Sendy Fransiscus Tantono

The Mechanical Behavior of a Soilbag under Vertical Compression

Monographic Series TU Graz

Computation in Engineering and Science

Series Editors

Monographic Series TU Graz

Computation in Engineering and Science Volume 2

Sendy Fransiscus Tantono

The Mechanical Behavior of a Soilbag under Vertical Compression

---

This work is based on the dissertation *The Mechanical Behavior of a Soilbag under Vertical Compression*, presented by S. F. Tantono at Graz University of Technology, Institute of Applied Mechanics in November 2007.
Supervisor: E. Bauer (Graz University of Technology)
Reviewer: E. Bauer (Graz University of Technology), D. Kolymbas (University of Innsbruck)

Bibliographic information published by Die Deutsche Bibliothek.
Die Deutsche Bibliothek lists this publication in the Deutsche Nationalbibliografie; detailed bibliographic data are available at http://dnb.ddb.de.

Cover photo	Vier-Spezies-Rechenmaschine by courtesy of the Gottfried Wilhelm Leibniz Bibliothek – Niedersächsische Landesbibliothek Hannover
Layout	Wolfgang Karl, TU Graz / Universitätsbibliothek
Printed	by TU Graz / Büroservice

Verlag der Technischen Universität Graz

www.ub.tugraz.at/Verlag

ISBN: 978-3-902465-97-9

Abstract

For a single soilbag filled with a cohesionless granular material analytical and numerical models based on a continuum approach are used to predict the evolution of deformation and stress under monotonic compression and plane strain conditions. Analytical models with different assumptions for the stress ratio distribution in the filling material, a constant volume and a frictionless interface between the soil and the wrapping bag are studied. In order to evaluate the simplifications assumed for the analytical model numerical simulations are carried out with a micro-polar hypoplastic model for the soil behavior and an elastic-ideally plastic model for the wrapping material. Particular attention is paid to the influence of the interface behavior between the soil and the bag material on the evolution of the state quantities. Herein the special cases of a frictionless interface and an interlocked interface are investigated. In contrast to the frictionless interface, the tensile stress in the wrapping bag material in the case of the interlocked interface is not homogeneous from the beginning of loading. Furthermore, the assumed interface behavior influences the evolution of the state quantities and the location of zones with intense strain localization of the granular material. The investigation with an initially random distribution of the void ratio of the granular material only shows an earlier onset of strain localization.

Zusammenfassung

Für eine mit einem Geotextil umschlossene Granulatpackung wird die Entwicklung der Verformungen und Spannungen bei ebener und monotoner Kompression sowohl mit analytischen wie auch numerischen Kontinuumsmodellen untersucht. Den analytischen Modellen liegen verschiedene Vereinfachungen zugrunde, wie beispielsweise ein konstantes Spannungsverhältnis, ein konstantes Volumen, sowie Reibungsfreiheit zwischen dem Granulat und der Einhüllung. Zur Bewertung der getroffenen Vereinfachungen werden numerische Untersuchungen mit einem mikropolaren hypoplastischen Materialmodell für das Granulat und einem elastisch-ideal plastisches Materialmodell für das Hüllmaterial durchgeführt. Besonderes Augenmerk wird auf den Einfluss der Kontakteigenschaften zwischen dem granularen Körper und der Einhüllung auf die Entwicklung der Zustandsgrößen gelegt. Die Untersuchungen zeigen für den reibungsbehafteten Kontakt eine inhomogene Verteilung der Membranspannung in der Hülle vom Beginn der Belastung. Darüber hinaus beeinflusst das Interfaceverhalten auch die Entwicklung der Spannungen und das Auftreten von Scherlokalisierungen im granularen Körper. Die Untersuchung mit einer anfänglichen Zufallsverteilung der Porenzahl im granularen Körper zeigt, dass Dehnungslokalisierungen bereits bei einer kleineren Kompression eintreten können.

CONTENTS

1 INTRODUCTION

A soilbag or sandbag is defined as a sack which is made of burlap or polymer materials filled with granular materials like sand, soil, or recycled concrete. The used filling material depends on the purpose of the structure and the availability of the filling material. Applications of a soilbag can either be for temporary or permanent constructions. For temporary constructions such as flooding barriers (Fig. 1.1(a)), soilbags are made and stacked up to several layers depending on the predicted flood-water level. After being used for certain period of time they are removed, emptied and disposed of. While the use of soilbags for temporary purpose has been established for a long time, its use in permanent constructions is rather new (Fig. 1.1(b) - 1.1(f)). For instance, soilbags can be used as reinforcement for increasing the bearing capacity of soft soil foundations, as damping layers for the reduction of vibration transmitted from traffic loads (e.g. Matsuoka & Liu, 2003 [81]), for facings installed in front of geosynthetic-reinforced soil retaining walls (e.g. Tatsuoka et al., 1997 [105]; Matsuoka & Liu, 2006 [82]), for ballast-foundations of railway tracks (e.g. Schilder, 1983 [99]; Matsuoka & Liu, 2003 [81]), for access roads in mountainous areas (e.g. Kimura & Fukubayashi, 2005 [69]), and for domes (e.g. Khalili, 1999 [68]).

The placing of layers of horizontal reinforcements underneath a foundation of a construction (e.g. footing, as shown in Fig. 1.2) is a well known method for improving the bearing capacity of shallow soil foundations. In this case, the reinforcement can take a part of the horizontal stress acting parallel to the layer of the reinforcement. Thus, with the reinforcement the lateral motion of soil can also be reduced which leads to smaller settlements. The motion of soil at the surrounding of the reinforcement is influenced by the developed shear resistance parallel to the interface between the granular soil and the reinforcement. The maximum shear resistance mainly depends on the type and surface structure of the reinforcement and the size of the grains. The maximum shear resistance is reached when either the tensile strength of the reinforcement is reached or the soil grains slip over the reinforcement. Large slippage of the soil particles over the reinforcement can lead to a heaving of the soil at the sides of the footing foundation. This behavior was demonstrated for instance in experiments by Matsuoka & Liu (2003 [81], 2006 [82]) with aluminium rods and a horizontal reinforcement. In order to reduce the heaving a closed form reinforcement as a part of the material under the footing was used, as sketched in Fig. 1.3. Using this closed form reinforcement Matsuoka & Liu (2003 [81], 2006 [82]) could show that under vertical loading the stiffness of the granular material inside the wrapping bag is higher than that outside. Consequently, the soil foundation can resist higher footing loads with the closed form reinforcement than with the plane layer reinforcement. Closed form reinforcements can be produced in an easy way with soilbags. Shape and dimension of the soilbags depend on their purposes (Fig. 1.4). The failure of a single soilbag is usually related

(a) **(b)**

(c) **(d)**

(e) **(f)**

Figure 1.1: Soilbags used for (**a**) temporary flooding barriers, (**b**) foundation of building, (**c**) retaining walls, (**d**) foundation of ballast for railway, (**e**) foundation of road, (**f**) dome construction.

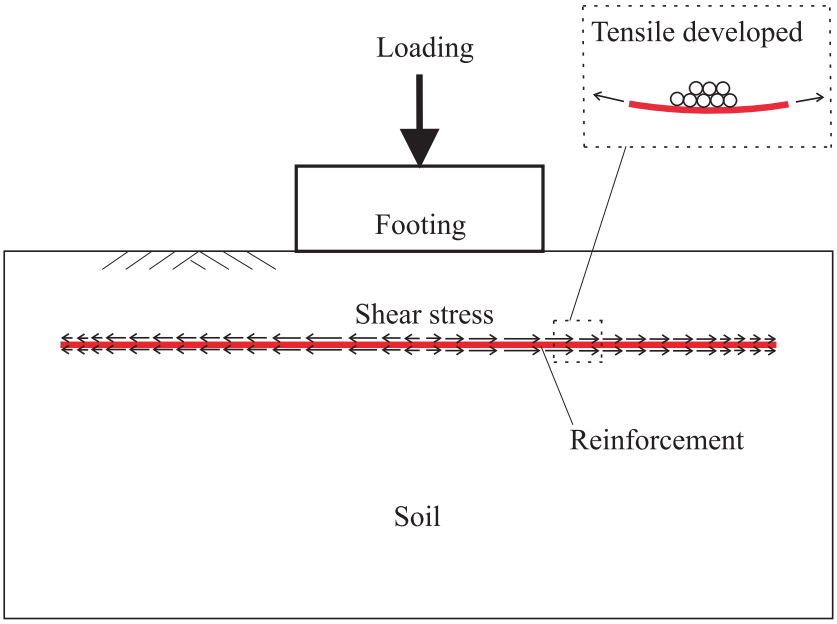

Figure 1.2: Illustration of the soil foundation reinforced with horizontal layer of reinforcement.

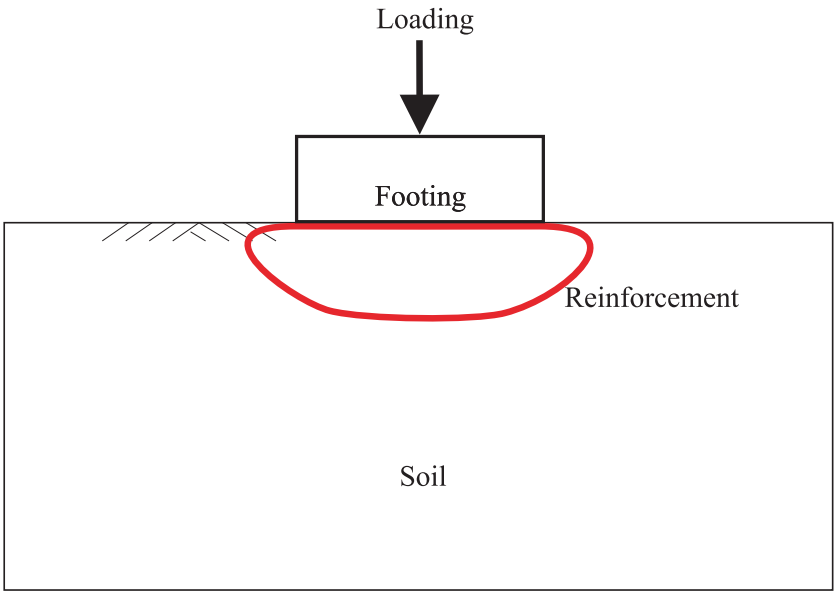

Figure 1.3: Illustration of the soil foundation reinforced with closed form reinforcement.

(a) **(b)**

Figure 1.4: Typical shapes of soilbags for instance for: (**a**) foundation of buildings and roads, (**b**) for dome.

with the tensile rupture of the bag material. Aqil et al. (2006) [2] reported that the shear load capacity is much lower than the vertical load capacity. Besides experimental results, there are only few analytical and numerical investigations on the mechanical behavior of soilbags (e.g. Tatsuoka, 2004 [103]; Matsuoka & Liu, 2006 [82]).

The present doctoral thesis focuses on the evolution of deformation and stress of a vertically compressed soilbag structure. Analytical and numerical investigations are carried out for plane strain condition. For the analytical study, similar simplifications are made as proposed by Matsuoka & Liu (2006) [82], e.g. the granular material deforms under constant volume, the stress ratio inside the soilbag is assumed to be constant and the contact between the soil and the bag is frictionless. The results obtained from the model by Matsuoka & Liu (2006) with a rectangular shape of the section of the soilbag are compared with that of a soilbag with lateral semicircular boundaries as proposed in this thesis. In order to validate the analytical results numerical investigations using the finite element method are also conducted. In the numerical model, particular attention is paid to the shear localization depending on the vertical displacement, the assumed interface properties and the initially homogeneous or inhomogeneous distribution of the void ratio. Furthermore, different interface behaviors between the granular material and the wrapping bag, i.e. a frictionless interface and an interlocked interface, is taken into account.

In addition, the influence of the interface properties on the deformation behavior of granular soil close to a bounding structure under shearing is also numerically studied. To this end, an infinite granular layer in contact with a rough bounding structure is considered. The influence of the slide and rotation resistances of the soil grains at the interface, the initial density of the granular specimen and the mean grain size on the location and the thickness of the shear band are investigated. Furthermore, fluctuations of the micro-polar boundary conditions along the interface are also studied.

Besides an enforced shear localization close to an interface, a so-called spontaneous development of shear bands far from bounding structures was observed, for instance also in a so-called element tests in the laboratory, e.g. in sand specimens under plane strain conditions (e.g. Oda et al., 1982 [92]; Desrues et al., 1996 [35]; Oda & Kazama, 1998 [91]; Alshibli & Sture, 2000 [1]; Gudehus, 1994 [50], 1997 [52], 2001 [54]; Oda et al., 2004 [93]) and in axisymetric triaxial tests (e.g. Drescher & Vardoulakis, 1982 [38]; Hettler & Vardoulakis, 1984 [59]; Frost & Jang, 2000 [44]). With the onset of strain localization the deformation becomes inhomogeneous so that the test is no longer an element test.

Regarding the mathematical modeling of shear bands in the granular body, it is well known that the numerical results obtained from finite element calculations with classical continuum models may show mesh dependencies when shear localization takes place (e.g. Neddleman, 1988 [88]; de Borst et al., 1993 [32]; Brinkgreve, 1994 [25]). Mesh dependency is related to the lack of an internal length in classical continuum descriptions. In order to overcome this shortcoming of classical continuum models, different enhanced continuum models had been proposed, for example, Cosserat continuum models (e.g. Mühlhaus & Vardoulakis, 1987 [86]; Mühlhaus, 1989 [84]; Mühlhaus, 1993 [85]; Tejchman & Gudehus, 2001 [114]; Ehlers, 2002 [39]; Huang & Bauer, 2003 [61]), non-local continuum theories (e.g. Bazant et al., 1987 [17]; Bazant & Lin, 1989 [16]; Bazant & Pijaudier-Cabot, 1989 [18]), and higher order gradient continuum models (e.g. Vardoulakis & Aifantis, 1989 [123]; de Borst & Mühlhaus, 1992 [31]; Han & Drescher, 1993 [57]; Pamin, 1994 [96]; Vardoulakis, 1999 [122]).

In the present study, a specific micro-polar model by Bauer & Huang (1999) [11] is adopted to describe the evolution of the non-symmetric stress tensor, couple stress tensor and void ratio of the granular material. The evolution equations for stress and couple stress are nonlinear tensor valued functions based on the framework of hypoplasticity which was originally developed within a non-polar continuum description (e.g. Kolymbas, 1978 [70], 1985 [71], 1987 [72], 1990 [73], 1991 [74], 2000 [75]; Darve, 1974 [28], 1991 [29]; Chambon, 1989 [26]; Kolymbas & Wu, 1993 [77]; Bauer & Wu, 1993 [14]; Wu & Bauer, 1993 [124]; Bauer, 1995 [3]; Gudehus, 1996 [51], 2006 [55]; Wu et al., 1996 [125]; Kolymbas & Herle, 1998 [76]; Bauer & Herle, 1999 [9]; Wu & Kolymbas, 1999 [126]). The micro-polar hypoplastic model takes into account macro-motion and micro-rotations, the current void ratio, the non-symmetric Cauchy stress tensor, the couple stress tensor and the mean grain size which enters the constitutive model as the characteristic length. By including the concept of critical states and with a pressure dependent density factor the model describes the essential properties of initially dense and initially loose granular soil for a wide range of pressures and densities with a single set of constitutive constants (e.g. Tejchman & Bauer, 1996 [111]; Tejchman & Gudehus, 2001 [114]; Huang & Bauer, 2003 [61]).

Beside a homogeneous distribution of the initial density for the granular material inside the soilbag, numerical simulations are also conducted with a random distribution of the initial void ratio. The inhomogeneity of the initial state may be neglected for certain geotechnical problem, such as large scale deformation analysis (e.g. Karcher, 2002), however, as shown by Nübel (2002) some problems related to the evolution of shear localization are sensitive against small

fluctuation of the initial density. In order to take into account the inhomogeneity of the initial void ratio different concepts for generating a random distribution of the void ratio have been proposed in the literature, e.g. Mogami (1965) [83], Shahinpoor (1981) [100], Bhatia & Soliman (1990) [22], Nübel (2002) [89], Nübel & Huang (2004), Huang et al. (2007) [64]. For example, Shahinpoor (1981) proposed a probability density function to describe the random distribution of the void ratio for granular materials with equal-sized hard spheres, which was also used by Nübel (2002) [89], Nübel & Huang (2004). Experiments carried out by Bhatia & Soliman (1990) [22] showed that the inhomogeneity of the void ratio for granular material like sand with different angularities and relative densities can be better represented by a density function with the so-called β-distribution. Huang et al. (2007) used this concept to prepare a random distribution of the void ratio for numerical simulations of granular materials like sand. In the present work, the same concept is also used for generating random distribution of the initial void ratio for the modeling of the filling material inside the soilbags.

For the numerical modeling of the interface properties using the finite element method, there are mainly two approaches. In the first approach the zones of the granular material close to the interface surface are modeled using a thin layer of so-called interface elements with peculiar properties which are different from the material properties used from granular material (e.g. Desai et al., 1984 [34]; Sharma & Desai, 1992 [101]). In this approach the thickness of the interface element needs to be specified and it is usually approximated by the thickness of the shear band. Experimental results, however, show that the thickness of shear band is not a material constant and is influenced by the whole boundary value problem. In the second approach, the contact problem between neighboring structures is solved. In particular, at the interface, kinematic discontinuities and tangential and normal displacement jumps (relative displacements) may take place (e.g. Goodman et al., 1968 [48]; Gens et al., 1988 [47]; Boulon & Nova, 1990 [24]; Day & Potts, 1994 [30]). In the normal direction the bodies are assumed to be in contact, while for the tangential direction Coulomb's friction law is usually used in classical finite element analysis of the interface. In particular, a constant ratio between the shear resistance and the normal pressure at the interface is assumed during shearing. However, this assumption only provides an approximate shear resistance at the interface and does not necessarily reflect the reality. In fact, according to the experimental results the shear resistance changes during shearing depending on several factors, such as density and mean grain size of the granular material, stress level, boundary conditions of the problem and type of the boundary value problem (e.g. Tejchman & Wu, 1995 [117]; Tejchman, 1997 [107]; Bauer & Huang, 1999 [11]; Bauer & Huang, 2004 [12]; Tejchman & Bauer, 2005 [113]). Therefore, in the numerical study, the actions of the soil particles at the interface such as sliding and rotation which are related to the surface roughness of the bounding structure and the mean grains size are furnished by the prescribed micro-polar boundary conditions at the interface. Thus, the shear resistance at the interface, as well as the occurrence and the thickness of the shear band is obtained as a prediction of the model (e.g. Tejchman & Bauer, 1996 [111]; Huang et al., 2003 [62]; Bauer & Huang, 2004 [12]).

The present doctoral thesis is structured as follows

- Chapter 1: Introduction and scope of the work.
- Chapter 2: A brief outline of the Cosserat continuum is given. A specific micro-polar hypoplastic model by Bauer & Huang (1999) [11] and its implementation in the finite element method for plane strain condition is presented.
- Chapter 3: Numerical simulations of shearing of a granular soil close to the surface of a bounding structure are conducted. Particular attention is paid to the influences of the micro-polar boundary conditions, the initial density of the granular body and the mean grain size on the evolution of the shear deformation and the shear resistance along the interface.
- Chapter 4: The mechanical properties of a single soilbag under vertical compression is analytically and numerically studied for different interface properties between the filling granular material and the wrapping bag. The analytical and numerical results are compared. Furthermore, the influence of an initial inhomogeneity of the void ratio on the evolution of the shear band patterns is also numerically investigated.
- Chapter 5: Summary of the main results is given.

2 MICRO-POLAR CONTINUUM MODEL

In this chapter, properties of the micro-polar continuum (e.g. Cosserat, 1909 [27]; Eringen & Suhubi, 1964 [42, 102]; Eringen, 1965 [40]; Besdo, 1985 [21]; Diebels, 2000 [37]; Ehlers, 2002 [39]; Bauer, 2004 [7]) are briefly described. A specific micro-polar hypoplastic version by Bauer & Huang (1999) [11] is presented and its implementation into the finite element program ABAQUS is outlined according to the procedure proposed by Huang (2000) [60] for plane strain condition.

2.1 Kinematic variables

The material points of the micro-polar continuum can translate and independently rotate. In general, each point possesses six degrees of freedom, i.e. three translation degrees of freedom and three rotational degrees of freedom. With respect to the position vector $\mathbf{X}$ of a material point of a body in the reference configuration $\mathcal{B}_0$ at time t_0 and the corresponding position vector $\mathbf{x}$ in the current configuration $\mathcal{B}$ at time $t > t_0$ (Fig. 2.1), the macromotion of the body is described by :

$$\mathbf{x} = \boldsymbol{\psi}(\mathbf{X}, t) \quad \text{or} \quad x_i = \psi_i(\mathbf{X}, t). \tag{2.1}$$

where x_i ($i = 1, 2, 3$) are the coordinates of the Cartesion coordinate system. The function $\boldsymbol{\psi}(\mathbf{X}, t)$ is postulated to be continuously differentiable and to be unique and uniquely invertible at any time, i.e.

$$\mathbf{X} = \boldsymbol{\psi}^{-1}(\mathbf{x}, t) \quad \text{or} \quad X_i = {\psi_i}^{-1}(\mathbf{x}, t). \tag{2.2}$$

The transformation of a line element $d\mathbf{X}$ of the body from the reference configuration $\mathcal{B}_0$ to the corresponding line element $d\mathbf{x}$ of the current configuration $\mathcal{B}$ is defined as:

$$d\mathbf{x} = \mathbf{F}\, d\mathbf{X}, \tag{2.3}$$

where the two point tensor $\mathbf{F}$ is the so-called deformation gradient:

$$\mathbf{F} = \frac{\partial \mathbf{x}}{\partial \mathbf{X}} \quad \text{or} \quad F_{ij} = \frac{\partial x_i}{\partial X_j}. \tag{2.4}$$

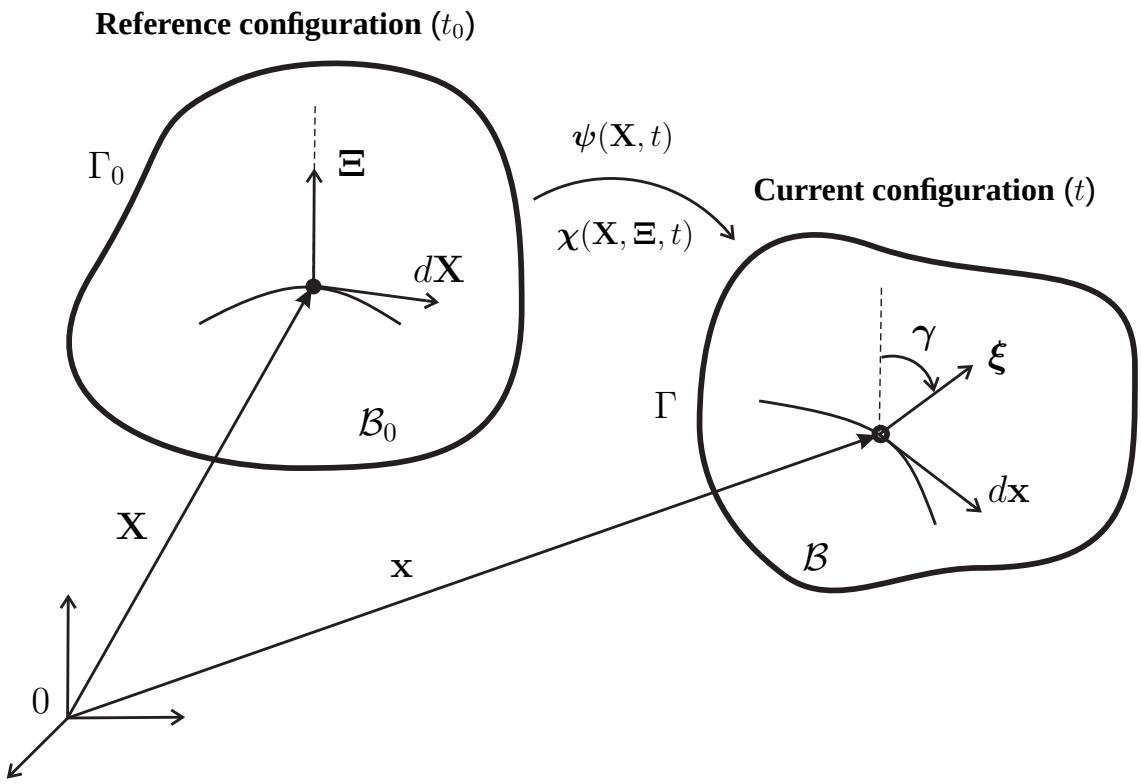

Figure 2.1: Macromotion and micromotion of a micro-polar continuum body.

In order to fulfil the requirement 2.2 the determinant of $\mathbf{F}$ must be a positive value, i.e. $\det[\mathbf{F}] > 0$. The material time derivative of Eq. 2.3 reads:

$$\frac{d\mathbf{x}}{dt} = \dot{\mathbf{x}} = \mathbf{L}\, d\mathbf{x}, \tag{2.5}$$

with the so-called velocity gradient $\mathbf{L}$, i.e.

$$\mathbf{L} = \dot{\mathbf{F}}\,\mathbf{F}^{-1} = \frac{\partial \dot{\mathbf{x}}}{\partial \mathbf{x}} = \frac{\partial \dot{\mathbf{u}}}{\partial \mathbf{x}} \quad \text{or} \quad L_{ij} = \frac{\partial \dot{x}_i}{\partial x_j} = \frac{\partial \dot{u}_i}{\partial x_j}. \tag{2.6}$$

In Eq. 2.6 the velocity vector $\dot{\mathbf{u}} = \dot{\mathbf{x}}$ can be obtained from the time derivative of the displacement vector $\mathbf{u} = \mathbf{x} - \mathbf{X}$.

The rotation degrees of freedom of points of a micro-polar continuum is described by directors $\boldsymbol{\Xi}$ of fixed length building a rigid triad attached to the material point X. The micromotion of the directors $\boldsymbol{\Xi}$ from the reference configuration $\mathcal{B}_0$ into the directors $\boldsymbol{\xi}$ of the current configuration $\mathcal{B}$ is described by

$$\boldsymbol{\xi} = \boldsymbol{\chi}(\mathbf{X}, \boldsymbol{\Xi}, t) \quad \text{or} \quad \xi_i = \chi_i(\mathbf{X}, \Xi_i, t). \tag{2.7}$$

The directors do not move like a material line element. The rotation of the directors can be represented by an orthogonal tensor $\bar{\mathbf{R}}$ with the properties $\bar{\mathbf{R}}^{-1} = \bar{\mathbf{R}}^T$ and $\det[\bar{\mathbf{R}}] = 1$. Tensor

$\bar{\mathbf{R}}$ rotates the directors $\boldsymbol{\Xi}$ of the reference configuration $\mathcal{B}_0$ into the directors $\boldsymbol{\xi}$ of the current configuration $\mathcal{B}$, i.e.

$$\boldsymbol{\xi} = \bar{\mathbf{R}}\,\boldsymbol{\Xi} \quad \text{or} \quad \xi_i = \bar{R}_{ij}\,\Xi_i. \tag{2.8}$$

The micro-rotation tensor $\bar{\mathbf{R}}$ can be expressed by the micro-rotation vector $\boldsymbol{\gamma} = \gamma\,\bar{\mathbf{e}}$ through the Euler-Rodrigues formula (e.g. Ehlers, 2002 [39])

$$\bar{\mathbf{R}} = \bar{\mathbf{e}} \otimes \bar{\mathbf{e}} + (\mathbf{I} - \bar{\mathbf{e}} \otimes \bar{\mathbf{e}}) \cos\gamma + (\bar{\mathbf{e}} \times \mathbf{I}) \sin\gamma. \tag{2.9}$$

The material time derivative of Eq. 2.8 yields

$$\dot{\boldsymbol{\xi}} = \dot{\bar{\mathbf{R}}}\bar{\mathbf{R}}^{\mathbf{T}}\,\boldsymbol{\xi} = \bar{\boldsymbol{\Omega}}\,\boldsymbol{\xi}. \tag{2.10}$$

Herein, $\bar{\boldsymbol{\Omega}} = \dot{\bar{\mathbf{R}}}\bar{\mathbf{R}}^{\mathbf{T}}$ is called micro-polar gyration tensor and is an antisymmetric tensor in the current configuration. The micro-polar gyration tensor $\bar{\boldsymbol{\Omega}}$ can be represented by the rate of the Cosserat rotation $\dot{\boldsymbol{\omega}}^c$ according to

$$\bar{\boldsymbol{\Omega}} = -\dot{\boldsymbol{\omega}}^c \cdot \boldsymbol{\epsilon} \quad \text{or} \quad \bar{\Omega}_{ij} = -\epsilon_{kij}\,\dot{\omega}^c_k. \tag{2.11}$$

or

$$\dot{\boldsymbol{\omega}}^c = \frac{1}{2}\,\boldsymbol{\epsilon} : \bar{\boldsymbol{\Omega}}^T \quad \text{or} \quad \dot{\omega}^c_k = \frac{1}{2}\,\epsilon_{kji}\,\bar{\Omega}_{ji}, \tag{2.12}$$

where $\boldsymbol{\epsilon}$ denotes the permutation tensor.

The non-symmetric Cosserat strain rate tensor is defined as:

$$\dot{\boldsymbol{\varepsilon}}^c = \mathbf{L} - \bar{\boldsymbol{\Omega}} = \mathbf{L} + \dot{\boldsymbol{\omega}}^c \cdot \boldsymbol{\epsilon} \quad \text{or} \quad \dot{\varepsilon}^c_{ij} = L_{ij} + \epsilon_{kij}\dot{\omega}^c_k. \tag{2.13}$$

The velocity gradient $\mathbf{L}$ can also be represented as the sum of $\dot{\boldsymbol{\varepsilon}}$ and $\mathbf{W}$, i.e.

$$\mathbf{L} = \dot{\boldsymbol{\varepsilon}} + \mathbf{W} \quad \text{or} \quad L_{ij} = \dot{\varepsilon}_{ij} + W_{ij}, \tag{2.14}$$

with the symmetric tensor

$$\dot{\boldsymbol{\varepsilon}} = \frac{1}{2}\left(\mathbf{L} + \mathbf{L}^T\right) \quad \text{or} \quad \dot{\varepsilon}_{ij} = \frac{1}{2}\left(L_{ij} + L_{ji}\right) \tag{2.15}$$

and the skew-symmetric tensor

$$\mathbf{W} = \frac{1}{2}\left(\mathbf{L} - \mathbf{L}^T\right) \quad \text{or} \quad W_{ij} = \frac{1}{2}\left(L_{ij} - L_{ji}\right). \tag{2.16}$$

$\mathbf{W}$ is also termed as the macro-spin tensor and it can be represented by the macro-spin vector $\dot{\boldsymbol{\omega}}$ according to the following relations

$$\mathbf{W} = -\dot{\boldsymbol{\omega}} \cdot \boldsymbol{\epsilon} \quad \text{or} \quad W_{ij} = -\epsilon_{kij}\, \dot{\omega}_k, \tag{2.17}$$

or

$$\dot{\boldsymbol{\omega}} = -\frac{1}{2}\boldsymbol{\epsilon} : \mathbf{W} \quad \text{or} \quad \dot{\omega}_k = -\frac{1}{2}\epsilon_{kij}\, W_{ij}. \tag{2.18}$$

Then $\dot{\boldsymbol{\varepsilon}}^c$ in Eq. 2.13 can alternatively be represented as

$$\dot{\boldsymbol{\varepsilon}}^c = \dot{\boldsymbol{\varepsilon}} \; - \; \dot{\boldsymbol{\omega}} \cdot \boldsymbol{\epsilon} \; + \; \dot{\boldsymbol{\omega}}^c \cdot \boldsymbol{\epsilon} \quad \text{or} \quad \dot{\varepsilon}^c_{ij} = \dot{\varepsilon}_{ij} - \epsilon_{kij}\, \dot{\omega}_k + \epsilon_{kij}\, \dot{\omega}^c_k. \tag{2.19}$$

From Eq. 2.19 it can be seen that the non-symmetric Cosserat strain rate tensor can be decomposed into the symmetric part $\dot{\boldsymbol{\varepsilon}}$ and the skew symmetric part
$(-\,\dot{\boldsymbol{\omega}} \cdot \boldsymbol{\epsilon} \; + \; \dot{\boldsymbol{\omega}}^c \cdot \boldsymbol{\epsilon})$. Only for $\dot{\boldsymbol{\omega}}^c = \dot{\boldsymbol{\omega}}$ the non-symmetric Cosserat strain tensor $\dot{\boldsymbol{\varepsilon}}^c$ in Eq. 2.19 reduces to the symmetric strain rate tensor $\dot{\boldsymbol{\varepsilon}}$ of the non-polar continuum.

The rate of gradient of the Cosserat rotation is the so-called rate of curvature tensor, i.e.

$$\dot{\boldsymbol{\kappa}} = \frac{\partial \dot{\boldsymbol{\omega}}^c}{\partial \mathbf{x}} \quad \text{or} \quad \dot{\kappa}_{ij} = \frac{\partial \dot{\omega}^c_i}{\partial x_j}. \tag{2.20}$$

2.2 Balance equations

2.2.1 Balance of mass

The principle of conservation of mass requires that the mass m of the body does not change during motion. Thus, $Dm/Dt = 0$ holds independent of the configuration of the body. With respect to a scalar field ρ, called mass density, the conservation of mass requires:

$$m = \int_{\mathcal{B}_0} \rho_0(\mathbf{X}, t_0) dV_0 = \int_{\mathcal{B}} \rho(\mathbf{x}, t) dV, \tag{2.21}$$

where ρ_0 is the mass density of the body in the reference configuration and ρ denotes the mass density in the current configuration.

For the continuously differentiable scalar function $\rho(\mathbf{x}, t)$ and using Reynold's transport theorem the material time derivative of Eq. 2.21 yields the following global form of conservation of mass (e.g. Fung, 1994 [45])

$$\frac{D\, m}{D\, t} = \frac{D}{Dt} \int_{\mathcal{B}} \rho \, dV = \int_{\mathcal{B}} \left[\frac{D\rho}{Dt} \; + \; \rho \, \mathrm{div}(\dot{\mathbf{u}}) \right] dV = 0. \tag{2.22}$$

Since the equation holds for an arbitrary choice of the volume V within the continuous body, the integrand in Eq. 2.22 must vanish. Hence

$$\frac{D\rho}{Dt} + \rho \operatorname{div}(\dot{\mathbf{u}}) = 0 \quad \text{or} \quad \dot{\rho} + \rho \frac{\partial \dot{u}_j}{\partial x_j} = 0 \quad \text{or} \quad \dot{\rho} + \rho \dot{\varepsilon}^c_{kk} = 0 \tag{2.23}$$

holds for each point in the body. Relation 2.23 is the local form of conservation of mass in the spatial description. For the special case of an incompressible material or an isochoric deformation, i.e. a deformation under constant volume $\dot{\varepsilon}^c_{kk} = 0$, the mass density remains constant.

2.2.2 Balance of linear momentum

Following Newton's second law of motion, in an inertial frame of reference, the material time derivative of the linear momentum $\mathbf{p}$ of a body in the current configuration $\mathcal{B}$ is equal to the resultant force $\boldsymbol{\mathcal{F}}$ to the body

$$\frac{D\mathbf{p}}{Dt} = \frac{D}{Dt} \int_{\mathcal{B}} \rho \, \dot{\mathbf{u}} \, dV = \boldsymbol{\mathcal{F}}. \tag{2.24}$$

The forces acting on the body can be obtained by integration of the surface traction $\mathbf{t}$ per unit area over the surface boundary Γ and the integration of the body force $\rho \, \mathbf{b}$ per unit volume over the volume of a body in the current configuration $\mathcal{B}$. Hence

$$\frac{D}{Dt} \int_{\mathcal{B}} \rho \, \dot{\mathbf{u}} \, dV = \int_{\Gamma} \mathbf{t} \, d\Gamma + \int_{\mathcal{B}} \rho \, \mathbf{b} \, dV. \tag{2.25}$$

Applying Reynold's transport theorem to the integral on the left hand side of Eq. 2.25 gives:

$$\frac{D}{Dt} \int_{\mathcal{B}} \rho \, \dot{\mathbf{u}} \, dV = \int_{\mathcal{B}} \left[\frac{D}{Dt}(\rho \, \dot{\mathbf{u}}) + \operatorname{div}(\dot{\mathbf{u}}) \, \rho \, \dot{\mathbf{u}} \right] dV.$$

Using the product rule of derivatives for the first term and rearranging the terms,

$$\frac{D}{Dt} \int_{\mathcal{B}} \rho \, \dot{\mathbf{u}} \, dV = \int_{\mathcal{B}} \left[\rho \frac{D\dot{\mathbf{u}}}{Dt} + \dot{\mathbf{u}} \left(\frac{D\rho}{Dt} + \rho \operatorname{div}(\dot{\mathbf{u}}) \right) \right] dV.$$

By substituting the balance equation of mass (Eq. 2.23) to the second term of the above equation, one obtains:

$$\frac{D}{Dt} \int_{\mathcal{B}} \rho \, \dot{\mathbf{u}} \, dV = \int_{\mathcal{B}} \rho \frac{D\dot{\mathbf{u}}}{Dt} dV = \int_{\mathcal{B}} \rho \, \ddot{\mathbf{u}} \, dV.$$

Applying Gauss' theorem to the first term of the right hand side of Eq. 2.25

$$\int_{\Gamma} \mathbf{t}\, d\Gamma = \int_{\Gamma} \boldsymbol{\sigma} \cdot \mathbf{n}\, d\Gamma = \int_{\mathcal{B}} \operatorname{div}(\boldsymbol{\sigma})\, dV.$$

Then, the conservation equation of linear momentum can be written as

$$\int_{\mathcal{B}} \rho\, \ddot{\mathbf{u}}\, dV \;=\; \int_{\mathcal{B}} \Big[\rho\, \mathbf{b} \;+\; \operatorname{div}(\boldsymbol{\sigma})\Big] dV,$$

or

$$\int_{\mathcal{B}} \rho\, \ddot{u}_i\, dV \;=\; \int_{\mathcal{B}} \left[\rho\, b_i \;+\; \frac{\partial \sigma_{ij}}{\partial x_j}\right] dV.$$

For quasi-static problems, $D\dot{\mathbf{u}}/Dt \;=\; \ddot{\mathbf{u}} \;=\; 0$, so that the conservation of linear momentum reduces to the equilibrium equation

$$\int_{\mathcal{B}} \Big[\rho\, \mathbf{b} \;+\; \operatorname{div}(\boldsymbol{\sigma})\Big] dV = \mathbf{0} \quad \text{or} \quad \int_{\mathcal{B}} \left[\rho\, b_i \;+\; \frac{\partial \sigma_{ij}}{\partial x_j}\right] dV = 0.$$

Since the above equation holds for arbitrary volume V within the body, one obtains the local form as:

$$\rho\, \mathbf{b} \;+\; \operatorname{div}(\boldsymbol{\sigma}) \;= \mathbf{0} \quad \text{or} \quad \rho\, b_i \;+\; \frac{\partial \sigma_{ij}}{\partial x_j} \;= 0. \tag{2.26}$$

2.2.3 Balance of moment of momentum

The balance of moment of momentum states that the material time derivative of moment of momentum is equal to the total torque acting on the body. Following e.g. Eringen & Kafadar (1976) [41], Diebles (2000) [37], Ehlers (2002) [39], the balance of moment of momentum for the micro-polar continuum can be expressed as

$$\frac{D}{Dt} \int_{\mathcal{B}} \left[\mathbf{x} \times \rho\, \dot{\mathbf{u}} + \rho\, \boldsymbol{\Theta}\, \dot{\boldsymbol{\omega}}^{c}\right] dV \;=\; \int_{\mathcal{B}} \left[\mathbf{x} \times \rho\, \mathbf{b} + \rho\, \mathbf{c}\right] dV + \int_{\Gamma} \left[\mathbf{x} \times \mathbf{t} + \mathbf{m}\right] d\Gamma. \tag{2.27}$$

Herein, $\rho\, \boldsymbol{\Theta}$ represents the tensor of micro-inertia and $\mathbf{c}$ is the body couple per unit mass. With the Gauss' theorem the second term in the right hand side of Eq. 2.27 can be written as

$$\begin{aligned} \int_{\Gamma} \Big[\mathbf{x} \times \mathbf{t} + \mathbf{m}\Big] d\Gamma \;&=\; \int_{\Gamma} \Big[\mathbf{x} \times \boldsymbol{\sigma}\, \mathbf{n} \;+\; \boldsymbol{\mu}\, \mathbf{n}\Big] d\Gamma \;=\; \int_{\mathcal{B}} \Big[\operatorname{div}(\mathbf{x} \times \boldsymbol{\sigma}) \;+\; \operatorname{div}(\boldsymbol{\mu})\Big] dV \\ &=\; \int_{\mathcal{B}} \Big[\Big(\operatorname{grad}(\mathbf{x})\Big) \times \boldsymbol{\sigma} \;+\; \mathbf{x} \times \operatorname{div}(\boldsymbol{\sigma}) \;+\; \operatorname{div}(\boldsymbol{\mu})\Big] dV. \end{aligned}$$

In the following only quasi-static problems are considered, so that the balance of moment of momentum reduces to

$$0 \;=\; \int\limits_{\mathcal{B}} \Big[\mathbf{x} \times \rho\,\mathbf{b} \,+\, \rho\,\mathbf{c} \,+\, \Big(\mathrm{grad}(\mathbf{x})\Big) \times \boldsymbol{\sigma} \,+\, \mathbf{x} \times \mathrm{div}(\boldsymbol{\sigma}) \,+\, \mathrm{div}(\boldsymbol{\mu})\Big] dV$$

$$= \int\limits_{\mathcal{B}} \Big[\mathbf{x} \times \Big(\rho\,\mathbf{b} \,+\, \mathrm{div}(\boldsymbol{\sigma})\Big) \,+\, \rho\,\mathbf{c} \,+\, \Big(\mathrm{grad}(\mathbf{x})\Big) \times \boldsymbol{\sigma} \,+\, \mathrm{div}(\boldsymbol{\mu})\Big] dV.$$

With respect to $(\mathrm{grad}(\mathbf{x})) \times \boldsymbol{\sigma} = \mathbf{I} \times \boldsymbol{\sigma} = \epsilon : \boldsymbol{\sigma}^T = -\epsilon : \boldsymbol{\sigma}$ and by substituting the balance equation of linear momentum (Eq. 2.26) to the first term of the right hand side of the above equation, one obtains

$$0 = \int\limits_{\mathcal{B}} \Big[\rho\,\mathbf{c} \,-\, \epsilon : \boldsymbol{\sigma} \,+\, \mathrm{div}(\boldsymbol{\mu})\Big] dV. \tag{2.28}$$

The local form of Eq. 2.28 reads

$$\rho\,\mathbf{c} \,-\, \epsilon : \boldsymbol{\sigma} \,+\, \mathrm{div}(\boldsymbol{\mu}) \,=\, 0 \quad \text{or} \quad \rho\,c_i \,-\, \epsilon_{ijk}\,\sigma_{jk} \,+\, \frac{\partial \mu_{ij}}{\partial x_j} \,=\, 0. \tag{2.29}$$

It follows from Eq. 2.29 that the stress tensor in a micro-polar continuum is non-symmetric, i.e. $\epsilon : \boldsymbol{\sigma} \neq 0$, with the exception of states where $\partial \mu_{ij}/\partial x_j = 0$ and $c_i = 0$ vanishes simultaneously (Huang & Bauer, 2003 [61]).

2.3 Micro-polar hypoplastic model

2.3.1 Evolution equation for the void ratio

For the numerical modeling of cohesionless granular materials the assumption is made that the volume of the solid grains does not change during any arbitrary deformation of the granular body. Therefore, a volume change of the body is equal to the volume change of the void space between the solid grains. Furthermore, if the void space is empty the mass m of the body is equal to the mass m_s of the solid grains, i.e.

$$m = m_s \quad \text{or equivalent to} \quad \rho\,V \,=\, \rho_s\,V_s,$$

where ρ is the mass density of the granular body and ρ_s denotes the mass density of the solid grains. For a representative volume element of a granular body, the total volume V can be

decomposed into the volume V_s of the solid grains and the volume V_v of the void space. With respect to the definition of the void ratio $e = V_v/V_s$, the mass density ρ can be expressed as:

$$\rho \;=\; \frac{\rho_s\, V_s}{V} \;=\; \frac{\rho_s\, V_s}{V_v + V_s} \;=\; \frac{\rho_s}{1+e}. \tag{2.30}$$

Substituting the above relation for ρ to the balance equation of mass (Eq. 2.23), one obtains

$$\frac{D}{D\,t}\left(\frac{\rho_s}{1+e}\right) \;+\; \frac{\rho_s}{1+e}\,\dot{\varepsilon}^c_{kk} \;=\; 0. \tag{2.31}$$

With the assumption that the volume of the solid grains does not change and also the mass density ρ_s of the grains remains constant, Eq. 2.31 can be rewritten into

$$\rho_s\left[\frac{-\dot{e}}{(1+e)^2} \;+\; \frac{1}{1+e}\,\dot{\varepsilon}^c_{kk}\right] \;=\; 0. \tag{2.32}$$

Since $\rho_s \neq 0$ the following evolution equation for the void ratio e is obtained

$$\dot{e} = (1+e)\;\dot{\varepsilon}^c_{kk}. \tag{2.33}$$

It is worth noting that with the assumption of an empty void space and $\rho_s = \mathrm{const.}$, the granular body can be treated as a single-component continuum (Bauer, 2005 [8]).

2.3.2 Constitutive relations for the stress and the couple stress

The evolution equations for the stresses σ_{ij}, the couple stresses μ_{ij} and the void ratio e of the micro-polar hypoplastic model by Bauer & Huang (1999) [11], Huang & Bauer (2003) [61] read

$$\mathring{\sigma}_{ij} = f_s\,\left[\hat{a}^2\,\dot{\varepsilon}^c_{ij} \;+\; (\hat{\sigma}_{kl}\dot{\varepsilon}^c_{kl} + \hat{\mu}_{kl}\dot{\kappa}^*_{kl})\,\hat{\sigma}_{ij} \;+\; f_d\,\hat{a}\,\left(\hat{\sigma}_{ij} + \hat{\sigma}^d_{ij}\right)\sqrt{\dot{\varepsilon}^c_{kl}\dot{\varepsilon}^c_{kl} + \dot{\kappa}^*_{kl}\dot{\kappa}^*_{kl}}\right], \tag{2.34}$$

$$\mathring{\mu}_{ij} = d_{50}\,f_s\,\left[a^2_m\,\dot{\kappa}^*_{ij} \;+\; (\hat{\sigma}_{kl}\dot{\varepsilon}^c_{kl} + \hat{\mu}_{kl}\dot{\kappa}^*_{kl})\,\hat{\mu}_{ij} \;+\; 2\,f_d\,a_m\,\hat{\mu}_{ij}\sqrt{\dot{\varepsilon}^c_{kl}\dot{\varepsilon}^c_{kl} + \dot{\kappa}^*_{kl}\dot{\kappa}^*_{kl}}\right], \tag{2.35}$$

$$\dot{e} = (1+e)\dot{\varepsilon}^c_{kk}. \tag{2.36}$$

Herein, $\mathring{\sigma}_{ij}$ is the objective stress rate given by Jaumann-Zaremba

$$\mathring{\sigma}_{ij} = \dot{\sigma}_{ij} + \sigma_{ik}W_{kj} - W_{ik}\sigma_{kj}, \tag{2.37}$$

and $\mathring{\mu}_{ij}$ is the objective couple stress rate

$$\mathring{\mu}_{ij} = \dot{\mu}_{ij} + \mu_{ik} W_{kj} - W_{ik} \mu_{kj}. \tag{2.38}$$

The constitutive equations 2.34 and 2.35 use tensor valued functions depending on the current void ratio e, the non-symmetric stress tensor $\boldsymbol{\sigma}$, the couple stress tensor $\boldsymbol{\mu}$, the non-symmetric strain rate tensor $\dot{\boldsymbol{\varepsilon}}^c$ and the rate of curvature tensor $\dot{\boldsymbol{\kappa}}$, where the normalized quantities $\hat{\sigma}_{ij}$, $\hat{\sigma}^d_{ij}$, $\hat{\mu}_{ij}$ and $\dot{\kappa}^*_{ij}$ have the following meaning

$$\hat{\sigma}_{ij} = \sigma_{ij}/\sigma_{kk}, \quad \hat{\sigma}^d_{ij} = \hat{\sigma}_{ij} - \delta_{ij}/3, \quad \hat{\mu}_{ij} = \mu_{ij}/(d_{50}\,\sigma_{kk}), \quad \dot{\kappa}^*_{ij} = d_{50}\,\dot{\kappa}_{ij}.$$

Herein, δ_{ij} is the Kronecker delta and d_{50} denotes the mean grain diameter, which enters the constitutive model as the characteristic length. The scalar factors f_s and f_d are called stiffness and density factors, respectively. Factors $\hat{a}$ and a_m are related to the limit stress and limit couple stress at critical states.

The stiffness factor f_s and the density factor f_d in Eqs. 2.34 - 2.35 are functions of relative void ratios which are pressure dependent. In particular, the stiffness factor f_s is proportional to the granular hardness h_s and depends on the current void ratio e, the maximum void ratio e_i and the stress σ_{kk}, i.e. (Bauer, 1995 [3])

$$f_s = \left(\frac{e_i}{e}\right)^{\beta} \frac{h_s\,(1+e_i)}{n\,h_i\,(\hat{\sigma}_{kl}\,\hat{\sigma}_{kl})\,e_i} \left(-\frac{\sigma_{kk}}{h_s}\right)^{1-n}, \tag{2.39}$$

with

$$h_i = \frac{8\,\sin^2\varphi}{(3+\sin\varphi)^2} + 1 - \frac{2\sqrt{2}\,\sin\varphi}{3+\sin\varphi} \left(\frac{e_{io} - e_{do}}{e_{co} - e_{do}}\right)^{\alpha}.$$

Herein $\beta > 1$, h_s, n are constitutive constants.

The density factor f_d is related to the current void ratio e, the minimum void ratio e_d and the critical void ratio e_c

$$f_d = \left(\frac{e - e_d}{e_c - e_d}\right)^{\alpha}. \tag{2.40}$$

Herein, $\alpha < 0.5$ is a positive constant. In Eq. (2.39) and Eq. (2.40) the void ratios e_i, e_d and e_c are pressure dependent. These limit void ratios decrease with an increase of pressure σ_{kk}, i.e. (Gudehus, 1996 [51])

$$\frac{e_i}{e_{i0}} = \frac{e_d}{e_{d0}} = \frac{e_c}{e_{c0}} = \exp\left[-\left(-\frac{\sigma_{kk}}{h_s}\right)^{n}\right], \tag{2.41}$$

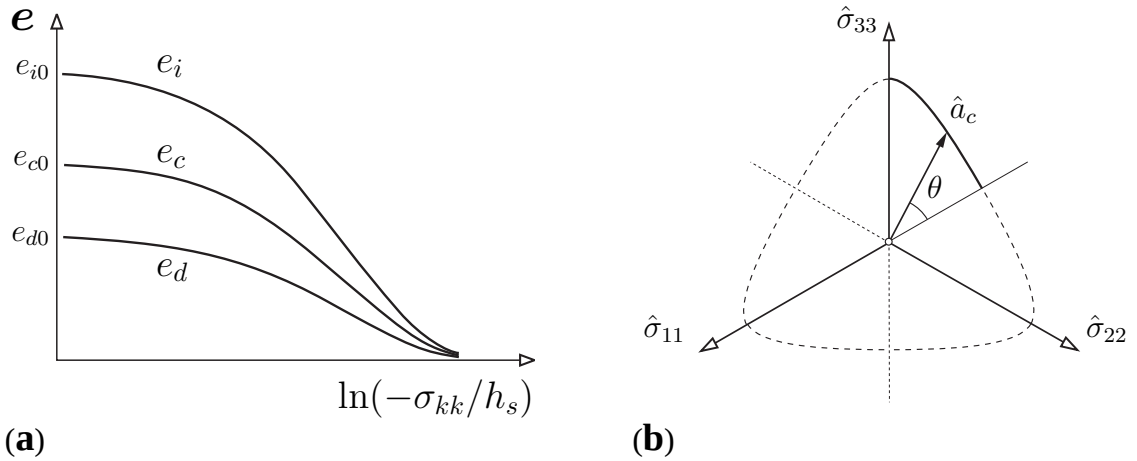

Figure 2.2: (**a**) Pressure dependence of the limit void ratios, (**b**) critical stress surface by Matsuoka Nakai (1977) in deviatoric plane.

where e_{i0}, e_{d0}, e_{c0} are the corresponding values for $\sigma_{kk} \approx 0$ (Fig. 2.2(a)). From Eq. 2.40, it follows that independent of the magnitude of pressure σ_{kk}:

$$\begin{aligned} &\text{for } e = e_c \quad \longrightarrow \quad f_d = 1, \\ &\text{for } e > e_c \quad \longrightarrow \quad f_d > 1, \\ &\text{for } e < e_c \quad \longrightarrow \quad f_d < 1. \end{aligned}$$

It was shown by Bauer (1999) [5] that for monotonic shearing and $f_d > 1$ the non-polar hypoplastic model describes contractancy while for $f_d < 1$ dilatancy becomes dominant.

In the model by Bauer & Huang (1999) [11], factor a_m is assumed to be constant. Factor $\hat{a}$ is adapted to the limit condition by Matsuoka-Nakai (1977). For arbitrary states $\hat{a}$ reads (Bauer, 2000 [6])

$$\hat{a} = \frac{\sin\varphi_c}{3-\sin\varphi_c}\left[\sqrt{\frac{8/3 - 3(\hat{\sigma}^{sd}_{kl}\,\hat{\sigma}^{sd}_{kl}) + \sqrt{3/2}\,(\hat{\sigma}^{sd}_{kl}\,\hat{\sigma}^{sd}_{kl})^{3/2}\cos(3\theta)}{1 + \sqrt{3/2}\,(\hat{\sigma}^{sd}_{kl}\,\hat{\sigma}^{sd}_{kl})^{1/2}\cos(3\theta)}} - \sqrt{\hat{\sigma}^{sd}_{kl}\,\hat{\sigma}^{sd}_{kl}}\right]. \tag{2.42}$$

In Eq. 2.42 φ_c denotes the critical friction angle, $\hat{\sigma}^{sd}_{kl} = (\hat{\sigma}^{d}_{kl} + \hat{\sigma}^{d}_{lk})/2$ and θ represents the so-called Lode angle which is defined as

$$\cos(3\theta) = -\sqrt{6}\frac{\hat{\sigma}^{sd}_{kl}\hat{\sigma}^{sd}_{lm}\hat{\sigma}^{sd}_{mk}}{(\hat{\sigma}^{sd}_{kl}\,\hat{\sigma}^{sd}_{kl})^{3/2}}. \tag{2.43}$$

When the limit stress condition is met the value of $\hat{a} = \hat{a}_c$. Then Eq. 2.42 represents the limit

condition by Matsuoka-Nakai (1977), as sketch out in the deviatoric plane in Fig. 2.2(b). It can be noted that for the special case of purely coaxial and homogeneous deformations starting from an initially symmetric stress tensor or for $d_{50} \to 0$ there are no polar effect, i.e. $\mu_{ij} = \dot{\mu}_{ij} = 0$, $\dot{\varepsilon}^c_{ij} = \dot{\varepsilon}_{ij}$ and $\sigma_{ij} = \sigma_{ji}$, so that the present micro-polar hypoplastic model reduces to the non-polar one given by Gudehus (1996) [51] and Bauer (1996) [4], i.e.

$$\mathring{\sigma}_{ij} = f_s \left[\hat{a}^2 \dot{\varepsilon}_{ij} + \hat{\sigma}_{ij} \left(\hat{\sigma}_{kl} \dot{\varepsilon}_{kl} \right) + f_d \, \hat{a} \left(\hat{\sigma}_{ij} + \hat{\sigma}^d_{ij} \right) \| \dot{\varepsilon}_{ij} \| \right] . \tag{2.44}$$

It follows from Eq. 2.44 that the functions f_s, $\hat{a}$ and f_d are the same for the micro-polar and non-polar version. Therefore coaxial and homogeneous deformation is sufficient for the adaptation of the constants involved in this functions as outlined in details by Bauer (1996) [4], Herle & Gudehus (1999) [58] and Huang & Bauer (2003) [61].

2.3.3 Calibration of the constitutive constants

The micro-polar hypoplastic model includes the following 10 constants: φ_c, h_s, n, e_{i0}, e_{d0}, e_{c0}, α, β, d_{50} and a_m. They can be determined from simple index and element test (Bauer, 1996 [4]; Herle & Gudehus, 1999 [58]). The critical friction angle φ_c is defined for a triaxial compression test in the critical state and, approximately, it corresponds to the angle of repose. The void ratios e_{d0} and e_{c0} are related to the minimum and the maximum void ratio in a nearly stress free state, respectively. The maximum void ratio e_{i0} can be approximated by a scaling factor to e_{c0}, for instance $e_{i0} \simeq 1.2\, e_{c0}$ (e.g. Herle & Gudehus, 1999 [58]). Parameters h_s and n can be related to an isotropic compression test starting from a loose specimen with a void ratio of $\simeq e_{i0}$. α and β are related to the peak friction angle in triaxial compression tests with initially loose and dense specimens (Bauer, 1996 [4]). The mean grain diameter d_{50} can be estimated from the grain size distribution. The micro-polar constant a_m is related to the rotation resistance of particles and it can be related to the shear band thickness using back analysis (Huang, 2000 [60]).

The values for the constitutive constants obtained for quartz sand (Huang & Bauer, 2003 [61]) are used for numerical simulations in the following chapters:

$e_{i0} = 1.20$, $e_{d0} = 0.51$, $e_{c0} = 0.82$, $\varphi_c = 30^0$, $a_m = 1.0$,
$h_s = 190$ MPa, $\alpha = 0.11$, $\beta = 1.05$, $n = 0.4$, $d_{50} = 0.5$ mm.

2.4 Implementation into the finite element method

2.4.1 Virtual power equation

For establishing the finite element formulation the virtual power equation is used. By taking the product of the virtual variations of the velocity fields, i.e. $\delta\dot{u}_i$ and $\delta\dot{\omega}_k^c$, with the equilibrium equations 2.26 and Eq. 2.29 and integrating over the volume of the body in the current configuration leads to the following weak form

$$\int_{\mathcal{B}} \left[\delta\dot{u}_i \frac{\partial \sigma_{ij}}{\partial x_j} + \delta\dot{u}_i \rho b_i + \delta\dot{\omega}_k^c \frac{\partial \mu_{kj}}{\partial x_j} - \delta\dot{\omega}_k^c \epsilon_{kij} \sigma_{ij} + \delta\dot{\omega}_k^c \rho c_k \right] dV = 0. \tag{2.45}$$

Applying the Gauss' theorem to the first term of Eq. 2.45,

$$\int_{\mathcal{B}} \delta\dot{u}_i \frac{\partial \sigma_{ij}}{\partial x_j} dV = \int_{\Gamma} \delta\dot{u}_i \sigma_{ij} n_j d\Gamma - \int_{\mathcal{B}} \frac{\partial(\delta\dot{u}_i)}{\partial x_j} \sigma_{ij} dV,$$

and to the third term of Eq. 2.45

$$\int_{\mathcal{B}} \delta\dot{\omega}_k^c \frac{\partial \mu_{kj}}{\partial x_j} dV = \int_{\Gamma} \delta\dot{\omega}_k^c \mu_{kj} n_j d\Gamma - \int_{\mathcal{B}} \frac{\partial(\delta\dot{\omega}_k^c)}{\partial x_j} \mu_{kj} dV,$$

Eq. 2.45 becomes

$$\begin{aligned} &\int_{\mathcal{B}} \left[\delta\dot{u}_i \rho b_i + \delta\dot{\omega}_k^c \rho c_k \right] dV + \int_{\Gamma} \left[\delta\dot{u}_i \sigma_{ij} n_j + \delta\dot{\omega}_k^c \mu_{kj} n_j \right] d\Gamma \\ &- \int_{\mathcal{B}} \left[\epsilon_{ijk} \delta\dot{\omega}_k^c \sigma_{ij} + \frac{\partial(\delta\dot{u}_i)}{\partial x_j} \sigma_{ij} + \frac{\partial(\delta\dot{\omega}_k^c)}{\partial x_j} \mu_{kj} \right] dV = 0. \end{aligned} \tag{2.46}$$

In the current configuration, the surface traction $t_i = \sigma_{ij} n_j$ is prescribed on the part Γ_t of the body surface while the surface couple $m_k = \mu_{kj} n_j$ is prescribed on Γ_m. The virtual velocity fields $\delta\dot{u}_i$ and $\delta\dot{\omega}_k^c$ are independent from each other, small and arbitrary, except on the surface Γ_u where $\dot{u}_i$ is prescribed and $\delta\dot{u}_i$ is zero, and on the surface Γ_{ω_c} where $\dot{\omega}_k^c$ is prescribed and $\delta\dot{\omega}_k^c$ is zero. In addition, Γ_u, Γ_{ω_c}, Γ_t and Γ_m are mutually exclusive, i.e. $\Gamma_u \cup \Gamma_t = \Gamma_{\omega^c} \cup \Gamma_m = \Gamma$ and $\Gamma_u \cap \Gamma_t = \Gamma_{\omega^c} \cap \Gamma_m = 0$.

With respect of $t_i = \sigma_{ij} n_j$ on Γ_t, $m_k = \mu_{kj} n_j$ on Γ_m, $\delta\dot{u}_i = 0$ on Γ_u, $\delta\dot{\omega}_k^c = 0$ on Γ_ω and the definitions of

$$\delta\dot{\varepsilon}_{ij}^c = \delta L_{ij} - \delta\bar{\Omega}_{ij} = \frac{\partial(\delta\dot{u}_i)}{\partial x_j} + \epsilon_{ijk}\delta\dot{\omega}_k^c \quad \text{and} \quad \delta\dot{\kappa}_{kj} = \frac{\partial(\delta\dot{\omega}_k^c)}{\partial x_j},$$

the weak form of the virtual power equation can be written as

$$\int_{\mathcal{B}} \left[\delta\dot{\varepsilon}^c_{ij}\,\sigma_{ij} \;+\; \delta\dot{\kappa}_{kj}\,\mu_{kj}\right]\,dV \;=\; \int_{\Gamma_t} \delta\dot{u}_i t_i\,d\Gamma_t \;+\; \int_{\Gamma_m} \delta\dot{\omega}^c_k m_k\,d\Gamma_m + \\ + \int_{\mathcal{B}} \left[\delta\dot{u}_i\,\rho b_i \;+\; \delta\dot{\omega}^c_k\,\rho c_k\right]\,dV. \tag{2.47}$$

2.4.2 Adaptation to plane strain condition

For plane strain condition, a point in a Cosserat continuum possesses two translational degrees of freedom, i.e. u_1, u_2, and one rotation degree of freedom ω^c_3. The non-zero stress and couple stress components for plane strain condition are shown in Fig. 2.3. For plane strain the local equilibrium equations 2.26 and 2.29 become:

$$\begin{aligned} \frac{\partial\sigma_{11}}{\partial x_1} + \frac{\partial\sigma_{12}}{\partial x_2} + \rho b_1 = 0, \\ \frac{\partial\sigma_{21}}{\partial x_1} + \frac{\partial\sigma_{22}}{\partial x_2} + \rho b_2 = 0, \\ \frac{\partial\mu_{31}}{\partial x_1} + \frac{\partial\mu_{32}}{\partial x_2} - (\sigma_{12} - \sigma_{21}) + \rho c_3 = 0. \end{aligned} \tag{2.48}$$

With respect to the following matrix representation of the generalized quantities

$$\begin{aligned} \dot{\mathbf{E}} &= [\dot{\varepsilon}^c_{11}, \dot{\varepsilon}^c_{22}, 0, \dot{\varepsilon}^c_{12}, \dot{\varepsilon}^c_{21}, d_{50}\dot{\kappa}_{31}, d_{50}\dot{\kappa}_{32}]^T, \\ \mathbf{S} &= [\sigma_{11}, \sigma_{22}, \sigma_{33}, \sigma_{12}, \sigma_{21}, \mu_{31}, \mu_{32}]^T, \\ \dot{\mathbf{u}} &= [\dot{u}_1, \dot{u}_2, \dot{\omega}^c_3]^T, \\ \bar{\mathbf{t}}^T &= [\bar{t}_1, \bar{t}_2, \bar{m}_3], \\ \mathbf{f}^T &= [\rho b_1, \rho b_2, \rho c_3], \end{aligned}$$

the corresponding virtual power equation for plane strain may be written as

$$\int_{\mathcal{B}} \delta\dot{\mathbf{E}}^T.\mathbf{S}\,dV = \int_{\Gamma} \delta\dot{\mathbf{u}}^T.\bar{\mathbf{t}}\,d\Gamma + \int_{\mathcal{B}} \delta\dot{\mathbf{u}}^T.\mathbf{f}\,dV. \tag{2.49}$$

The constitutive equations 2.34 and 2.35 can be represented in matrix notations as

$$\mathring{\mathbf{S}} \;=\; \mathbf{H}\,.\,\dot{\mathbf{E}}, \tag{2.50}$$

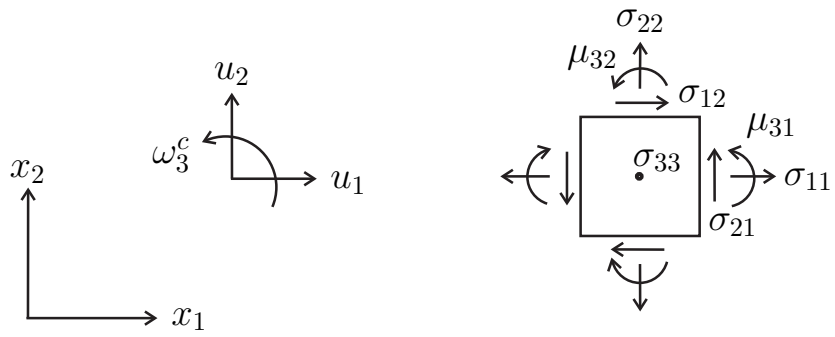

Figure 2.3: Kinematic variables (u_1, u_2, ω_3^c), stress components (σ_{11}, σ_{22}, σ_{33}, σ_{12}, σ_{21}) and couple stress components (μ_{31}, μ_{32}) in Cosserat continuum for plane strain condition.

where $\mathbf{H}$ is the constitutive matrix with the dimension (7×7) given by

$$\mathbf{H} = \begin{bmatrix} \mathbf{H}_{\sigma\sigma} & \mathbf{H}_{\sigma\mu} \\ \mathbf{H}_{\mu\sigma} & \mathbf{H}_{\mu\mu} \end{bmatrix}. \tag{2.51}$$

$\mathbf{H}_{\sigma\sigma}$, $\mathbf{H}_{\sigma\mu}$, $\mathbf{H}_{\mu\sigma}$, $\mathbf{H}_{\mu\mu}$ are nested matrices of matrix $\mathbf{H}$ with different dimensions (Huang, 2000 [60]):

$$\mathbf{H}_{\sigma\sigma} = f_s \left(\hat{a}^2\, \mathbf{I_5} + \hat{\mathbf{S}}_\sigma . \hat{\mathbf{S}}_\sigma^T + \frac{f_d\, \hat{a}}{\|\dot{\mathbf{E}}\|} \left(\hat{\mathbf{S}}_\sigma + \hat{\mathbf{S}}_\sigma^d \right) . \dot{\mathbf{E}}_\sigma^T \right),$$

$$\mathbf{H}_{\sigma\mu} = f_s \left(\hat{\mathbf{S}}_\sigma . \hat{\mathbf{S}}_\mu^T + \frac{f_d\, \hat{a}}{\|\dot{\mathbf{E}}\|} \left(\hat{\mathbf{S}}_\sigma + \hat{\mathbf{S}}_\sigma^d \right) . \dot{\mathbf{E}}_\mu^T \right),$$

$$\mathbf{H}_{\mu\sigma} = d_{50}\, f_s \left(\hat{\mathbf{S}}_\mu . \hat{\mathbf{S}}_\sigma^T + \frac{f_d\, 2\, a_m}{\|\dot{\mathbf{E}}\|} \hat{\mathbf{S}}_\mu . \dot{\mathbf{E}}_\sigma^T \right),$$

$$\mathbf{H}_{\mu\mu} = d_{50}\, f_s \left(a_m^2\, \mathbf{I_2} + \hat{\mathbf{S}}_\mu . \hat{\mathbf{S}}_\mu^T + \frac{f_d\, 2\, a_m}{\|\dot{\mathbf{E}}\|} \hat{\mathbf{S}}_\mu . \dot{\mathbf{E}}_\mu^T \right),$$

where:

$$\mathbf{I}_5 = \begin{bmatrix} 1 & 0 & 0 & 0 & 0 \\ 0 & 1 & 0 & 0 & 0 \\ 0 & 0 & 1 & 0 & 0 \\ 0 & 0 & 0 & 1 & 0 \\ 0 & 0 & 0 & 0 & 1 \end{bmatrix}, \quad \mathbf{I}_3 = \begin{bmatrix} 1 & 0 & 0 \\ 0 & 1 & 0 \\ 0 & 0 & 1 \end{bmatrix}, \quad \mathbf{I}_2 = \begin{bmatrix} 1 & 0 \\ 0 & 1 \end{bmatrix},$$

$$\hat{\mathbf{S}}_\sigma = \left[\frac{\sigma_{11}}{\sigma_{kk}}, \frac{\sigma_{22}}{\sigma_{kk}}, \frac{\sigma_{33}}{\sigma_{kk}}, \frac{\sigma_{12}}{\sigma_{kk}}, \frac{\sigma_{21}}{\sigma_{kk}}\right]^T, \quad \hat{\mathbf{S}}_\mu = \left[\frac{\mu_{31}}{d_{50}\sigma_{kk}}, \frac{\mu_{32}}{d_{50}\sigma_{kk}}\right]^T,$$

$$\hat{\mathbf{S}}^d_\sigma = \left[\frac{\sigma_{11}}{\sigma_{kk}} - \frac{1}{3}, \frac{\sigma_{22}}{\sigma_{kk}} - \frac{1}{3}, \frac{\sigma_{33}}{\sigma_{kk}} - \frac{1}{3}, \frac{\sigma_{12}}{\sigma_{kk}}, \frac{\sigma_{21}}{\sigma_{kk}}\right]^T,$$

$$\dot{\mathbf{E}}_\sigma = [\dot{\varepsilon}^c_{11}, \dot{\varepsilon}^c_{22}, 0, \dot{\varepsilon}^c_{12}, \dot{\varepsilon}^c_{21}]^T, \quad \dot{\mathbf{E}}_\mu = [d_{50}\dot{\kappa}_{31}, d_{50}\dot{\kappa}_{32}]^T,$$

$$\sigma_{kk} = \sigma_{11} + \sigma_{22} + \sigma_{33}, \qquad \|\dot{\mathbf{E}}\| = \sqrt{\dot{\mathbf{E}}^T_\sigma.\dot{\mathbf{E}}_\sigma + \dot{\mathbf{E}}^T_\mu.\dot{\mathbf{E}}_\mu}.$$

The Jaumann-Zaremba objective stress rates $\mathring{\sigma}_{ij}$ and couple stress rates $\mathring{\mu}_{3j}$ are related to the time derivative of the corresponding stress components, i.e. $\dot{\sigma}_{ij}$, and to the time derivative of the corresponding couple stress components, i.e. $\dot{\mu}_{3j}$ as

$$\begin{aligned}
\dot{\sigma}_{11} &= \mathring{\sigma}_{11} + W_{12}\,(\sigma_{12} + \sigma_{21}) \\
\dot{\sigma}_{22} &= \mathring{\sigma}_{22} - W_{12}\,(\sigma_{12} + \sigma_{21}) \\
\dot{\sigma}_{33} &= \mathring{\sigma}_{33} \\
\dot{\sigma}_{12} &= \mathring{\sigma}_{12} - W_{12}\,(\sigma_{11} - \sigma_{22}) \\
\dot{\sigma}_{21} &= \mathring{\sigma}_{21} - W_{12}\,(\sigma_{11} - \sigma_{22}) \\
\dot{\mu}_{31} &= \mathring{\mu}_{31} + W_{12}\,\mu_{32} \\
\dot{\mu}_{32} &= \mathring{\mu}_{32} - W_{12}\,\mu_{31}
\end{aligned}$$

with

$$\begin{aligned}
\mathring{\sigma}_{11} &= f_s \Big[\hat{a}^2\,\dot{\varepsilon}^c_{11} + P\,\hat{\sigma}_{11} + f_d\,\hat{a}\,(2\hat{\sigma}_{11} - 1/3)\,\sqrt{R}\Big],\\
\mathring{\sigma}_{22} &= f_s \Big[\hat{a}^2\,\dot{\varepsilon}^c_{22} + P\,\hat{\sigma}_{22} + f_d\,\hat{a}\,(2\hat{\sigma}_{22} - 1/3)\,\sqrt{R}\Big],\\
\mathring{\sigma}_{33} &= f_s \Big[P\,\hat{\sigma}_{33} + f_d\,\hat{a}\,(2\hat{\sigma}_{33} - 1/3)\,\sqrt{R}\Big],\\
\mathring{\sigma}_{12} &= f_s \Big[\hat{a}^2\,\dot{\varepsilon}^c_{12} + P\,\hat{\sigma}_{12} + 2\,f_d\,\hat{a}\,\hat{\sigma}_{12}\,\sqrt{R}\Big],\\
\mathring{\sigma}_{21} &= f_s \Big[\hat{a}^2\,\dot{\varepsilon}^c_{21} + P\,\hat{\sigma}_{21} + 2\,f_d\,\hat{a}\,\hat{\sigma}_{21}\,\sqrt{R}\Big],\\
\mathring{\mu}_{31} &= d_{50}\,f_s \Big[a_m^2\,d_{50}\dot{\kappa}_{31} + P\,\hat{\mu}_{31} + 2\,f_d\,a_m\,\hat{\mu}_{31}\,\sqrt{R}\Big],\\
\mathring{\mu}_{32} &= d_{50}\,f_s \Big[a_m^2\,d_{50}\dot{\kappa}_{32} + P\,\hat{\mu}_{32} + 2\,f_d\,a_m\,\hat{\mu}_{32}\,\sqrt{R}\Big],
\end{aligned}$$

where

$$\begin{aligned}
P &= \hat{\sigma}_{11}\,\dot{\varepsilon}^c_{11} + \hat{\sigma}_{22}\,\dot{\varepsilon}^c_{22} + \hat{\sigma}_{12}\,\dot{\varepsilon}^c_{12} + \hat{\sigma}_{21}\,\dot{\varepsilon}^c_{21} + \hat{\mu}_{31}\,d_{50}\,\dot{\kappa}_{31} + \hat{\mu}_{32}\,d_{50}\,\dot{\kappa}_{32},\\
R &= \dot{\varepsilon}^{c\,2}_{11} + \dot{\varepsilon}^{c\,2}_{22} + \dot{\varepsilon}^{c\,2}_{12} + \dot{\varepsilon}^{c\,2}_{21} + d_{50}^2\,\dot{\kappa}_{31}^2 + d_{50}^2\,\dot{\kappa}_{32}^2\,.
\end{aligned}$$

2.4.3 Element formulation and finite element procedure

Following Huang (2000) [60] a four node quadrilateral isoparametric finite element with two translational degrees of freedom, i.e. u_1, u_2, and one rotational degree of freedom, i.e. ω_3^c, at each node is used. Thus, the same interpolation for the displacements and the coordinates is applied. Within the finite element the interpolation for $\mathbf{X} = [X_1, X_2]^T$, $\mathbf{x} = [x_1, x_2]^T$, the generalized displacement $\mathbf{u} = [u_1, u_2, \omega_3^c]^T$, the generalized velocity $\dot{\mathbf{u}} = [\dot{u}_1, \dot{u}_2, \dot{\omega}_3^c]^T$, the generalized strain rate $\dot{\mathbf{E}} = [\dot{\varepsilon}^c_{11}, \dot{\varepsilon}^c_{22}, 0, \dot{\varepsilon}^c_{12}, \dot{\varepsilon}^c_{21}, d_{50}\dot{\kappa}_{31}, d_{50}\dot{\kappa}_{32}]^T$, the generalized virtual velocity $\delta\dot{\mathbf{u}} = [\delta\dot{u}_1, \delta\dot{u}_2, \delta\dot{\omega}_3^c]^T$ and the generalized virtual strain rate $\delta\dot{\mathbf{E}} = [\delta\dot{\varepsilon}^c_{11}, \delta\dot{\varepsilon}^c_{22}, 0, \delta\dot{\varepsilon}^c_{12}, \delta\dot{\varepsilon}^c_{21}, d_{50}\delta\dot{\kappa}_{31}, d_{50}\delta\dot{\kappa}_{32}]^T$ is given by

$$\mathbf{u} = \sum_{\alpha=1}^{4} N^\alpha \mathbf{I}_3 \mathbf{u}^\alpha, \tag{2.52}$$

$$\mathbf{X} = \sum_{\alpha=1}^{4} N^\alpha \mathbf{I}_2 \mathbf{X}^\alpha, \qquad \mathbf{x} = \sum_{\alpha=1}^{4} N^\alpha \mathbf{I}_2 \mathbf{x}^\alpha, \tag{2.53}$$

$$\dot{\mathbf{u}} = \sum_{\alpha=1}^{4} N^{\alpha} \mathbf{I}_3 \dot{\mathbf{u}}^{\alpha}, \qquad \delta\dot{\mathbf{u}} = \sum_{\alpha=1}^{4} N^{\alpha} \mathbf{I}_3 \delta\dot{\mathbf{u}}^{\alpha}, \tag{2.54}$$

$$\dot{\mathbf{E}} = \sum_{\alpha=1}^{4} \boldsymbol{\beta}^{\alpha} \dot{\mathbf{u}}^{\alpha}, \qquad \delta\dot{\mathbf{E}} = \sum_{\alpha=1}^{4} \boldsymbol{\beta}^{\alpha} \delta\dot{\mathbf{u}}^{\alpha}, \tag{2.55}$$

where: N^{α} is a standard bilinear shape function with respect to the node α, i.e. ($\alpha = 1, 2, 3, 4$) and

$$\boldsymbol{\beta}^{\alpha\,T} = \begin{bmatrix} \dfrac{\partial N^{\alpha}}{\partial x_1} & 0 & 0 & \dfrac{\partial N^{\alpha}}{\partial x_2} & 0 & 0 & 0 \\ 0 & \dfrac{\partial N^{\alpha}}{\partial x_2} & 0 & 0 & \dfrac{\partial N^{\alpha}}{\partial x_1} & 0 & 0 \\ 0 & 0 & 0 & 1 & -1 & d_{50}\dfrac{\partial N^{\alpha}}{\partial x_1} & d_{50}\dfrac{\partial N^{\alpha}}{\partial x_2} \end{bmatrix}. \tag{2.56}$$

In particular, the shape function for the node α reads

$$N^{\alpha} = \frac{1}{4}\left(1 + \xi_1^{\alpha}\xi_1\right)\left(1 + \xi_2^{\alpha}\xi_2\right), \tag{2.57}$$

and $(\xi_1^{\alpha}, \xi_2^{\alpha})$ denotes the local coordinates of node α in the master element as shown for example in Fig. 2.4.

α	1	2	3	4
ξ_1^{α}	-1	1	1	-1
ξ_2^{α}	-1	-1	1	1

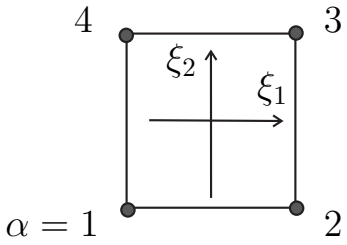

Figure 2.4: Nodes in the master element.

According to Nagtegaal et al. (1974) [87], a selective reduced integration technique can be used to avoid volumetric locking. In the selective reduced integration technique, only a one-point Gauss integration is used to compute the volume change while a four-point Gauss integration is applied for the stresses and couple stresses. Following Hughes (1980) [65] the selective reduced integration technique can be implemented by changing matrix $\boldsymbol{\beta}^{\alpha}$ in Eq. 2.56 with the following

matrix $\bar{\boldsymbol{\beta}}^{\alpha}$:

$$\overline{\boldsymbol{\beta}}^{\alpha} = \begin{bmatrix} \frac{1}{2}\left(\frac{\overline{\partial N^{\alpha}}}{\partial x_1} + \frac{\partial N^{\alpha}}{\partial x_1}\right) & \frac{1}{2}\left(\frac{\overline{\partial N^{\alpha}}}{\partial x_2} - \frac{\partial N^{\alpha}}{\partial x_2}\right) & 0 \\ \frac{1}{2}\left(\frac{\overline{\partial N^{\alpha}}}{\partial x_1} - \frac{\partial N^{\alpha}}{\partial x_1}\right) & \frac{1}{2}\left(\frac{\overline{\partial N^{\alpha}}}{\partial x_2} + \frac{\partial N^{\alpha}}{\partial x_2}\right) & 0 \\ 0 & 0 & 0 \\ \frac{\partial N^{\alpha}}{\partial x_2} & 0 & 1 \\ 0 & \frac{\partial N^{\alpha}}{\partial x_1} & -1 \\ 0 & 0 & d_{50}\frac{\partial N^{\alpha}}{\partial x_1} \\ 0 & 0 & d_{50}\frac{\partial N^{\alpha}}{\partial x_2} \end{bmatrix}, \tag{2.58}$$

where

$$\frac{\overline{\partial N^{\alpha}}}{\partial x_i} = \frac{1}{V^e}\int\limits_{V^e} \frac{\partial N^{\alpha}}{\partial x_i}\, dV.$$

$\partial N^{\alpha}/\partial x_j$ in $\overline{\boldsymbol{\beta}}^{\alpha}$ and $\boldsymbol{\beta}^{\alpha}$ needs to be computed based on the following relation

$$\frac{\partial N^{\alpha}}{\partial x_j} = \frac{\partial N^{\alpha}}{\partial \xi_1}\frac{\partial \xi_1}{\partial x_j} + \frac{\partial N^{\alpha}}{\partial \xi_2}\frac{\partial \xi_2}{\partial x_j}. \tag{2.59}$$

$\partial N^{\alpha}/\partial \xi_1$ and $\partial N^{\alpha}/\partial \xi_2$ can be derived from Eq. 2.57 to

$$\frac{\partial N^{\alpha}}{\partial \xi_1} = \frac{1}{4}\xi_1^{\alpha}\,(1+\xi_2^{\alpha}\xi_2) \quad \text{and} \quad \frac{\partial N^{\alpha}}{\partial \xi_2} = \frac{1}{4}\xi_2^{\alpha}\,(1+\xi_1^{\alpha}\xi_1). \tag{2.60}$$

$\partial \xi_i/\partial x_j$ is the inverse of the isoparametric transformation from the current configuration of the finite element to the master element

$$\frac{\partial \xi_i}{\partial x_j} = \left[\frac{\partial x_i}{\partial \xi_j}\right]^{-1}, \tag{2.61}$$

where

$$\frac{\partial x_i}{\partial \xi_j} = \frac{\partial}{\partial \xi_j}\left(X_i + u_i\right) = \frac{\partial X_i}{\partial \xi_j} + \frac{\partial u_i}{\partial \xi_j}.$$

With respect to the element interpolation for $\mathbf{X}$ (Eq. 2.53) and $\mathbf{u}$ (Eq. 2.52) the following relation can be obtained

$$\frac{\partial x_i}{\partial \xi_j} = \sum_{\alpha=1}^{4} X_i^{\alpha} \frac{\partial N^{\alpha}}{\partial \xi_j} + \sum_{\alpha=1}^{4} u_i^{\alpha} \frac{\partial N^{\alpha}}{\partial \xi_j}. \tag{2.62}$$

By substituting Eqs. 2.52 - 2.55 into the virtual power equation 2.49, it follows for the single finite element

$$\sum_{\alpha=1}^{4} \delta\dot{\mathbf{u}}^{\alpha T} \int_{V_e} \boldsymbol{\beta}^{\alpha T}.\mathbf{S} = \sum_{\alpha=1}^{4} \delta\dot{\mathbf{u}}^{\alpha T} \left(\int_{S_e} (N^{\alpha}\mathbf{I}_3)^T.\bar{\mathbf{t}}\, dS + \int_{V_e} (N^{\alpha}\mathbf{I}_3)^T.\mathbf{f}\, dV \right), \tag{2.63}$$

where V_e and S_e are the volume and surface area of an element, respectively.

Following the standard procedure in finite element programming (e.g. Hinton & Owen, 1977), the summation of Eq. 2.63 through all elements of the discretized global structure can be written in the terms of the global node sequence as

$$\sum_{K=1}^{NNODE} \mathbf{R}^K\, \delta\dot{\mathbf{u}}^K = 0 \quad \text{with} \quad \mathbf{R}^K = \mathbf{R}^K(\mathbf{u}^L), \tag{2.64}$$

where the upper case letters K and L indicate nodes in the global node sequence, $NNODE$ is the total node number ($K, L = 1, 2, ..., NNODE$), $\mathbf{R}^K$ is the residual force at node K depending on the generalized displacement $\mathbf{u}$ and $\delta\dot{\mathbf{u}}^K$ is the generalized virtual velocity. $\mathbf{R}^K$ is computed from the summation of relevant contributions to the node K from the surrounding elements of the global system, where the element contribution $\mathbf{R}_e^{\alpha}$ for $\mathbf{R}^K$ can be computed according to

$$\mathbf{R}_e^{\alpha} = \int_{Se} (N^{\alpha}\mathbf{I}_3)^T.\bar{\mathbf{t}}\, dS + \int_{Ve} (N^{\alpha}\mathbf{I}_3)^T.\mathbf{f}\, dV - \int_{Ve} \boldsymbol{\beta}^{\alpha T}.\mathbf{S}\, dV. \tag{2.65}$$

As $\delta\dot{\mathbf{u}}^K$ in Eq. 2.64 are independent variables which can be set to zero except for one degree of freedom in the system, the equilibrium equation obtained for each node is as follows

$$\mathbf{R}^K(\mathbf{u}^L) = 0. \tag{2.66}$$

Due to strong nonlinearity of the equation system, the Newton-Raphson iteration method is adopted. If the equilibrium equation 2.66 is satisfied by $\mathbf{u}_{t0}^L$ at time $t0$, the new equilibrium for a load increment with respect to the increment of the nodal variable $\Delta\mathbf{u}^L = \mathbf{u}_{t0+\Delta t}^L - \mathbf{u}_{t0}^L$ can be written as

$$\mathbf{R}^K\left(\mathbf{u}_{t0}^L + \Delta\mathbf{u}^L\right) = 0. \tag{2.67}$$

With respect to the global tangential stiffness $\mathbf{K}^{KL}$ the Newton-Raphson iteration can be written as

$$\mathbf{K}_i^{KL}\,\Delta\mathbf{u}_{i+1}^L = \mathbf{R}_i^K, \tag{2.68}$$

with $\mathbf{K}_i^{KL} = (\delta\mathbf{R}^K)/(\delta\mathbf{u}^L)\,(\mathbf{u}_i^M)$ and $\mathbf{u}_{i+1}^L = \mathbf{u}_i^L + \Delta\mathbf{u}_{i+1}^L$. Herein, the subscript i ($i = 0, 1, 2, ...$) denotes the number of iterations with $\mathbf{u}_0^L = \mathbf{u}_{t0}^L$ and $\mathbf{R}_0^K = \mathbf{R}^K(\mathbf{u}_{t0}^L)$.

The initial guess can be computed according to $\mathbf{K}_0^{KL}\Delta\mathbf{u}_1^L = \Delta\mathbf{R}^K$, where $\Delta\mathbf{R}^K$ can be obtained from Eq. 2.65 with

$$\Delta\mathbf{R}_e^\alpha = \int_{Se} (N^\alpha\mathbf{I_3})^T.\bar{\mathbf{t}}_{t0+\Delta t}\,dS + \int_{Ve} (N^\alpha\mathbf{I_3})^T.\mathbf{f}_{t0+\Delta t}\,dV - \int_{Ve} \overline{\boldsymbol{\beta}}^{\alpha T}.\mathbf{S}_{t0}\,dV.$$

The global tangential stiffness matrix $\mathbf{K}^{KL}$ in Eq. 2.68 can be computed from the element stiffness matrix $\mathbf{K}_e^{\alpha\beta}$ according to the sequence of the degree of freedom in the discrete system:

$$\begin{aligned}\mathbf{K}_e^{\alpha\beta} = &\int_{Ve} \overline{\boldsymbol{\beta}}^{\alpha T}\,\mathbf{H}\,\overline{\boldsymbol{\beta}}^{\beta}\,dV + \int_{Ve} \frac{\delta\overline{\boldsymbol{\beta}}^{\alpha T}}{\delta\mathbf{u}^\beta}\,\mathbf{S}\,dV + \int_{Ve} \overline{\boldsymbol{\beta}}^{\alpha T}\,\mathbf{S}\,\frac{\delta J}{\delta\mathbf{u}^\beta}\,\frac{1}{J}\,dV \\ &- \int_{Se} (N^\alpha\mathbf{I_3})^T\,\mathbf{Q}_s^\beta\,dS - \int_{Ve} (N^\alpha\mathbf{I_3})^T\,\mathbf{Q}_v^\beta\,dV.\end{aligned} \tag{2.69}$$

Herein, $\mathbf{Q}_s^\beta$ and $\mathbf{Q}_v^\beta$ denote the load contribution to the global stiffness:

$$\mathbf{Q}_s^\beta = \frac{\delta\bar{\mathbf{t}}}{\delta\mathbf{u}^\beta} + \frac{1}{A_r}\,\bar{\mathbf{t}}\,\frac{\delta A_r}{\delta\mathbf{u}^\beta},$$

$$\mathbf{Q}_s^\beta = \frac{\delta\bar{\mathbf{f}}}{\delta\mathbf{u}^\beta} + \frac{1}{J}\,\bar{\mathbf{f}}\,\frac{\delta J}{\delta\mathbf{u}^\beta},$$

with $J = dV/dV_0$ and $A_r = dS/dS_0$ are the ratio of a volume element and the ratio of a surface element, respectively.

2.4.4 Time integration scheme

For a rate independent material behavior, a fictitious time scale can be introduced for quasi-static loading process. A loading step is divided into increments which corresponds to the division of the time domain into time increments. For a generalized displacement increment computed for a time interval $[t0,\ t1 = t0 + \Delta t]$, the stresses σ_{ij}, couple stresses μ_{3j} and void ratio e are to be updated by integrating the constitutive equations at Gauss points within each element. Following Huang (2000) [60] the detail updating process with a one-step implicit time integration method and sub-time stepping scheme can be explained as follows:

Providing the void ratio e_{t0} at time $t0$ is known, the void ratio at time $t1$ can be computed according to

$$e_{t1} = (1 + e_{t0})\ \exp[\Delta\epsilon_v] - 1, \tag{2.70}$$

where $\Delta\epsilon_v = \Delta\epsilon^c_{11} + \Delta\epsilon^c_{22}$ is the increment of the volumetric strain.

With respect to the known value of the generalized stress $\mathbf{S}_{t0}$ at time $t0$, the generalized stress at time $t1$ is updated according to

$$\mathbf{S}_{t1} = \mathbf{S}_{t0}\ +\ \Delta\mathbf{S}. \tag{2.71}$$

Herein, an iteration procedure for the evaluation of the general stress increment $\Delta\mathbf{S}$ is required. The $(j+1)$th estimation for the generalized stress increment reads

$$\Delta\mathbf{S}^{j+1}\ =\ \mathbf{H}\left(\mathbf{S}^{j}_{t0+\theta\Delta t}, e_{t0+\theta\Delta t}, \frac{\Delta\mathbf{E}}{\|\Delta\mathbf{E}\|}\right).\Delta\mathbf{E}, \tag{2.72}$$

where

$$\mathbf{S}^{j+1}_{t1} = \mathbf{S}_{t0}\ +\ \Delta\mathbf{S}^{j+1}, \tag{2.73}$$

$$\begin{aligned}\mathbf{S}_{t0+\theta\Delta t}\ &=\ (1-\theta)\mathbf{S}_{t0} + \theta\mathbf{S}_{t1} = \mathbf{S}_{t0} + \theta\Delta\mathbf{S},\\ e_{t0+\theta\Delta t}\ &=\ (1-\theta)e_{t0} + \theta e_{t1},\end{aligned}$$

with $\theta \in [0, 1]$. According to Buchanan and Turner (1992) the integration scheme is unconditionally stable for $\theta \geq 0.5$. The iteration stops if the following condition is fulfilled

$$R = \frac{\|\Delta\mathbf{S}^{j+1} - \Delta\mathbf{S}^{j}\|}{\|\Delta\mathbf{S}^{j}\|}\ \leq\ \epsilon_{TOL}, \tag{2.74}$$

with a prescribed tolerance ϵ_{TOL}. When the total number of iteration is reached, i.e. $j = niter$, and the requirement 2.74 is not yet fulfilled, the sub-time stepping is initiated by reducing the time increment by a half. In order to prevent the infinite sub-stepping, a lower bound is defined, i.e. the integration scheme fails for the sub-time increment less than $(\varepsilon_{time} * \Delta t)$, with ε_{time} is a prescribed positive scalar (e.g. Huang, 2000 [60]). The flowchart of the algorithm is shown in Fig. 2.5.

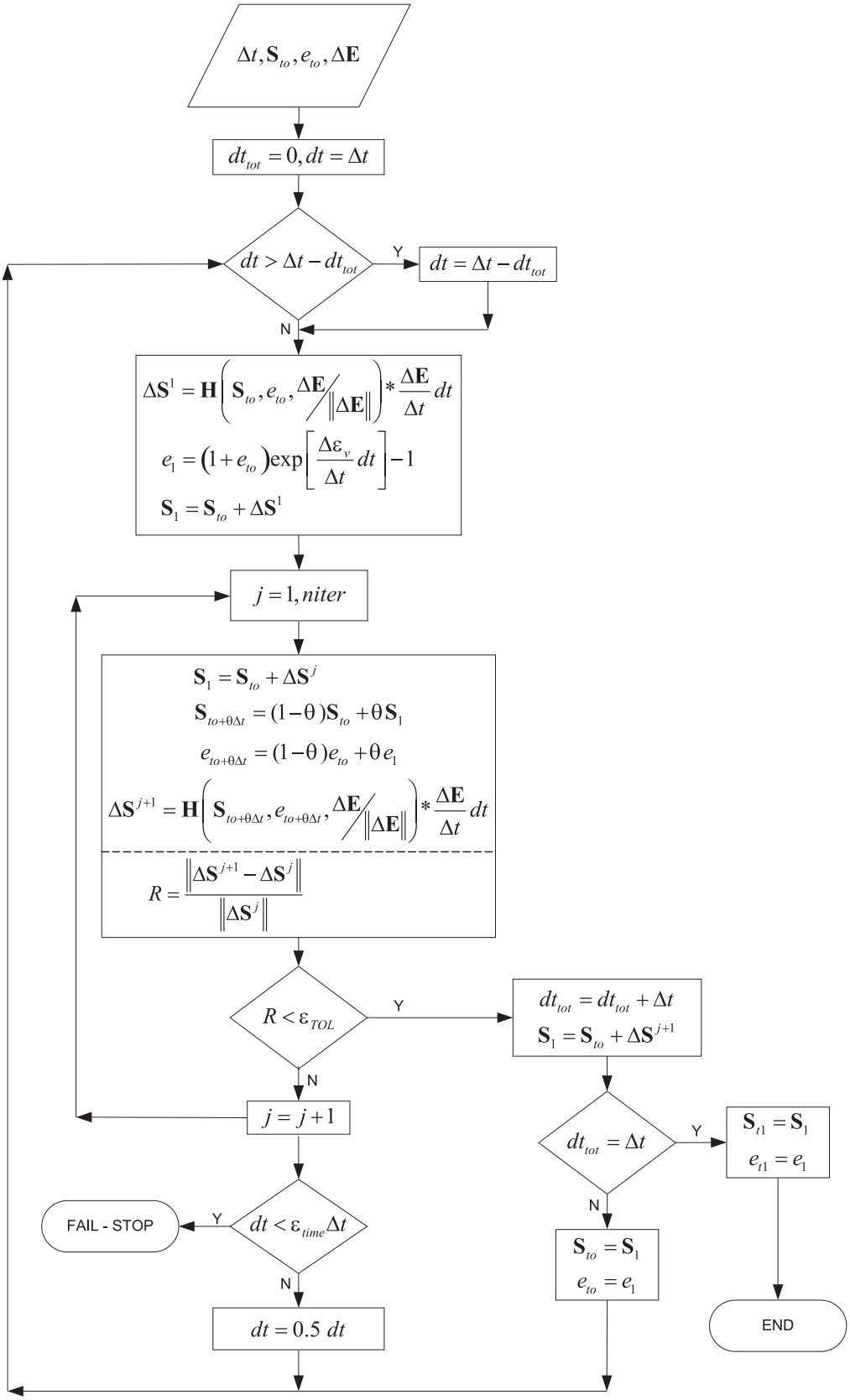

Figure 2.5: Flowchart of time integration scheme for the micro-polar hypoplastic model (after Huang, 2000 [60]).

3 SOIL STRUCTURE INTERACTION

The mechanical properties of the interface behavior between soil and the bounding structures under shearing can be of great importance in many geotechnical applications such as shallow foundations, retaining walls, tunnels and reinforced soil structures (e.g. Gudehus, 1994 [50], 1999 [53]). Therefore, the investigations of the soil-structure interface have attracted great attentions of many researchers. Field observations, laboratory experiments and numerical simulations have been conducted in order to gain insights into the complex phenomena in the soil body close to the surface of the bounding structure. Experiments such as direct shear test (e.g. Potyondy, 1961 [97]; Jewell & Wroth, 1987 [67]; Paikowsky et al., 1995 [94]; Tejchman & Wu, 1995 [117]; Frost et al., 2002 [43]; DeJong & Frost, 2002 [33]) simple shear test (Uesugi & Kishida, 1986a [119]; Uesugi & Kishida, 1986b [118]; Uesugi et al., 1988 [120]), pullout test (e.g. Ingold, 1983 [66]; Bauer & Mowafy, 1988 [15]; Palmiera & Milligan, 1989 [95]; Bergado et al., 1996 [19]) and ring torsional test (e.g. Yoshimi & Kishida, 1981 [127]; Garga & Sedano, 2002 [46]) had been carried out to investigate the deformation behavior of the soil close to the interface and the shear resistance between granular materials and bounding structures with different surface roughness. The surface roughness is usually defined as the difference between the highest peak and the lowest trough along the surface profile.

Experiments show an evidence of the influence of the mean grain size, the density of the granular material, the surface roughness and the stiffness of the bounding structure (e.g. Potyondy, 1961 [97]; Uesugi & Kishida, 1986a [119]; Boulon, 1989 [23]; Paikowsky et al., 1995 [94];

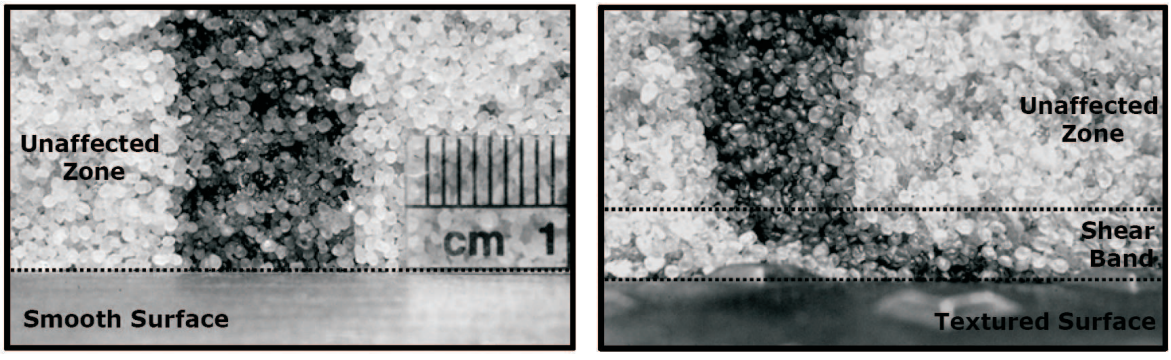

(**a**) (**b**)

Figure 3.1: Shearing of granular materials on the (**a**) smooth surface and (**b**) rough surface (After DeJong & Frost, 2002 [33]).

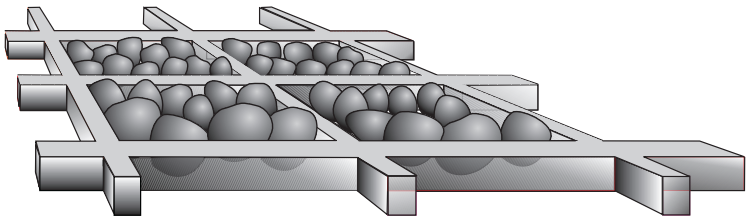

Figure 3.2: Interlocking of soil particles within the cells of geogrid reinforcement.

Tejchman & Wu, (1995) [117]; DeJong & Frost, 2002 [33]; Frost et al., 2002 [43]) and the type of the tests (e.g. Uesugi & Kishida, 1986b [118]; Tejchman & Wu, 1995 [117]; Tejchman, 2004 [110]) on the shear resistance at the interface and on the corresponding displacement field inside the granular body.

In particular, the influence of the surface roughness of the bounding structure on the deformation behavior of the granular body can be clearly observed in Fig. 3.1. In this experiment, the shear tests were conducted on compacting alternating layers of dyed/non-dyed sub-rounded sand which were placed on top of the interchangeable steel-alloy sleeve. After a certain shear displacement the deformations of the sand specimens are shown in Figs. 3.1(a) - 3.1(b) for the smooth and the rough surfaces of a steel-alloy sleeve, respectively. In Fig. 3.1(a) shear deformations in the sand body cannot be detected. Thus, the sand specimen behaves like a rigid body during shearing. This also means that the slippage occurs at the interface, and the shear resistance at the interface is lower than in the granular body (e.g. Potyondy, 1960 [97]; Jewell & Wroth, 1987 [67]; Bauer & Mowafy, 1988 [15]; Bergado et al., 1996 [19], 2003 [20]). On the contrary, when a textured steel-alloy sleeve is sheared against the granular body, a part of the soil particles are interlocked by the rough surface of the steel-alloy sleeve (Fig. 3.1(b)). Therefore, the displacement of soil particles at the interface is mainly dictated by displacement of the bounding structure. The distribution of the shear deformation across the height of the granular body is nonlinear (e.g. Garga & Infante Sedano, 2002 [46]). After large shearing the shear deformation is localized within a zone in the granular body close to the surface of the bounding structure, as shown in Fig. 3.1(b). This zone is called shear band. The granular body outside of the shear band is almost not affected. Furthermore, the occurrence of the interlocking of soil particles at the interface is mainly related with the interaction between the surface roughness of the bounding structure, the grain size and the surface roughness of the grains. The shear resistance at the interface is not constant during shearing (e.g. Tejchman & Wu (1995) [117]). With the increase of shearing the shear resistance at the interface first increases up to the peak and then it can decrease toward a stationary value. In addition to the sliding of the soil particles at the interface, Uesugi et al. (1988) [120] reported that the soil particles at the interface may also rotate.

The aim of this chapter is to investigate the deformation behavior of a granular soil close to a bounding structure under shearing. Due to shearing parallel to the bounding structure the soil grains at the interface between the granular body and the bounding structure can generally translate relatively to the surface of the bounding structure and they can also rotate. In the

present study, only cases where the grains at the interface are captured by the rough surface of the bounding structure are considered. An example for such rough bounding structures is a geogrid in a reinforced soil structure. As sketched in Fig. 3.2 the interlocking of the soil grains within the geogrid cells are dominant (e.g. Bauer & Mowafy, 1988 [15]; Konietzky et al., 2004 [78]). Although the displacement of the grains at the interface is mainly dictated by the displacement of the bounding structure, the soil grains can rotate. In this context it is important to distinguish between rotation of the particles with and without a relative displacement of the center of the mass of the particles (e.g. Bauer & Huang, 2004 [12]). The rotation resistance of the grains at the interface is related to some factors such as the shape and surface roughness of the grains and the ratio between the grain size and the surface roughness of the bounding structure. For instance along the interface of a geogrid (Fig. 3.2) the rotation resistance of the grains located within the geogrid cells may be different as the rotation resistance of grains in contact with the smooth surface of the members of the geogrid. Analytical investigations (e.g. Unterreiner et al., 1994 [121]; Bauer, 2005 [8]) and numerical simulations (e.g. Tejchman, 1997 [107]; Bauer & Huang, 1999 [11]; Huang & Bauer, 2003 [61]; Bauer & Huang, 2004 [12]) with a micro-polar continuum model show a strong influence of the assumed boundary conditions on the deformation within the shear layer. Tejchman (1997) [107] proposed a constitutive model with a linear relation between the displacement and Cosserat rotation of the soil particle at the interface. Herein, the assumed factor of the particle translation which is transmitted to the rotation shows a strong influence on the deformation of the granular soil close to the interface. The main results obtained from analytical and numerical studies with micro-polar hypoplastic models and a homogeneous distribution of the prescribed interface boundary conditions are:

- the displacement field is nonlinear from the beginning of shearing (e.g. Tejchman & Wu, 1993 [116]; Tejchman, 1994 [106]; Tejchman, 1997 [108]; Tejchman & Bauer, 1996 [111], 2004 [112], 2005 [113]; Bauer et al., 2006 [13]),
- for an initially dense material shear strain localization appears before the peak stress ratio is reached (e.g. Bauer & Huang, 1997 [10]),
- for large shearing the deformation is localized within a narrow zone while outside this localized zone the granular soil behaves rigidly for continuous shearing (e.g. Tejchman & Gudehus, 2001 [114]; Huang & Bauer, 2003 [61]; Gudehus & Nübel, 2004 [56]),
- Cosserat rotations are only pronounced within the localized zone (e.g. Tejchman, 1997 [108], [107]; Tejchman, 2000 [109]),
- the thickness of the localized zone can be detected from the distribution of the Cosserat rotation, the void ratio, the gradients of the curvatures and the shear strain rate, based on their pronounced values (e.g. Tejchman & Gudehus, 2001 [114]; Huang et al., 2002 [63]; Nübel, 2002 [89]; Huang & Bauer, 2003 [61]; Nübel & Huang, 2004 [90]),
- while the distribution of the void ratio reflects the history of dilatancy or contractancy, the distribution of the shear strain rate is related to the current active thickness of the localized zone (e.g. Huang & Bauer, 2003 [61]; Bauer et al., 2006 [13]),

- the thickness of the localized zone is almost proportional to the mean grain size and also influenced by the void ratio, the pressure level and the micro-polar boundary conditions (e.g. Tejchman, 1997 [107]; Tejchman et al., 1999 [115]),
- for monotonic shearing the state quantities within localized zones tend towards a stationary state for which a coupling between the norm of the deviatoric stress and the norm of the couple stress tensor may exist depending on the type of the micro-polar model (e.g. Huang, 2000 [60]; Nübel, 2002 [89]; Huang & Bauer, 2003 [61]).

In particular, for shearing of a granular layer between parallel walls with symmetric micro-polar boundary conditions at the top and the bottom surfaces the shear localization occurs in the middle of the layer. When non-symmetric micro-polar boundary conditions are considered the localization is closer to the surface boundary with higher prescribed Cosserat rotation. In the following section further numerical studies with different interface properties and different initial states are carried out.

3.1 Shear localization close to a bounding structure

Plane shearing of an infinite extended granular strip in contact with a rough surface of a bounding structure is simulated using the finite element method and a micro-polar hypoplastic model. The bounding structure is assumed to be rigid and it moves parallel to the granular strip. Due to the symmetry of the problem, only a small section of the infinite layer is considered as shown in Fig. 3.3(a). In particular, a section with an initial height of $h_0 = 4$ cm and a width of $b = 10$ cm is discretized with finite elements with a size of 1.25 mm $\times$ 1.25 mm. The finite element mesh and the boundary conditions are shown in Fig. 3.3(b). In order to model the behavior of a lateral infinite layer constraints to the side nodes of the elements along section I and section II are introduced (e.g. Bauer & Huang, 1999 [11]). In particular, each node on the left boundary ($x_1 = 0$) is controlled to have the same displacements and Cosserat rotation as the corresponding node with the same vertical co-ordinate on the right boundary ($x_2 = b$):

$$x_1 = 0 \;:\; u_1(0,x_2) = u_1(b,x_2),\, u_2(0,x_2) = u_2(b,x_2),\, \omega_3^c(0,x_2) = \omega_3^c(b,x_2),$$
$$x_1 = b \;:\; u_1(b,x_2) = u_1(0,x_2),\, u_2(b,x_2) = u_2(0,x_2),\, \omega_3^c(b,x_2) = \omega_3^c(0,x_2).$$

These prescribed lateral constraints also imply that arbitrary field quantities Φ are independent of the coordinate in the direction of shearing, i.e. $\partial\Phi(x_1,x_2)/\partial x_1 = 0$.

For the top surface of the granular soil layers the following boundary conditions are assumed:

$$x_2 = h \;:\; u_1 = 0,\, \sigma_{22} = -p_0 = -100 \text{ kPa},\, \omega_3^c = 0.$$

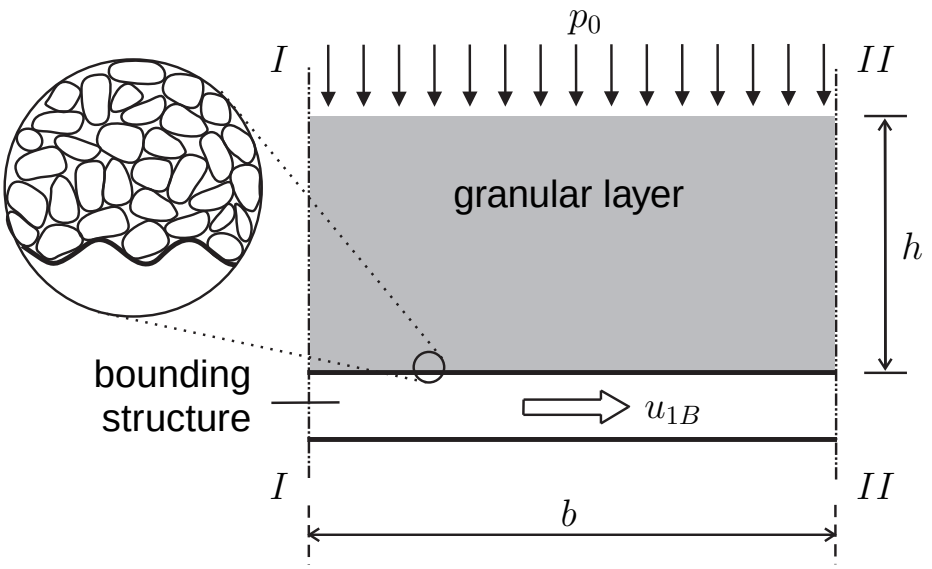

(**a**)

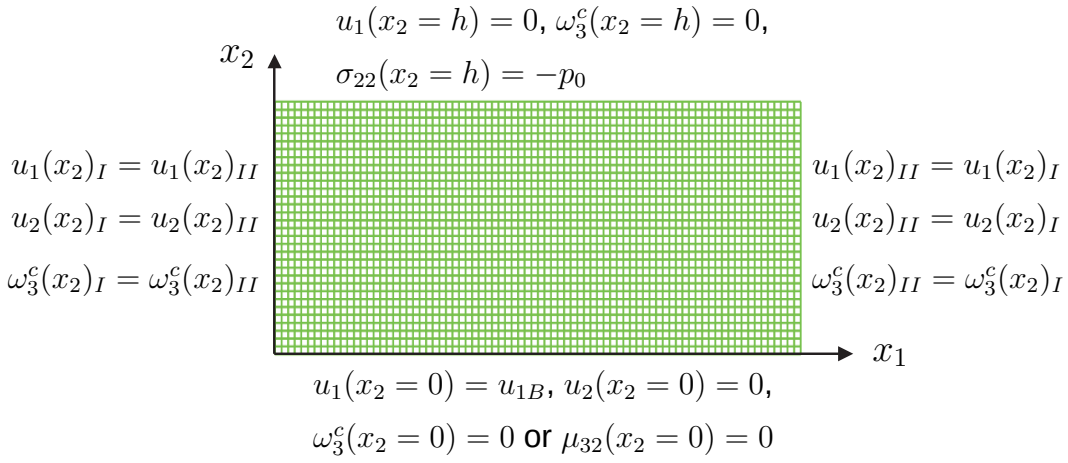

(**b**)

Figure 3.3: Modeling the interaction between a plane infinite granular layer under constant vertical pressure p_0 and the rough surface of the bounding structure under shearing:
(a) section of the granular layer with the height h and the width b,
(b) initially undeformed finite element mesh with prescribed boundary conditions.

Herein the vertical pressure p_0 at the top surface is kept constant. Thus, the height of the specimen can change as a result of contractancy or dilatancy within the specimen. The Cosserat rotation of the soil particle at the top boundary is assumed to be zero.

At the bottom surface of the granular soil layer it is assumed that the grains are captured by the rough surface of the rigid bounding structure so that at the boundary $x_2 = 0$ neither relative displacement nor strain takes place. Therefore, the displacements of the particles along the interface are equal to the prescribed horizontal shear displacement u_{1B} of the bounding structure. In order to study the influence of particle rotation at the interface two different micro-polar boundary conditions are considered: a homogeneous distribution and a periodic fluctuation of the Cosserat rotation. A periodic fluctuation of the Cosserat rotation may be motivated for instance by a different rotation resistance of particles along the interface of a geogrid with a periodic cell structure as sketched out in Fig. 3.2. It can be imagined that the rotation resistance for particles in contact with the smooth surface of the grid members is smaller than the rotation resistance of particles located within the cells of the grid.

The prescribed boundary conditions at the bottom surface of the granular soil for the homogeneous distribution of the Cosserat rotation reads:

$$x_2 = 0 \;\; : \;\; u_1 = u_{1B},\, u_2 = 0,\, \mu_{32}(x_1 \in b) = 0,$$

and for the periodic fluctuation of the Cosserat rotation:

$$x_2 = 0 \;\; : \;\; u_1 = u_{1B},\, u_2 = 0,\, \omega_3^c(x_1 \in b_1) = 0 \text{ and } \mu_{32}(x_1 \in b_2) = 0,$$

with $b_1 + b_2 = b$. In addition to the influence of the Cosserat rotation, the influences of the initial density of the granular body and the mean grain size on the evolutions of the shear deformation and the shear resistance at the interface are also investigated.

The material properties of the granular material used here is the same as those mentioned in Section 2.3.

3.2 Homogeneous distribution of the micro-polar boundary condition

For the case that the rotation resistance along the interface can be neglected the couple stresses are assumed to be zero along the interface, i.e. $\mu_{32}(x_2 = 0) = 0$. In Fig. 3.4 the deformed granular soil strip together with the contour plot of the void ratio is shown after a horizontal displacement of the bounding structure of $u_{1B}/h_0 = 1.4$. It can be seen that the distribution of the displacement across the height of the layer is non-linear. The deformation localizes within a zone close to the surface of the bounding structure. The lighter strip indicates a higher void

Figure 3.4: Deformed shape of the granular body and contour plot of the void ratio within a granular layer after a horizontal displacement of the bounding structure of $u_{1B} = 1.4\,h_0$ (homogeneous initial void ratio $e_0 = 0.6$, mean grain diameter $d_{50} = 1$ mm and zero interface couple stresses) - lightest strip: $e \simeq e_c = 0.76$, darkest strip: $e \simeq e_0 = 0.6$.

ratio which reflects a strong dilatancy within the localized zone. The granular soil outside the shear band remains almost unaffected. Thus, the initially homogeneous distributed void ratio becomes inhomogeneous with stratified structure as a result of strain localization. The predicted thickness of the shear band is about $7 \times d_{50}$, which is smaller than the shear band thickness observed in a granular body far from a bounding structure. For instance, in the biaxial compression test a shear band thickness of $10 \times d_{50}$ up to $20 \times d_{50}$ is reported from the experiments by Hettler & Vardoulakis (1984) [59], Oda et al. (2004) [93] and from the numerical simulations by Tejchman & Bauer (1996) [111], Tejchman (1997) [108], Gudehus & Nübel (2004) [56], Nübel & Huang (2004) [90].

3.2.1 Effect of the initial void ratio and the mean grain size

In order to investigate the influence of the initial void ratio e_0 and the mean grain diameter d_{50} calculations with the following four combinations are performed:

e_0	0.6	0.6	0.55	0.72
d_{50}	0.5	1.0	0.5	0.5

A comparison of the normalized horizontal displacements across the height of the layer is shown in Fig. 3.5(a). It is obvious that the thickness of the localized zone is larger for a higher initial void ratio and a larger mean grain diameter. The Cosserat rotation ω_3^c is extremal at the interface, where the amount is larger for a lower initial void ratio e_0 and a lower mean grain diameter d_{50} as shown in Fig. 3.5(b). At the beginning of shearing the normalized quantity $\varphi_m = \arctan(\sigma_{12}/\sigma_{22})$, which is called mobilized friction angle, increases and reaches a peak state which is higher for an initially denser material (Fig. 3.6). It can be observed that for the same initial void ratio $e_0 = 0.6$ the peak value is not influenced by the mean grain diameter.

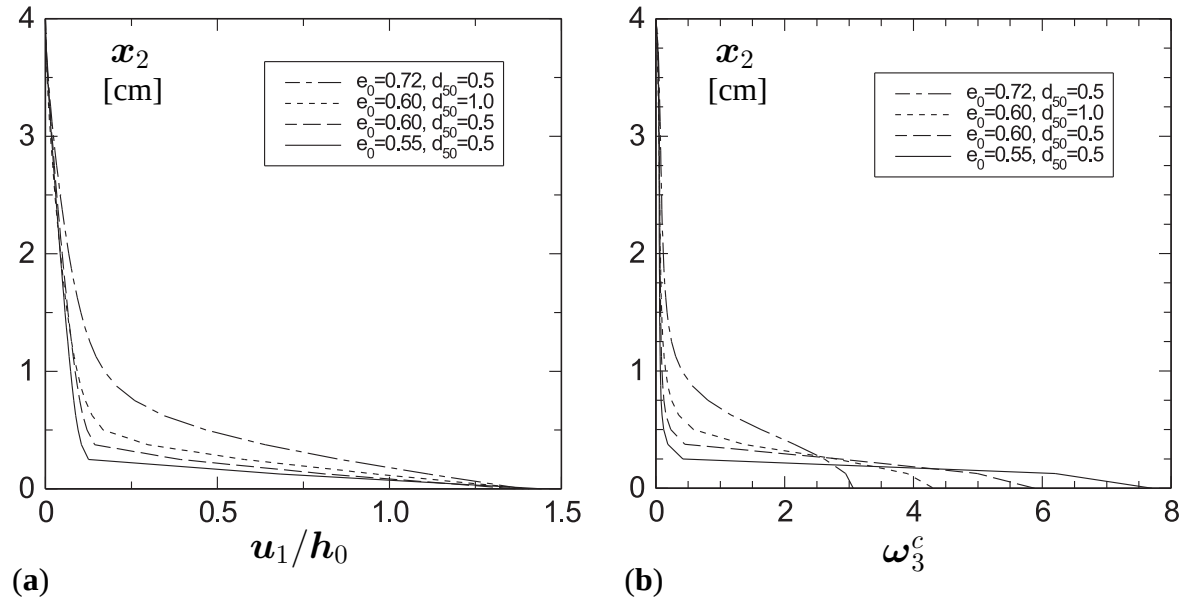

Figure 3.5: Influence of the initial void ratio e_0 and the mean grain diameter d_{50} on the distribution of **(a)** the normalized horizontal displacement u_1/h_0 **(b)** of the Cosserat rotation ω_3^c.

After the peak the mobilized friction angle φ_m decreases and for large shearing it tends towards a stationary value which is close to the critical friction angle of the granular soil. The deviation of the stationary value from the critical friction angle is related to the amount of the shear deformation and may also be affected by the special version of the polar hypoplastic model as discussed in Appendix B. It is worth mentioning that σ_{12} and σ_{22} are stress components parallel and perpendicular to the rough rigid bounding structure. From the equilibrium in the vertical direction it follows that σ_{12} and σ_{22} are independent on the co-ordinate x_2.

3.2.2 Effect of the vertical pressure

The influence of the vertical pressure, i.e. $p_0 = 100$, 200 and 400 kPa, on the deformation behavior of the granular body is shown in Figs. 3.7 - 3.8 for the initially homogeneous specimen with $e_0 = 0.6$ and $d_{50} = 1$ mm and the horizontal displacement of the bounding structure of $u_{1B}/h_0 = 1.4$. In particular, the amount of ω_3^c at the interface is higher for a lower vertical pressure (Figs. 3.7(b)). It can also be observed that the higher the vertical pressure p_0 the larger the thickness of the shear band (Figs. 3.7(a)-(b)). Fig. 3.8(a) clearly shows that a higher vertical pressure p_0 leads to a higher horizontal shear stress σ_{12}. However, under large shearing the mobilized friction angle φ_m tends to a stationary value which is independent of the vertical pressure p_0 (Figs. 3.8(b)). This stationary value is close to the critical friction angle of the granular soil. The reason of the deviation is related to the amount of the shear deformation and may also be affected by the special version of the polar hypoplastic model (Appendix B). It can

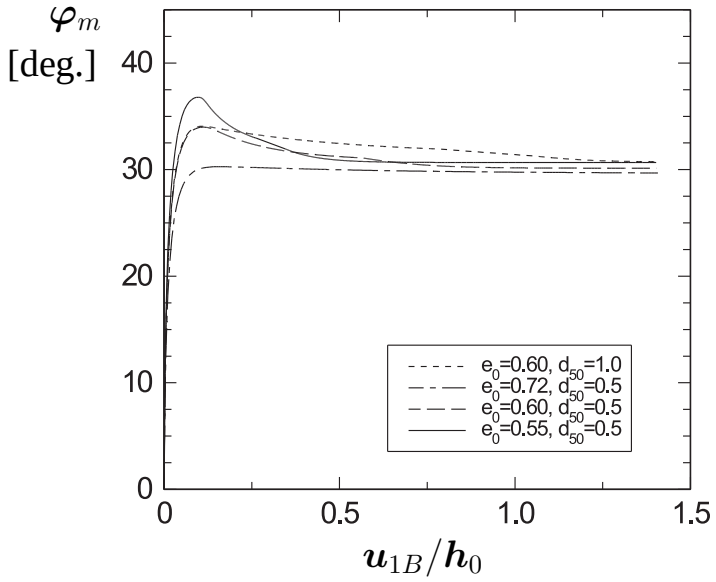

Figure 3.6: Influence of the initial void ratio e_0 and the mean grain diameter d_{50} on the evolution of the mobilized friction angle φ_m .

also be observed from Fig. 3.8(b) that a lower vertical pressure p_0 leads to higher peak value of the mobilized friction angle φ_m .

3.3 Periodic fluctuation of the micro-polar boundary condition

In this section the shear resistances due to a fluctuation of the micro-polar boundary conditions at the interface is investigated. Two special cases with a periodic change of the Cosserat rotation or the couple stress within prescribed distances are considered. The fluctuation is modeled by a bit-by-bit locking of Cosserat rotation ω_3^c along the boundary $x_2 = 0$ as follows:

- Small bit-by-bit locking:
  Zero Cosserat rotation, i.e. $\omega_3^c = 0$, is prescribed within a distance of 5 mm followed by zero couple stress, i.e. $\mu_{32} = 0$, within a distance of 20 mm (Fig. 3.9(a)).

- Large bit-by-bit locking:
  Zero Cosserat rotation, i.e. $\omega_3^c = 0$, is prescribed within a distance of 12.5 mm followed by zero couple stress, i.e. $\mu_{32} = 0$, within a distance of 12.5 mm (Fig. 3.9(b)).

The numerical calculations are carried out for an initial void ratio of $e_0 = 0.6$, a mean grain diameter of $d_{50} = 1$ mm and a constant vertical pressure of $p_0 = 100$ kPa. For a prescribed horizontal displacement of the bounding structure of $u_{1B} = 2\,h_0$ the numerical results obtained

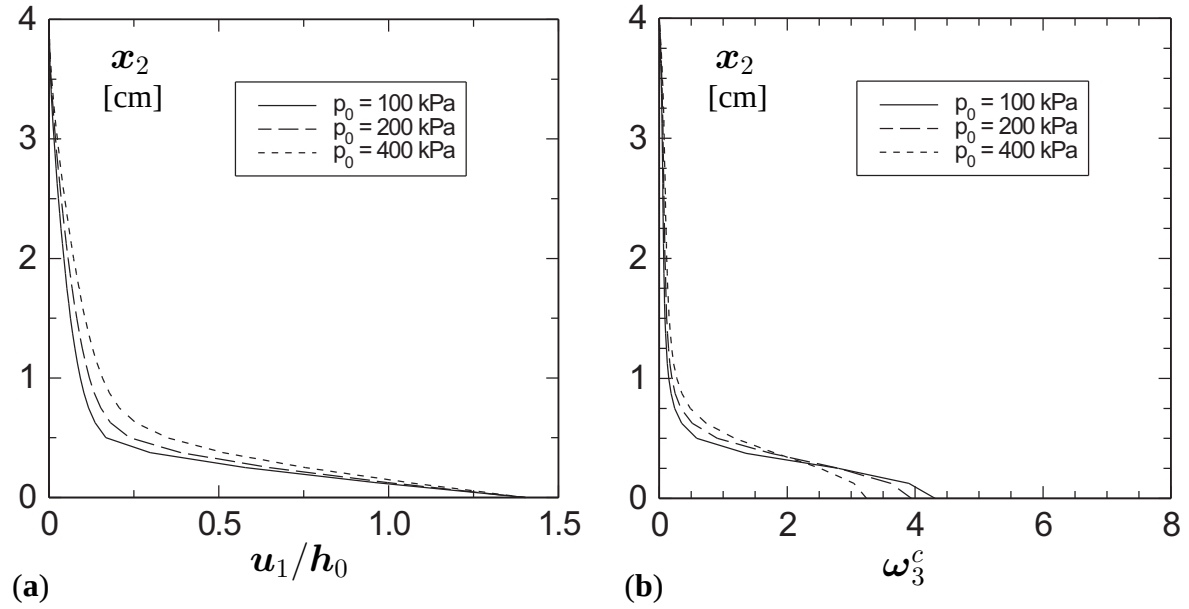

Figure 3.7: Influence of the vertical pressure p_0 on the distribution of (**a**) the normalized horizontal displacement u_1/h_0 and (**b**) the Cosserat rotation ω_3^c.

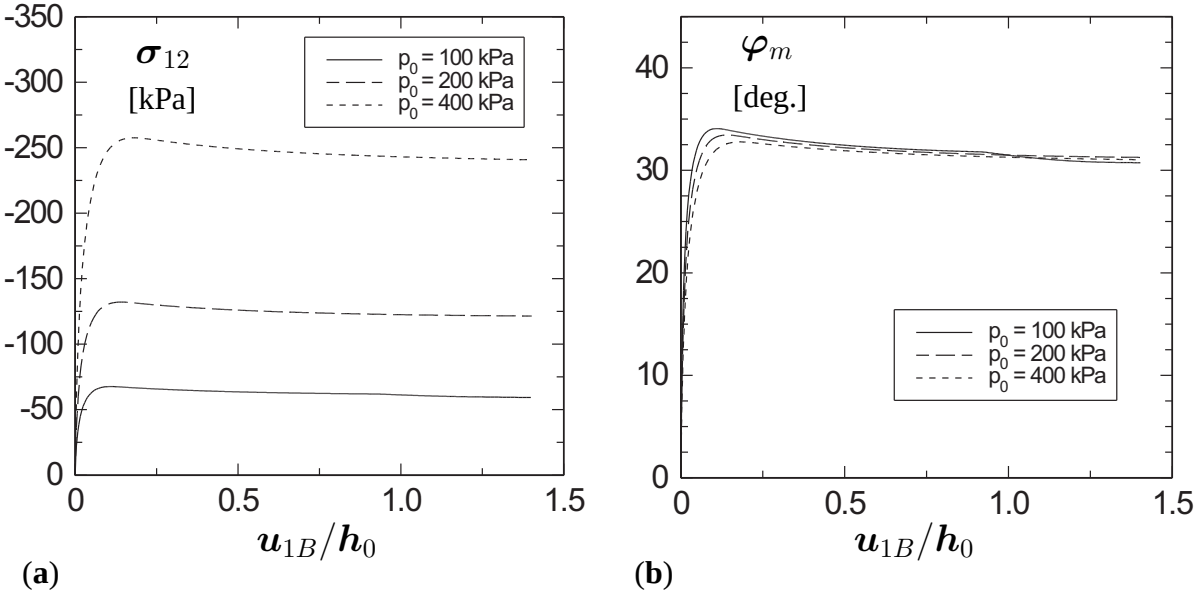

Figure 3.8: Influence of the vertical pressure p_0 on the evolution of (**a**) the mean horizontal shear stress σ_{12} and (**b**) the mobilized friction angle φ_m .

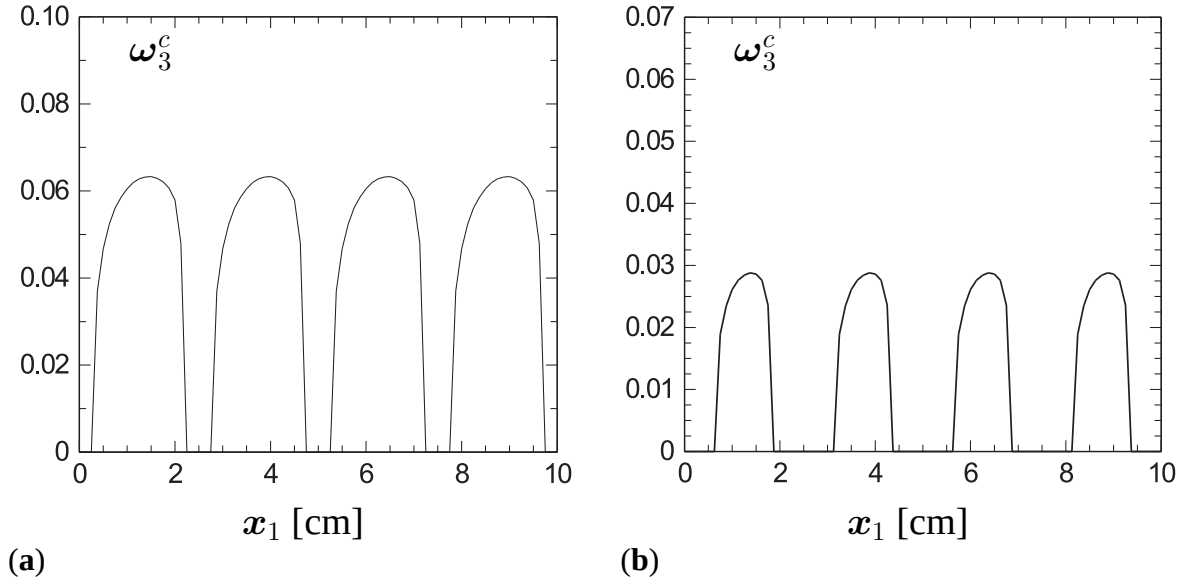

Figure 3.9: Fluctuation of the Cosserat rotation ω_3^c along the interface: (**a**) small bit-by-bit locking of the Cosserat rotation, (**b**) large bit-by-bit locking of the Cosserat rotation.

for the small bit-by-bit locking of the Cosserat rotation are shown in Figs. 3.9(a) - 3.12(a) while those for the large bit-by-bit locking of the Cosserat rotation are shown in Figs. 3.9(b) - 3.12(b).

In particular, Figs. 3.9(a) and 3.9(b) show the distribution of assumed-values of the Cosserat rotation ω_3^c along an interface section of 10 cm. The deformed shapes of the granular body as well as the contour plots of the void ratio e are shown for the small and for the large bit-by-bit locking of the Cosserat rotation in Figs. 3.10(a) and 3.10(b), respectively. A comparison indicates that the location and the thickness of the shear band strongly depend on the micro-polar boundary conditions at the interface. It can be seen in Fig. 3.10 that the location of the shear band is at the bottom in the middle of the granular layer for both cases. In particular, compared to the large bit-by-bit locking of the Cosserat rotation the location of the shear band is closer to the surface of the bounding structure for the small one. The thickness of the shear band is $10 \times d_{50}$ for both cases. The lighter strip shows strong dilatancy in the localized zone while the material outside of the shear band remains almost unaffected. For the corresponding stress state a critical void ratio of $e_c = 0.76$ can be calculated via Eq. 2.41. Figs. 3.11(a) and 3.11(b) show the distribution of the Cosserat rotation across the height of specimen for the small and the large bit-by-bit locking of the Cosserat rotation, respectively. Figs. 3.12(a) and 3.12(b) show that a fluctuation of the rotation resistance leads to a fluctuation of the mobilized friction angle φ_m. However, under large shearing the average value of the mobilized friction angle φ_m is independent of the assumed fluctuation of the micro-polar boundary conditions and it is almost equal to the critical friction angle of the granular soil for plane shearing. The small deviation is again related to the amount of the applied shear deformation and may also be influenced by the specific polar hypoplastic version (Appendix B).

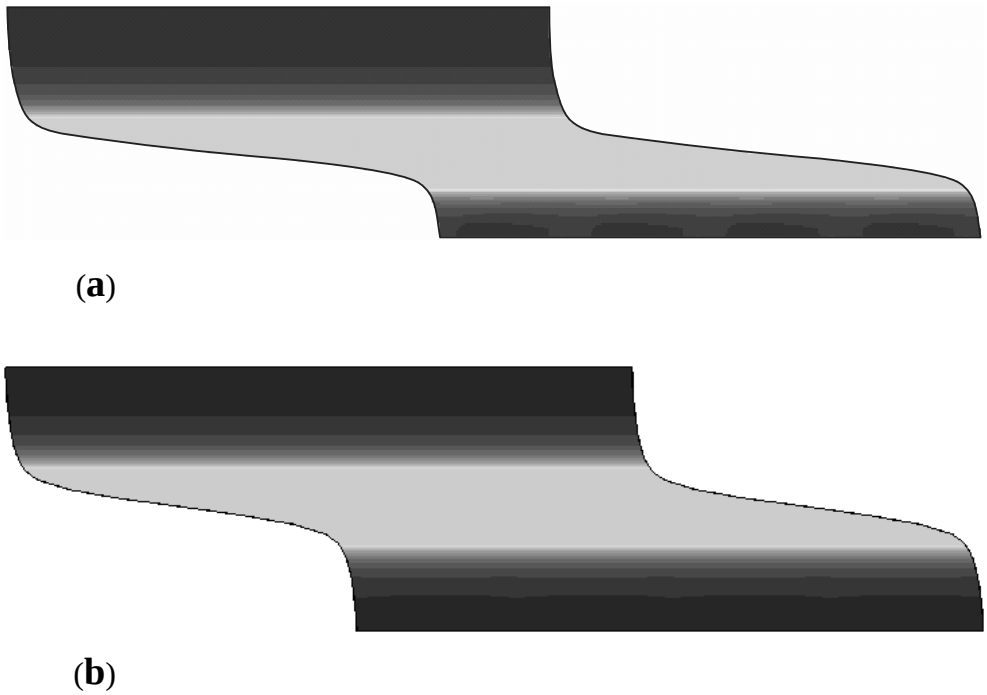

(**a**)

(**b**)

Figure 3.10: Deformed shape of the granular body and contour plot of a granular layer after a horizontal displacement of $U_{1B} = 2h_0$ with (**a**) Small bit-by-bit locking of the Cosserat rotation, (**b**) Large bit-by-bit locking of the Cosserat rotation (homogeneous initial void ratio $e_0 = 0.6$, mean grain diameter $d_{50} = 1mm$) - lightest strip: $e \simeq e_c = 0.76$.

3.4 Effect of a stratified soil

While in the foregoing investigations the granular specimen with a homogeneous distributed initial void ratio is investigated the influence of a thin layer with a slightly different initial void ratio is considered in this section. In particular, an initially rather high void ratio of $e_0 = 0.62$ within the layer $0.375 \leq x_2 \leq 0.5$ cm is assumed. Along the bottom surface of the granular soil a small bit-by-bit locking of the Cosserat rotation is prescribed.

The resulting displacement field and Cosserat rotation across the specimen's height are compared to that obtained for a homogeneous initial void ratio of $e_0 = 0.6$ after $u_{1B} = 2h_0$, as shown in Fig. 3.13. In particular, the location of shear localization shifts closer to the layer with the initially higher void ratio, as shown by the dashed curve in Fig. 3.13(a). The same tendency can be observed for the distribution of the Cosserat rotation (Fig. 3.13(b)).

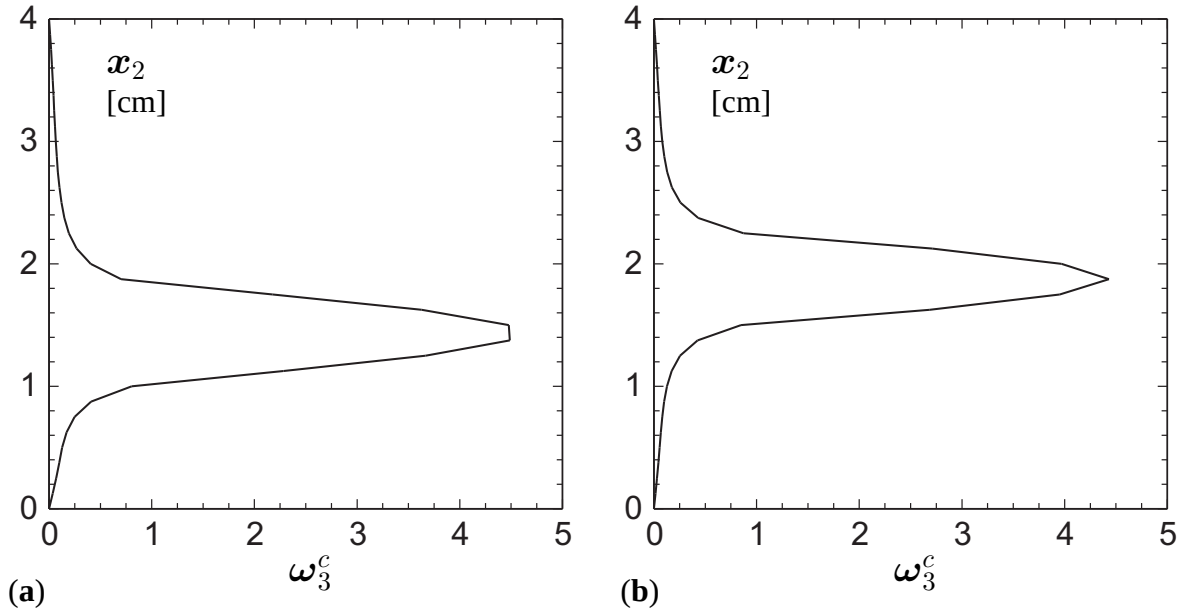

Figure 3.11: Distribution of the Cosserat rotation ω_3^c across the height of the granular layer with: (**a**) small and (**b**) large bit-by-bit locking of the Cosserat rotation along the interface after a horizontal displacement of the bounding structure $u_{1B} = 2h_0$.

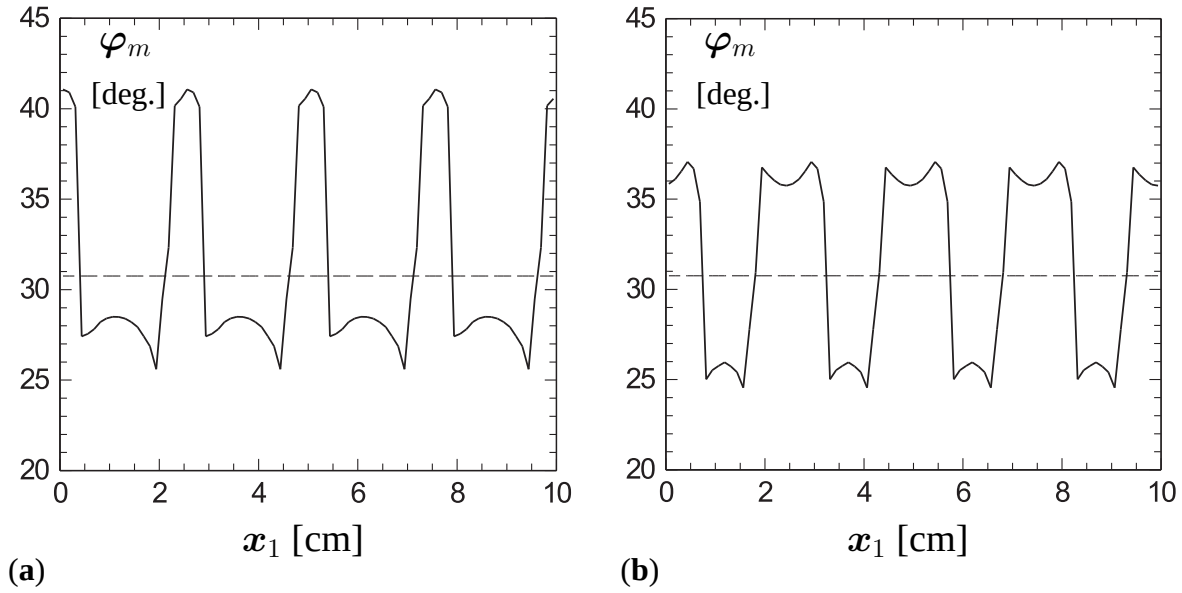

Figure 3.12: Fluctuation of the mobilized friction angle φ_m (solid curve) and its average value (dotted line) for a granular layer with: (**a**) small and (**b**) large bit-by-bit locking of the Cosserat rotation along the interface after a horizontal displacement of the bounding structure $u_{1B} = 2h_0$.

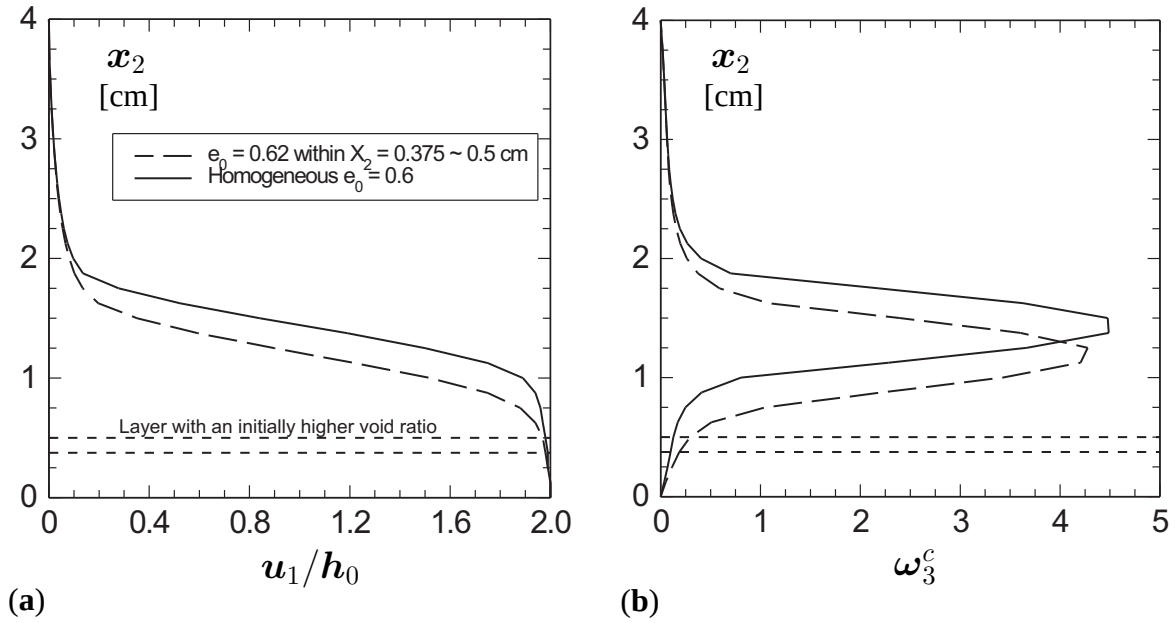

Figure 3.13: Influence of the distribution of the initial void ratio e_0 for a mean grain diameter $d_{50} = 1$ mm, and a fluctuation of the micro-polar interface boundary conditions:
(**a**) normalized horizontal displacement u_1/h_0,
(**b**) Cosserat rotation ω_3^c across the height of the layer.

3.5 Comparison of the numerical results

From the numerical results obtained for the particular prescribed micro-polar boundary conditions along the interface:

- zero couple stress (Case 1),
- small bit-by-bit locking of Cosserat rotation (Case 2),
- large bit-by-bit locking of Cosserat rotation (Case 3),

the following main conclusions can be drawn:

The location of the shear band is:

- for Case 1: close to the interface,
- for Case 2: farther from the interface,
- for Case 3: close to the middle of the granular layer.

The predicted thickness of the shear band is:

- for Case 1: $7 \times d_{50}$,
- for Case 2: $10 \times d_{50}$,
- for Case 3: $10 \times d_{50}$.

Furthermore, the shear band is located closer to a layer with slightly higher initial void ratio when a stratified soil is considered.

4 MECHANICAL BEHAVIOR OF A SOILBAG UNDER VERTICAL COMPRESSION

In this chapter, the mechanical behavior of a single soilbag under vertical compression is investigated using analytical and numerical approaches. For the analytical approach, several simplifications are assumed. In particular, it is assumed that from the beginning of compression the stress ratio in the soil material is constant and the volume of the soil does not change during deformation. Depending on the assumed shape of the section, the stress in the granular material inside the soilbag is assumed to be either piecewise or entirely homogeneous distributed. For the soilbag structure a plane strain condition and a frictionless interface behavior between the soil and the bag are considered. Thereby, the tensile stress of the bag is uniformly distributed along the circumference of the soilbag. In addition to the analytical model by Matsuoka & Liu (2006) (in the following called M&L) where a rectangular section is assumed, also a soilbag model with lateral semicircular boundaries is investigated. In contrast to the model by M&L the local equilibrium in the soilbag is generally fulfilled with the proposed soilbag model.

In order to validate the assumptions made for the analytical model the corresponding numerical investigations using the finite element method are also conducted. Particular attention is paid on the shear localization depending on the vertical displacement, the assumed interface properties and the initially homogeneous or heterogeneous distribution of the void ratio. As already discussed in Chapter 3, the interface behavior is dictated by the slide and the rotation resistances of soil particles in contact with the wrapping bag. The following interface properties are investigated: a frictionless interface (no slide and rotation resistance) and a fully interlocked interface (translation and rotation of the soil particles at the interface coincides with the motion of the bag).

4.1 Analytical approach

4.1.1 Soilbag model by Matsuoka - Liu

The mechanical behavior of a single soilbag under monotonic vertical compression (Fig. 4.1) is investigated based on a simplified analytical model proposed by M&L (2006). In this model the following assumptions are made:

- The soilbag with a rectangular cross section, i.e. with the width B and the height H,

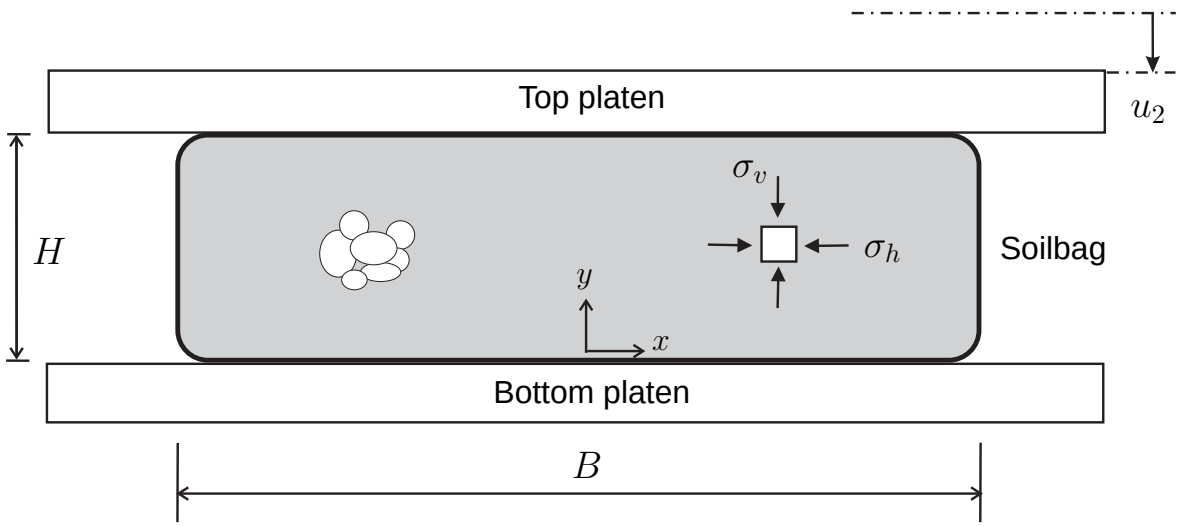

Figure 4.1: Section of a vertically compressed single soilbag.

is completely filled with a cohesionless granular material and vertically compressed between parallel rigid platens. In the M&L model, a constant horizontal pressure is prescribed at the lateral plane boundaries of the soilbag which is not taken into account in the present study. In this context, it can be noted that a constant lateral pressure does not guarantee that the lateral boundaries remain plane during compression. Thus, an alternative shape of the soilbag section with lateral semicircular boundaries is discussed in Subsection 4.1.2.

- The weight of the granular material inside the bag is neglected. Thus, for the initially uncompressed soilbag a stress free state is assumed for both, the wrapping bag and the granular materials.
- Plane strain condition (with the unity depth l perpendicular to the plane) is considered.
- The surfaces of the top and bottom platens are frictionless and the normal pressure p_v in the contact zone is homogeneously distributed over the contact area B x l.
- The material behavior of the wrapping bag is linear elastic-ideally plastic, where the used elastic modulus E and the limit tensile stress σ_{limit} is defined for a tensile test under plane strain condition. The change of the thickness of the membrane of the bag is neglected.
- The interface between the granular material and the bag is frictionless. As relative displacements between the granular material and the bag are not restricted, the tensile stress in the membrane is uniformly mobilized. Although a rectangular section is considered, the edges are smoothed out as shown in Fig. 4.1.
- The vertical stress σ_v and horizontal stress σ_h of the granular material is homogeneously distributed. Independent of the amount of the compression the stress ratio σ_v/σ_h is as-

sumed to be constant and equal to the limit stress ratio of the granular material. Thus, the limit stress ratio can be related to the critical friction angle of the granular material. In this context, it is worth noting that during vertical compression the soilbag system is not in the so-called critical state. Although the volume change is assumed to be zero and the limit stress ratio is reached, the magnitude of the stress components in the soil can still increase.

In the following, it will also be assumed that the soilbag has almost a rectangular section with initial dimension of ($B_0 \times H_0$) so that the initial quantities can be approximated as

$$\begin{aligned} \text{initial perimeter} &: L_0 = 2(B_0 + H_0), \\ \text{initial volume} &: V_0 = B_0\, H_0\, l. \end{aligned} \tag{4.1}$$

For a vertical compression u_2 the initial height H_0 of the soilbag reduces to:

$$H = H_0 - u_2. \tag{4.2}$$

As the volume of the soilbag is assumed to be constant during compression, thus

$$V = B\, H\, l = V_0 = B_0\, H_0\, l. \tag{4.3}$$

With respect to Eq. 4.2 and Eq. 4.3 one obtains the width B depending on the initial dimensions and the vertical displacement u_2 as

$$B = \frac{H_0 B_0}{H_0 - u_2}. \tag{4.4}$$

Then the current perimeter $L = 2(B + H)$ can be represented as a function of u_2, i.e.

$$L = 2\left(H_0 - u_2 + \frac{B_0\, H_0}{H_0 - u_2}\right), \tag{4.5}$$

and the change of perimeter $\Delta L = L - L_0$ is defined as

$$\Delta L = \frac{2\, u_2\, (B_0 - H_0 + u_2)}{H_0 - u_2}. \tag{4.6}$$

The normalized quantity, $\Delta L / L_0$, reads:

$$\frac{\Delta L}{L_0} = \frac{u_2\, (B_0 - H_0 + u_2)}{(H_0 - u_2)\, (B_0 + H_0)}, \tag{4.7}$$

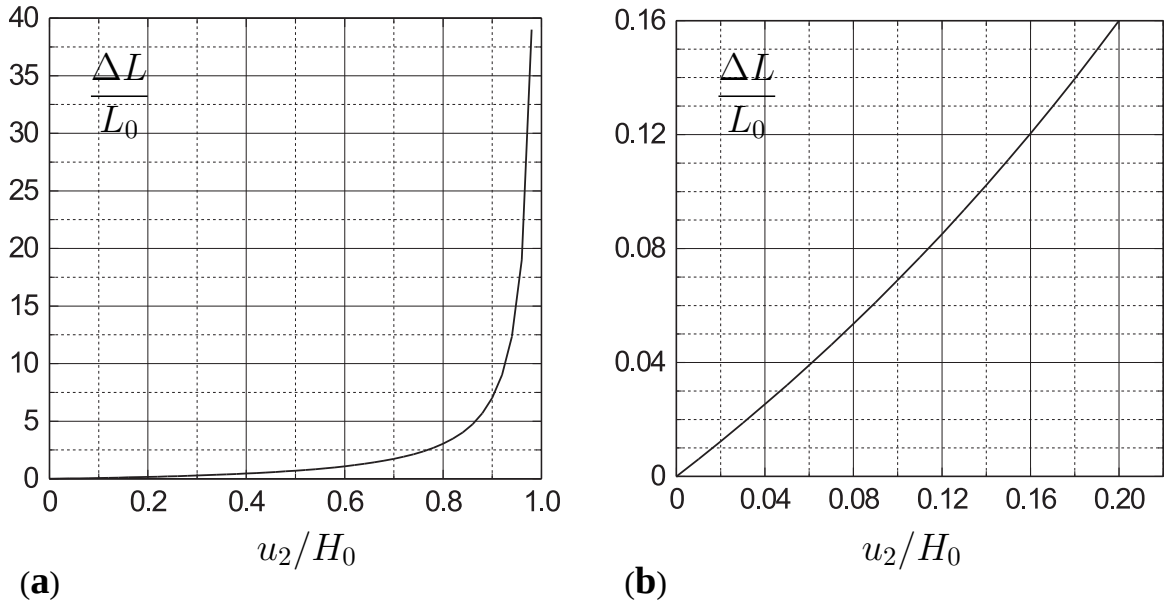

Figure 4.2: Relation between the normalized change of perimeter of the soilbag and the normalized prescribed vertical displacement for (**a**) a higher range of u_2, (**b**) a lower range of u_2.

with the following extreme values:

$$\frac{\Delta L}{L_0} \rightarrow \infty \quad \text{for } u_2 \rightarrow H_0$$

$$\frac{\Delta L}{L_0} = 0 \qquad \text{for the initial state with } u_2 = 0 \text{ and for } \bar{u}_2 = H_0 - B_0 > 0.$$

The latter only has physical meaning for vertically oriented soilbags with the initial dimension $H_0 > B_0$. In this case the change of perimeter is negative at the beginning of vertical compression, i.e. $\Delta L < 0$ for $u_2 < \bar{u}_2$ so that no tensile stress is activated in the wrapping material. In the following only soilbags with the initial dimension $B_0 \geq H_0$ are considered. As an example for $B_0/H_0 = 4$, the nonlinear increase of the normalized quantity $\Delta L/L_0$ with the normalized prescribed vertical displacement u_2/H_0 is shown in Fig. 4.2. From Fig. 4.2(b) it can be observed that $\Delta L/L_0$ is also nonlinear for the small compression range.

With the assumption that the influence of the transverse contraction for plane strain condition is taken into account with the value of the elastic modulus and with respect to the definition of

engineering strain, the tensile stress σ_{bag} and the consequently tensile force T of the bag read

$$\sigma_{bag} = E\frac{\Delta L}{L_0}, \qquad T = E\frac{\Delta L}{L_0} t\, l, \tag{4.8}$$

where E and t are elastic modulus and the thickness of the bag, respectively. It should be noted that the elastic modulus E in Eq. 4.8 already takes into account the influence of the transverse contraction for plane strain condition. With respect to the definition of engineering strain and the real elasticity modulus E_{real}, the relation between E and E_{real} can be obtained as:

$$E = \frac{E_{real}}{1-\nu^2}, \tag{4.9}$$

where ν denotes the Poisson's ratio. When the limit stress σ_{bag}^{limit} in the wrapping material is reached the corresponding quantities $(\Delta L/L_0)_{flow}$ and T_{limit} are:

$$\left(\frac{\Delta L_0}{L_0}\right)_{flow} = \frac{\sigma_{bag}^{limit}}{E}, \qquad T_{limit} = \sigma_{bag}^{limit}\, t\, l. \tag{4.10}$$

Substituting Eq.4.10 into Eq. 4.7,

$$\left(\frac{\Delta L}{L_0}\right)_{flow} = \frac{\sigma_{bag}^{limit}}{E} = \frac{\left(\frac{u_2}{H_0}\right)_{flow}\left(\frac{B_0}{H_0} - 1 + \left(\frac{u_2}{H_0}\right)_{flow}\right)}{\left(1+\frac{B_0}{H_0}\right)\left(1-\left(\frac{u_2}{H_0}\right)_{flow}\right)} \tag{4.11}$$

leads to a quadratic equation for the normalized vertical displacement $(u_2/H_0)_{flow}$. Eq. 4.11 has the following real and only positive solution:

$$\begin{aligned}\left(\frac{u_2}{H_0}\right)_{flow} &= \frac{1}{2}\left[1 - \frac{B_0}{H_0} - \left(1+\frac{B_0}{H_0}\right)\frac{\sigma_{bag}^{limit}}{E}\right] + \\ &+ \frac{1}{2}\left[\sqrt{\left(1-\frac{B_0}{H_0}\right)^2 + \left(1+\frac{B_0}{H_0}\right)^2\left(2+\frac{\sigma_{bag}^{limit}}{E}\right)\frac{\sigma_{bag}^{limit}}{E}}\right].\end{aligned} \tag{4.12}$$

Then, the corresponding dimension of the soilbag reads:

$$\begin{aligned}H_{flow} &= H_0 - u_{2\,flow}, \\ B_{flow} &= \frac{H_0 B_0}{H_0 - u_{2\,flow}}.\end{aligned} \tag{4.13}$$

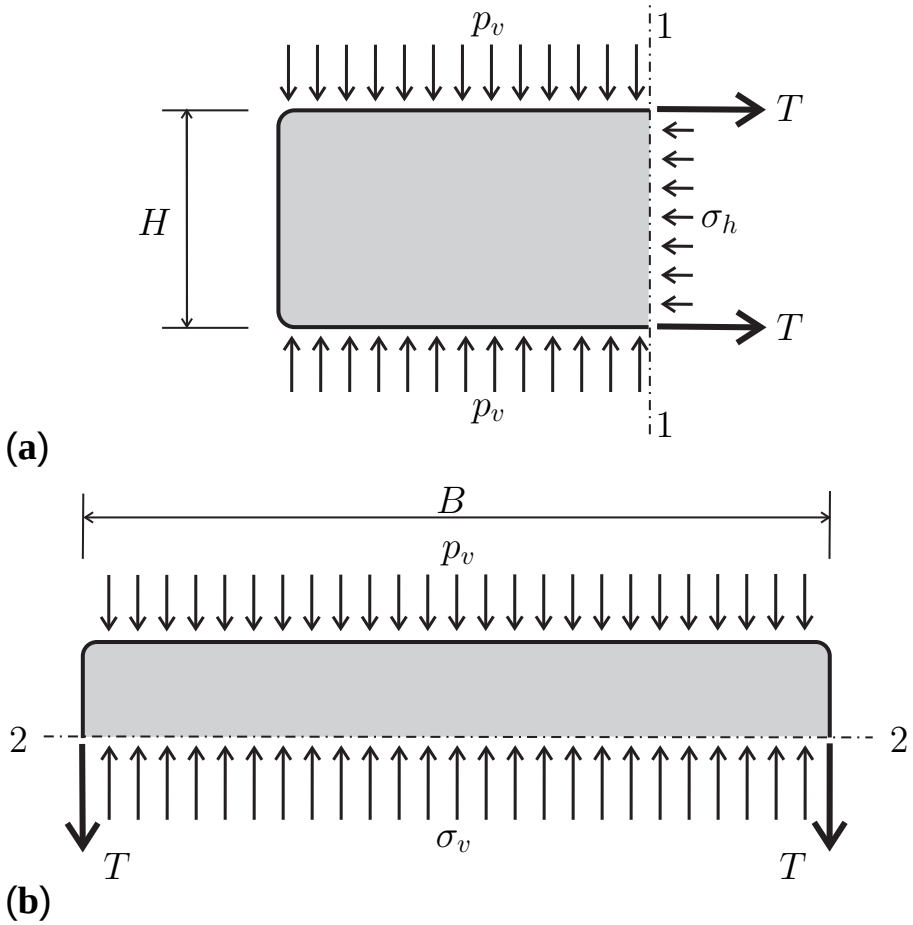

Figure 4.3: Free-body diagram of (**a**) the left part of the soilbag 'cut' at cross section 1-1, (**b**) the upper part of soilbag 'cut' at cross section 2-2; B is the current width and H is the current height of the soilbag; p_v is the applied vertical pressure; T is the tensile force of the bag; σ_h and σ_v are the horizontal and vertical stresses of the granular material, respectively.

In order to analyze the stress state developed in the soilbag, the free-body diagrams of a soilbag with the unity depth l perpendicular to the plane in Fig. 4.3 are considered. With respect to Fig. 4.3(a) the equilibrium for the horizontal forces requires:

$$\sigma_h \, H \, l - 2T = 0. \tag{4.14}$$

With respect to Fig. 4.3(b) the equilibrium for the vertical forces reads:

$$\sigma_v \, B \, l - p_v \, B \, l - 2T = 0. \tag{4.15}$$

From Eq. 4.14 and Eq. 4.15 the horizontal stress σ_h and the vertical stress σ_v of granular material inside the soilbag can be represented as

$$\sigma_h = \frac{2T}{H\,l}, \qquad \sigma_v = p_v + \frac{2T}{B\,l}. \tag{4.16}$$

With the tensile force of the bag $T = \sigma_{bag}\,t\,l$ Eq. 4.16 can be re-written:

$$\sigma_h = \frac{2t}{H}\,\sigma_{bag}, \qquad \sigma_v = p_v + \frac{2t}{B}\,\sigma_{bag}. \tag{4.17}$$

As long as the wrapping material is in an elastic state and with respect of Eq. 4.7 and Eq. 4.8 one obtains for σ_h and σ_v:

$$\sigma_h = 2E\,t\,\frac{u_2\,(B_0 - H_0 + u_2)}{(B_0 + H_0)\,(H_0 - u_2)^2}, \tag{4.18}$$

$$\sigma_v = p_v + 2E\,t\,\frac{u_2\,(B_0 - H_0 + u_2)}{B_0\,H_0\,(B_0 + H_0)}. \tag{4.19}$$

From Eq. 4.19 it can be concluded that for the analytical model by M&L (2006) the local equilibrium close to the top and bottom is not fulfilled because the vertical stress σ_v in the soil material is not equal to the vertical compression pressure p_v.

In the relations 4.18 and 4.19 the only unknown is the vertical pressure p_v acting on the contact surface. Thus, an additional constitutive relation is needed which has to be related to the material property of the filling material. To this end, it is convenient to consider in the following the stress ratio K, i.e.

$$K = \frac{\sigma_v}{\sigma_h}.$$

It can be noted that for an incompressible (the Poisson's ratio $\nu \rightarrow 0.5$) and linear elastic material the stress ratio K is independent of the elastic modulus:

$$K = \frac{\sigma_v}{\sigma_h} = \frac{\nu\varepsilon_h + (1-\nu)\varepsilon_v}{\nu\varepsilon_v + (1-\nu)\varepsilon_h} = 1.$$

Moreover, with $K = 1$ the stress ratio of an isotropic stress state is represented. In general, however, the stress ratio K is not constant and it strongly depends on the loading history because the material behavior of granular material is non-linear and inelastic. Only for special boundary conditions, simplified material properties and special states, an analytical relation for K can be derived. For example, under monotonic oedometric compression, i.e. one dimensional compression under zero lateral strain, the stress ratio is almost constant and it can be

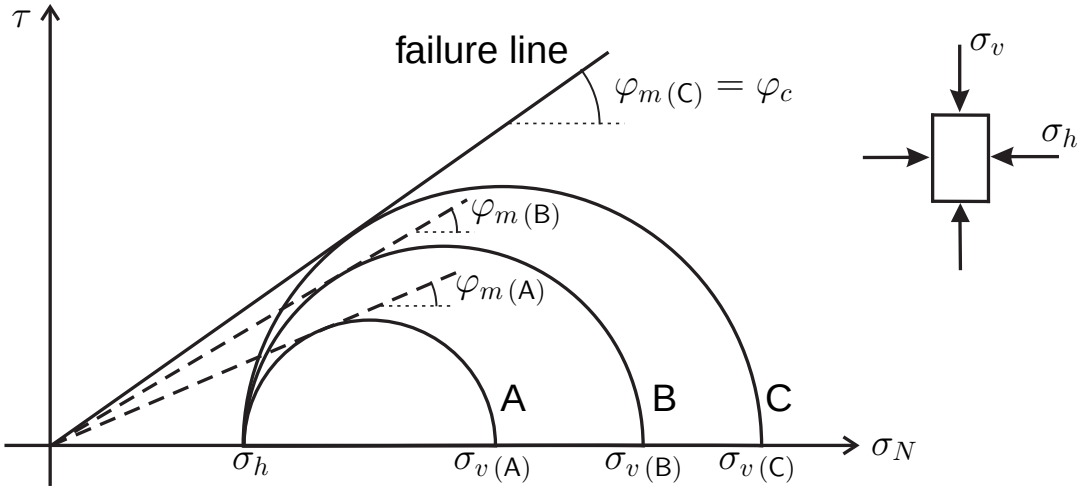

Figure 4.4: Different stress states in the Mohr-Coulomb diagram for triaxial compression under an axisymmetric lateral stress $\sigma_h < \sigma_v$.

approximated using Jaky's formula: $1/K = 1 - \sin\varphi$, where φ is the friction angle of the cohesionless granular material. As $\sin\varphi < 1$, the horizontal stress σ_h is lower than the vertical stress σ_v under oedometric compression. Another element test is the triaxial compression of a granular material under a lateral constant axisymmetric stress. In the Mohr diagram an increase of the vertical stress σ_v can be demonstrated with an increase of the diameter of the Mohr circle from circle A to B to C as illustrated in Fig. 4.4. By using the tangent to the circle passing the origin of the diagram the stress ratio can be expressed as a function of the so-called mobilized friction angle φ_m as:

$$K = \frac{1 + \sin\varphi_m}{1 - \sin\varphi_m}, \tag{4.20}$$

where $\sin\varphi_m$ is the ratio between the radius of the Mohr circle, which is formed by the major stress σ_v and minor stress σ_h, and the abscissa of the center of the corresponding Mohr circle, i.e.

$$\sin\varphi_m = \frac{(\sigma_v - \sigma_h)/2}{(\sigma_v + \sigma_h)/2} = \frac{K-1}{K+1}.$$

The increase of the mobilized friction angle φ_m is limited by the so-called failure state (Mohr circle C in Fig. 4.4). In the case that the failure state coincides with the critical stress state the corresponding mobilized friction angle is called critical friction angle φ_c. For such states the stress ratio K can be expressed as a function of φ_c:

$$K = \frac{1 + \sin\varphi_c}{1 - \sin\varphi_c}. \tag{4.21}$$

It is worth mentioning that in the homogeneous triaxial compression test there is no intermediate principle stress, the vertical stress and horizontal stress are the major principle stress and the minor principle stress, respectively. For more general stress states, when the intermediate principle stress is not the same as the minor principle stress there exists three different Mohr circles. In the present model the assumption is made that the stress ratio is related to the critical friction angle as defined in Eq. 4.21. According to Eq. 4.21, lower values of K are related to lower critical friction angles φ_c as demonstrated in the following table

K	1	2	3	4	5
φ_c (degree)	0.00	19.50	30.00	36.87	41.81

With the definition of the stress ratio $K = \sigma_v/\sigma_h$ the following relation for the vertical pressure p_v can be deduced from the representation of the vertical and horizontal stresses in Eq. 4.16:

$$p_v = \frac{2T}{B\,l}\left[\frac{B}{H}K - 1\right]. \tag{4.22}$$

As an alternative, Eq. 4.22 can also be represented as a function of the vertical compression u_2:

$$p_v = 2\,E\,t\,\frac{u_2\,(B_0 - H_0 + u_2)}{B_0\,H_0\,(B_0 + H_0)}\left[\frac{B_0\,H_0}{(H_0 - u_2)^2}\left(\frac{1+\sin\varphi_c}{1-\sin\varphi_c}\right) - 1\right]. \tag{4.23}$$

With respect of Eq. 4.22 the resulting vertical force $F_v = p_v\,B\,l$ acting on the soilbag reads:

$$F_v \;=\; p_v\,B\,l \;=\; 2\,T\,\left[\frac{B}{H}K - 1\right]. \tag{4.24}$$

For different stress ratios K the ratio F_v/T linearly increases with the increase of the size ratio B/H of the soilbag (Fig. 4.5(a)). It can be observed that for constant K the ratio F_v/T is higher for the rectangular shape of the soilbag, i.e. $B/H > 1$, than for the square shape of the soilbag, i.e. $B/H = 1$.

In addition, Fig. 4.5(b) shows that for constant size ratio B/H the ratio F_v/T linearly increases with the increase of the stress ratio K.

When the limit stress in the wrapping bag is reached, the corresponding vertical pressure $p_{v\,flow}$ can be calculated as

$$p_{v\,flow} = \frac{2\,\sigma_{bag}^{limit}\,t}{B_{flow}}\left[\frac{B_{flow}}{H_{flow}}K - 1\right], \tag{4.25}$$

and the corresponding vertical compression force $F_{v\,flow}$ reads

$$F_{v\,flow} = p_{v\,flow}\,B_{flow}\,l. \tag{4.26}$$

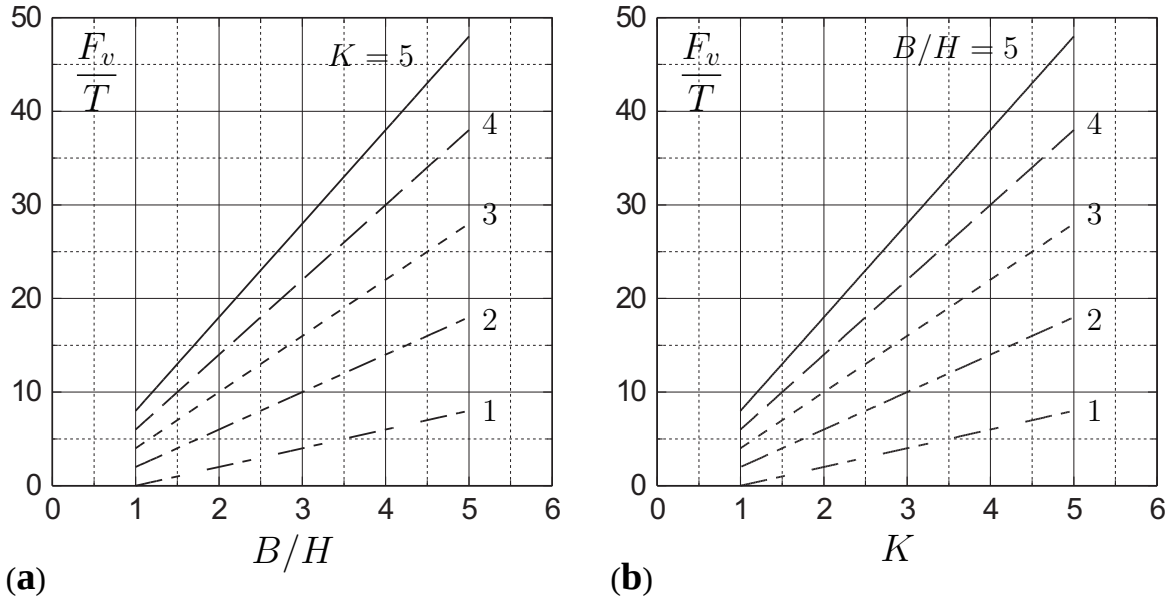

Figure 4.5: Evolution of the normalized compression force F_v/T depending on the: (**a**) stress ratio coefficient K, (**b**) size ratio B/H.

Herein, B_{flow} and H_{flow} are the corresponding dimension of the soilbag according to Eq. 4.13. For continuing loading:

$$\bar{p}_v = \frac{2\,\sigma_{bag}^{limit}\,t}{B}\left[\frac{B}{H}K - 1\right]. \tag{4.27}$$

and

$$\bar{F}_v = \bar{p}_v\,B\,l. \tag{4.28}$$

From Eq. 4.27 and Eq. 4.28, it follows that for continuing compression the resulting reaction force can increase.

For an initial perimeter of $L_0 = 100$ cm, a constant stress ratio of $K = 3$, a limit stress of the wrapping material of $\sigma_{bag}^{limit} = 70$ MPa, a thickness of the wrapping material of $t = 0.3$ mm, an elastic modulus of the wrapping material of $E = 533$ MPa, and for the initial size ratios of $B_0/H_0 = 1$, 3, 4 and 5, the following specific values can be obtained:

$\frac{B_0}{H_0}$	B_0 cm	H_0 cm	$(u_2)_{flow}$ cm	H_{flow} cm	B_{flow} cm	$p_{v\,flow}$ kPa	$F_{v\,flow}$ kN
5	41.7	8.3	1.3	7	49.6	1714	849
4	40	10	1.7	8.3	48.3	1434	692
3	37.5	12.5	2.4	10.1	46.5	1159	538
1	25	25	6.4	18.7	38	565	214

Figs. 4.6(a) - 4.6(d) show the evolution of the normalized change of perimeter, $\Delta L/L_0$, the normalized tensile stress of the bag, $\sigma_{bag}/\sigma_{bag}^{limit}$, the normalized vertical pressure, $p_v/p_{v\,flow}$, and the normalized vertical compressive force, $F_v/F_{v\,flow}$, for different initial size ratios B_0/H_0. It can be seen that for the same normalized vertical displacement u_2/H_0 the increases of $\Delta L/L_0$, $\sigma_{bag}/\sigma_{bag}^{limit}$, $p_v/p_{v\,flow}$ and $F_v/F_{v\,flow}$ are higher for a higher initial size ratio B_0/H_0. While the increase of ΔL with u_2 is unlimited (Fig. 4.6(a)) the increase of the stress σ_{bag} in the wrapping material is limited by σ_{bag}^{limit} (Fig. 4.6(b)). In particular, $\Delta L/L_0$ can still increase even though the limit tensile force in the wrapping material is reached as shown in Fig. 4.7(a). From Fig. 4.6(b) it can be observed that the limit tensile stress in the wrapping material is reached earlier for a higher initial size ratio B_0/H_0. A continuous increase of the vertical displacement u_2 leads to a further increase of the vertical pressure p_v and, consequently, also to a further increase of the resulting vertical force F_v (Figs. 4.6(c) - 4.6(d)). The increase of p_v and F_v, however, is much smaller than in the linear elastic range of the soilbag material. This behavior was also observed in experiments by Lohani et al. (2006) [80].

From relations 4.22 and 4.24 it follows that for $u_2 \rightarrow H_0$ or equivalent for $H \rightarrow 0$ the vertical pressure p_v and the resulting vertical force F_v tend to infinite. However, for real soilbag materials p_v and F_v are restricted either by the maximum flow strain of the wrapping material or the destruction of the wrapping material caused by the penetration of grains with sharp edges, at which the soilbag breaks.

4.1.2 Soilbag model with lateral semicircular boundaries

In this section, the soilbag with lateral semicircular boundaries is considered as sketched out in Fig. 4.8. The same assumption as mentioned in the previous section are considered except for the shape of the lateral soilbag boundaries and the distribution of the stress ratio of the granular material. In particular, in the middle part of the soilbag a stress ratio of $K = 3$, and in the semicircle area a stress ratio of $K = 1$ is assumed. The latter is required for semicircular boundaries and it means that $\sigma_{v2}^* = \sigma_h^*$ in these areas (Fig. 4.9(b)). For the present model the stress σ_{bag}^* in the wrapping material, the stress components σ_v^* and σ_h^* in the soil material and the vertical pressure p_v^* can be derived in a similar manner as shown in the forgoing section. In

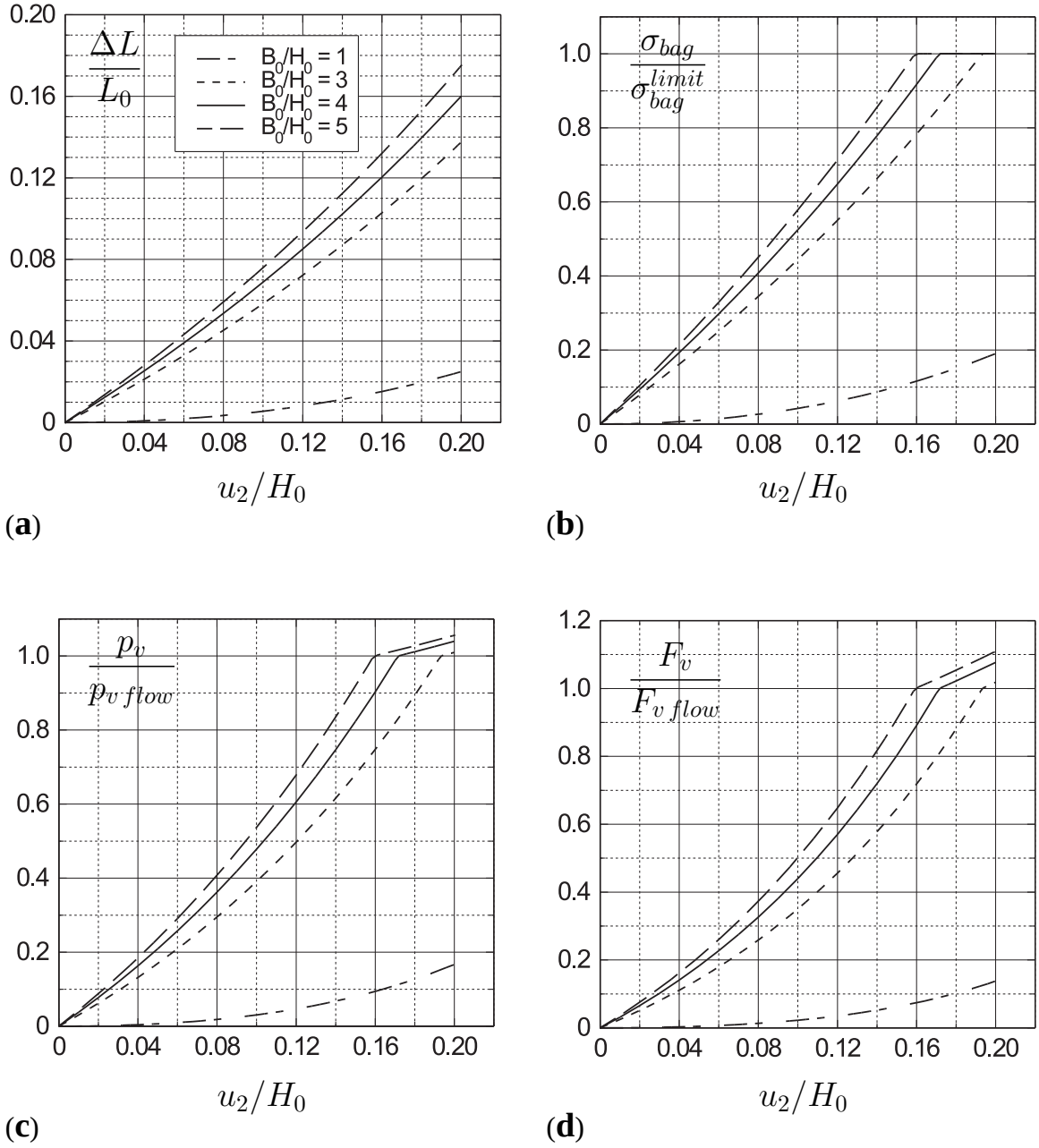

Figure 4.6: Evolution of (**a**) the normalized change of perimeter $\Delta L/L_0$, (**b**) the normalized tensile stress of the bag $\sigma_{bag}/\sigma_{bag}^{limit}$, (**c**) the normalized vertical pressure $p_v/p_{v\,flow}$, (**d**) the normalized vertical force $F_v/F_{v\,flow}$ for different ratios $B_0/H_0 = 1, 3, 4, 5$, $K = 3$, $L_0 = 100$ cm, $t = 0.3$ mm, $\sigma_{bag}^{limit} = 70$ MPa, $E = 533$ MPa.

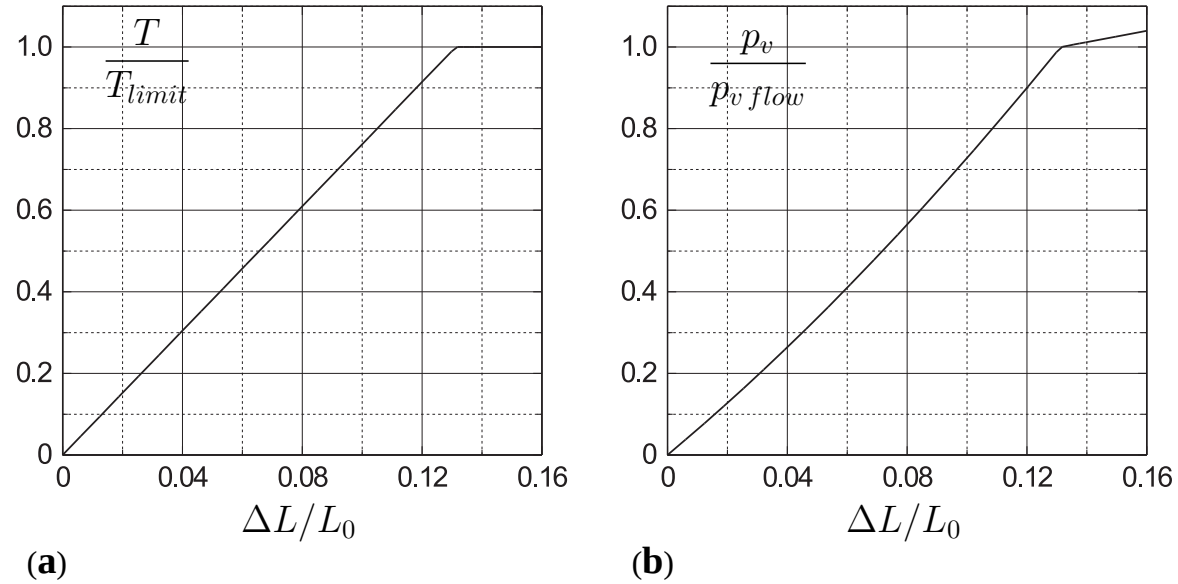

Figure 4.7: Evolution of (**a**) the normalized tensile force T/T_{limit} of the bag, (**b**) the normalized vertical pressure $p_v/p_{v\,flow}$ of the soilbag with regards to the normalized change of perimeter $\Delta L/L_0$ of the soilbag for $u_2/H_0 = 0.2$ and $B_0/H_0 = 4$.

particular, the following relations can be obtained:

$$\begin{aligned} \text{initial perimeter} \;&:\; L_0^* = 2B_0^* + \pi H_0, \\ \text{initial volume} \;&:\; V_0^* = B_0^*\, H_0\, l + \pi \left(\frac{H_0}{2}\right)^2 l. \end{aligned} \tag{4.29}$$

For the vertical displacement u_2, the corresponding quantities read:

$$H = H_0 - u_2, \tag{4.30}$$

$$B^* = \frac{4B_0^* H_0 + 2\pi H_0 u_2 - \pi u_2^2}{4(H_0 - u_2)}, \tag{4.31}$$

$$L^* = \frac{4B_0^* H_0 - 2\pi H_0 u_2 + 2\pi H_0^2 + \pi u_2^2}{2(H_0 - u_2)}, \tag{4.32}$$

$$\Delta L^* = L^* - L_0^* = \frac{u_2(\pi u_2 + 4B_0^*)}{2(H_0 - u_2)}, \tag{4.33}$$

$$\frac{\Delta L^*}{L_0^*} = \frac{u_2(\pi u_2 + 4B_0^*)}{2(H_0 - u_2)(2B_0^* + \pi H_0)}\,. \tag{4.34}$$

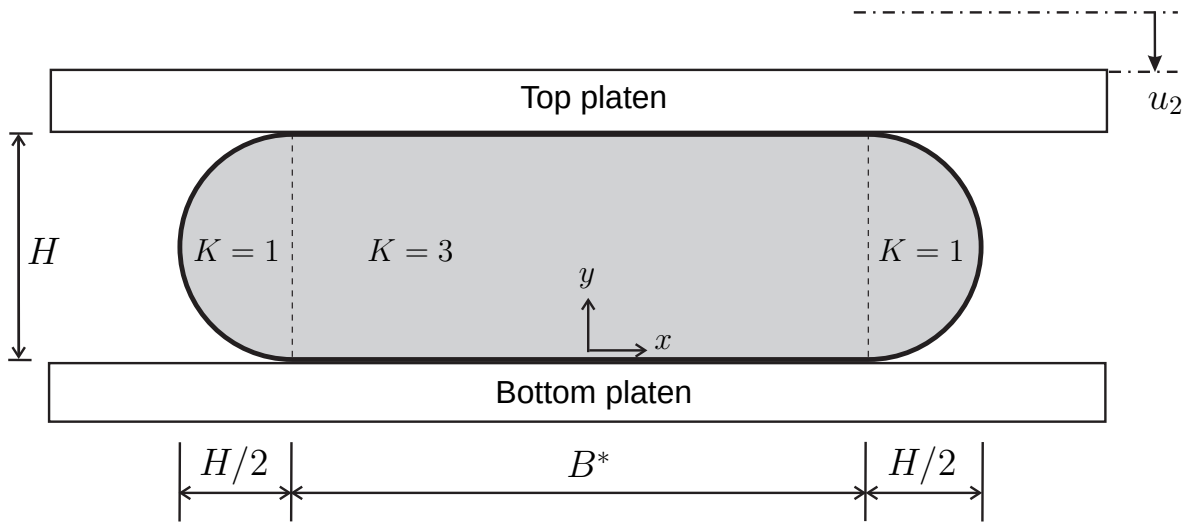

Figure 4.8: Section of a vertically compressed soilbag with semicircular boundaries and different stress ratios K.

The equilibrium of the horizontal forces for the left part of the soilbag (Fig. 4.9(a)) requires:

$$\sigma_h^* \, H \, l \; - \; 2 \, \sigma_{bag}^* \, t \, l \; = \; 0, \tag{4.35}$$

and for the upper part of the soilbag (Fig. 4.9(b)) the equilibrium of the vertical forces reads:

$$p_v^* \, B^* \, l \; - \; \sigma_v^* \, B^* \, l \; - \; 2 \, \sigma_{v2}^* \frac{H}{2} \, l \; + \; 2 \, \sigma_{bag}^* \, t \, l \; = \; 0. \tag{4.36}$$

By substituting Eq. 4.35 into Eq. 4.36 and with respect to $\sigma_{v2}^* = \sigma_h^*$, it follows

$$\sigma_v^* \; = \; p_v^*. \tag{4.37}$$

A comparison of Eq. 4.19 with Eq. 4.37 shows that in contrast to the model by M&L (2006) also the local equilibrium in the vertical direction is fulfilled for the present model, i.e. $\sigma_v^* \; = \; p_v^*$.

For $\sigma_{bag}^* = E(\Delta L^* / L_0^*)$, Eq. 4.35 can be written as:

$$\begin{aligned} \sigma_h^* \; &= \; \frac{2 \, t \, E}{(H_0 - u_2)} \frac{u_2(\pi u_2 + 4B_0^*)}{2(H_0 - u_2)(2B_0^* + \pi H_0)} \\ &= \; \frac{2 \, t \, E \, u_2(\pi u_2 + 4B_0^*)}{(H_0 - u_2)^2(2B_0^* + \pi H_0)}. \end{aligned} \tag{4.38}$$

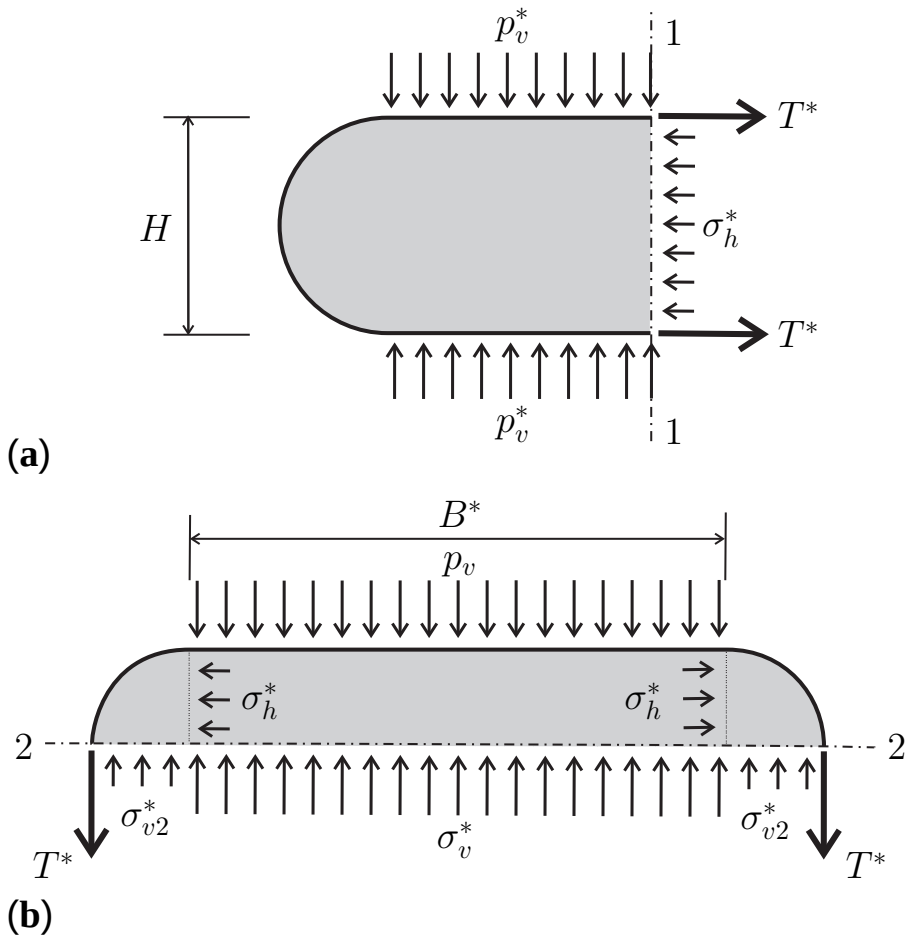

Figure 4.9: Free-body diagram of (**a**) the left part of the soilbag with lateral semicircular boundaries 'cut' at cross section 1-1, (**b**) the upper part of soilbag with lateral semicircular boundaries 'cut' at cross section 2-2.

With respect to the stress ratio $K = \sigma_v^*/\sigma_h^*$, the vertical pressure p_v^* reads:

$$\begin{aligned} p_v^* &= K\,\sigma_h^* \\ &= \left(\frac{1+\sin\varphi_c}{1-\sin\varphi_c}\right)\frac{E\,t\,u_2(\pi u_2 + 4B_0^*)}{(H_0-u_2)^2(2B_0^*+\pi H_0)}. \end{aligned} \tag{4.39}$$

In order to compare the present model with the model proposed by M&L (2006) the following three different initial states are assumed:

A : the initial volume V_0^* is the same as the initial volume V_0 for the M&L model, i.e. $V_0^* = V_0 = B_0 H_0 l$,

B : the initial perimeter L_0^* is the same as the initial perimeter L_0 for the M&L model, i.e. $L_0^* = L_0 = 2(B_0 + H_0)$,

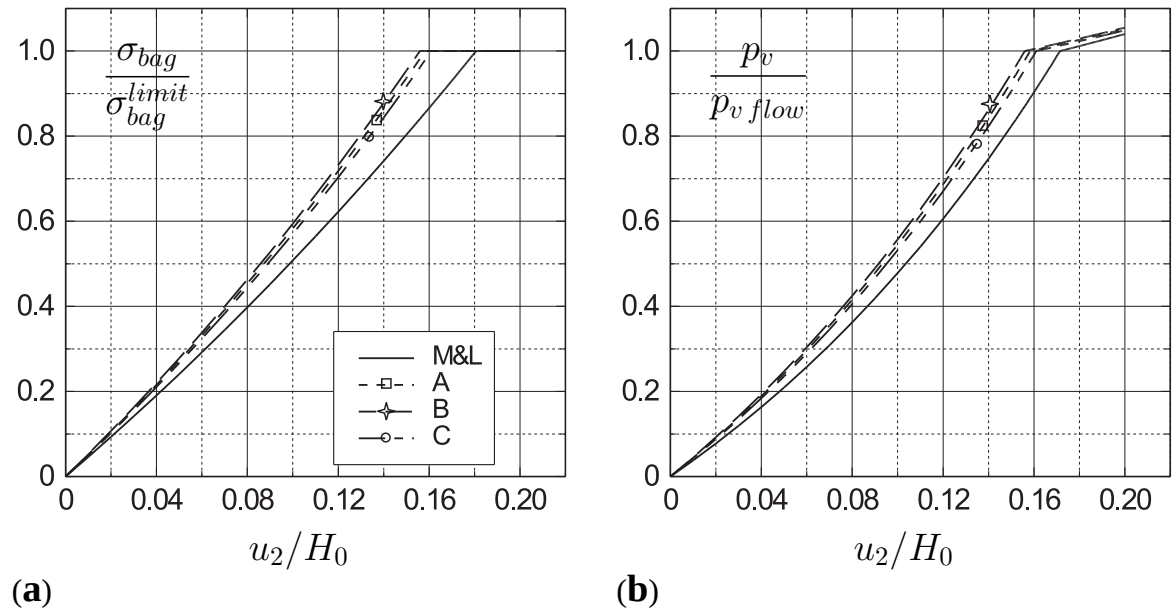

Figure 4.10: Evolution of (**a**) the normalized tensile stress $\sigma_{bag}/\sigma_{bag}^{limit}$ of the bag, (**b**) the normalized vertical pressure $p_v/p_{v\,flow}$ of the soilbag for different analytical models, $B_0/H_0 = 4$, $t = 0.3$ mm, $\sigma_{bag}^{limit} = 70$ MPa, $E = 533$ MPa.

C : the initial total width, i.e. $(B_0^* + H_0)$, is the same as the initial width B_0 for the M&L model, i.e. $B_0^* = B_0 - H_0$.

Figs. 4.10(a) - Fig. 4.10(b) show the evolutions of the normalized stress $\sigma_{bag}/\sigma_{bag}^{limit}$ of the wrapping material and the normalized vertical pressure $p_v/p_{v\,flow}$ for different analytical models. From both figures, it can be seen that for the same vertical compression u_2 the stress in the soilbag and also the vertical pressure is slightly higher for model B than for model A and C. These small differences between models A, B and C are related to the differences in the magnitude of the perimeter L^*. The values of $\sigma_{bag}/\sigma_{bag}^{limit}$ and $p_v/p_{v\,flow}$ obtained from the models A, B and C are significant higher than that from the M&L model. This can be explained by the different assumptions made for the distribution of the stress ratio K.

4.2 Numerical simulations

For the following numerical simulations with the finite element method, it is assumed that the soilbag is completely filled with a cohesionless granular material and compressed between parallel stiff and frictionless platens which are wider than the final deformed width of the soilbag (Fig. 4.11). The vertical compression is applied on the top of the soilbag by the prescribed vertical displacement u_2. For the soilbag structure, a plane strain condition is assumed. The

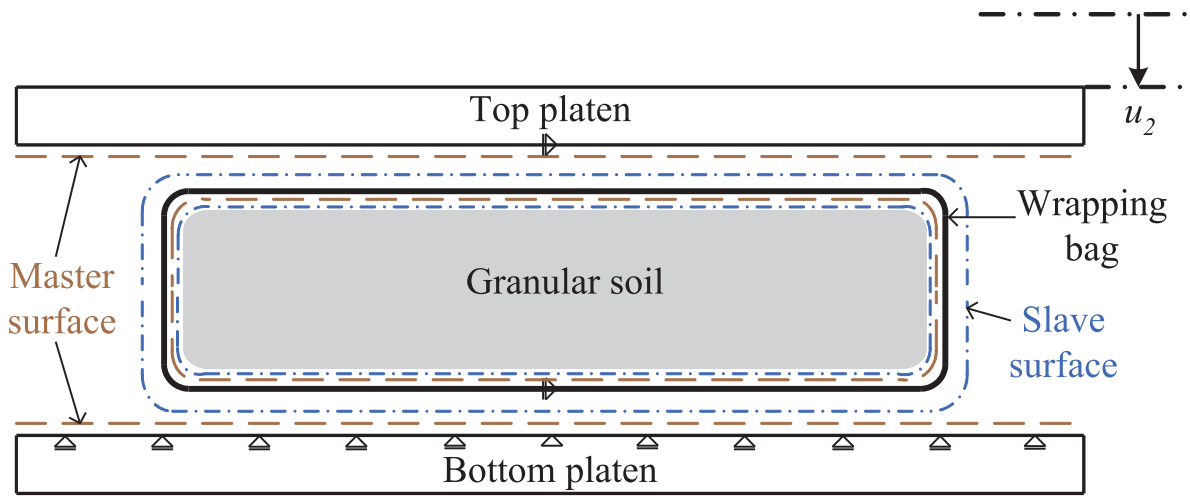

Figure 4.11: Master surfaces and slave surfaces for simulation of the interface.

weight of the soilbag is neglected. Particular attention is paid to the influence of the interface behavior between the granular soil and the bag on the evolution of stress and strain.

The mechanical behavior of the granular material is described with the micro-polar hypoplastic model outlined in Section 2.3. A four nodes quadrilateral iso-parametric element with bilinear shape function and rotational degree of freedom is used for plane strain conditions as proposed by Huang (2000) [60]. The wrapping bag is discretized with linear truss elements and for the mechanical behavior the same elastic-ideally plastic material model is used as for the analytical investigations in Section 4.1. The incapability of the bag to resist compression is taken into account. In contrast to the analytical approach, an updated cross section area of the truss elements is taken into account by assuming an incompressible material.

The contact between the granular material and the bag and the contact between the bag and the top and bottom platens are described with the use of the concept of master surface and slave surface, which allows to model relative displacements as well as a separation or closing of the contact between two bodies. In particular, for the interface between the bag and the top and bottom platens, the master surface is attached to the stiffer elements of the top and the bottom platens while the slave surface is attached to the elements of the bag (Fig. 4.11). The same frictionless interface behavior, i.e. the friction coefficient is zero, is assumed as for the analytical investigation.

For the interface between the bag and the granular material, the master surface is attached to the elements of the wrapping bag while the slave surface is attached to the elements of the granular soil (Fig. 4.11). The following two different interface behaviors between the bag and the granular material are investigated:

1. Frictionless interface: the outer nodes of the bounding finite soil elements and the bag nodes are allowed to have relative displacements and rotations. These properties are

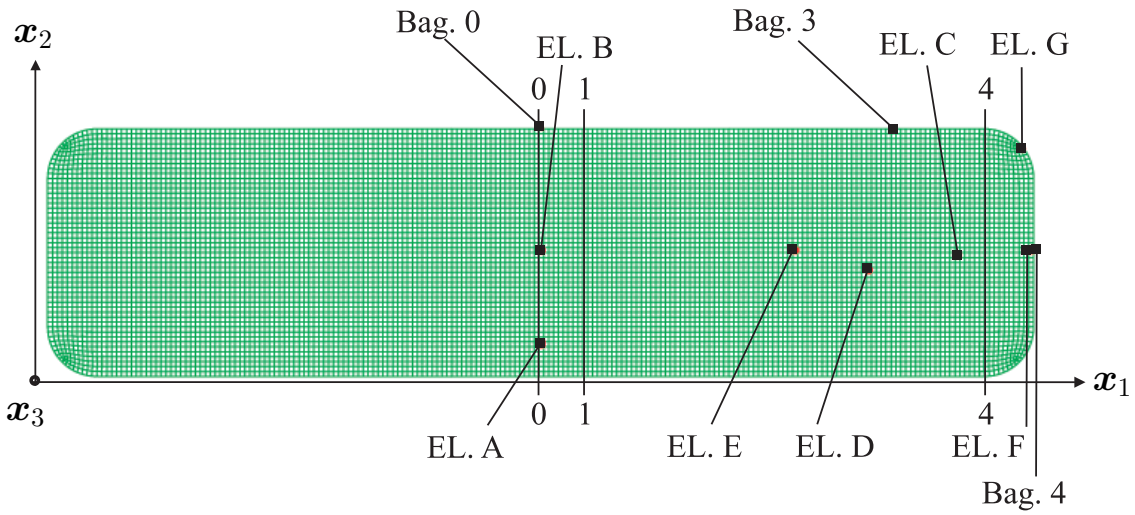

Figure 4.12: Undeformed shape of the soilbag.

achieved with a friction coefficient of zero and zero couple stresses prescribed at the interface.

2. Interlocked interface: the outer nodes of the bounding finite soil elements are connected with the nodes of the bag elements, thus, no relative displacements and Cosserat rotations between soil nodes and bag nodes take place.

In the following, a soilbag with a dimension of $B_0 = 40$ cm and $H_0 = 10$ cm is considered. In contrast to the analytical approach, the perimeter of the soilbag can be computed without any restriction of the shape of the deformed soilbag. In particular, the current perimeter is computed from the summation of the lengths of the individual bag elements. For the undeformed shape (Fig. 4.12), the initial perimeter is $L_0 = 96.6$ cm. The initial size of an element is 0.2 cm $\times$ 0.2 cm with the exception of elements in the area close to the curved boundaries. For the filling material, the constitutive constants for quartz sand as mentioned in Section 2.3 is used with an initial void ratio of $e_0 = 0.60$. The following elastic properties are used for the thin wrapping bag with a thickness of $t = 0.3$ mm (Liu, 2006 [79]):

elastic modulus	E	$=$	533 MPa,
tensile limit stress	σ_{bag}^{limit}	$=$	70 MPa.

As the vertical pressure at the top and bottom surface of the granular soil is not uniformly distributed and the volume change is not homogeneous, their mean values are taken for the representation of the numerical results shown in the following sections.

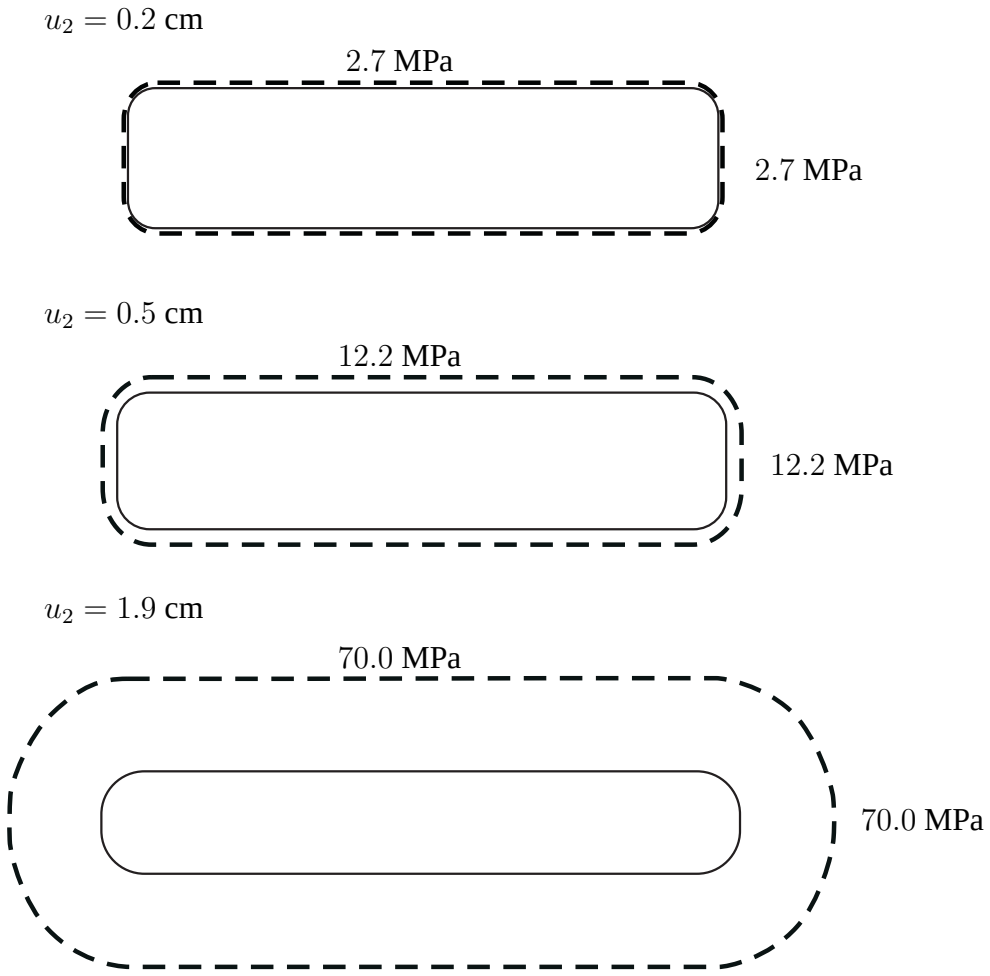

Figure 4.13: Frictionless interface: distribution of tensile stress σ_{bag} in the wrapping material for different vertical displacements u_2.

4.2.1 Frictionless interface behavior

For the frictionless interface the tensile stress in the wrapping bag uniformly increases along the circumference of the soilbag with the increase of the vertical displacement u_2, where the limit stress is reached for $u_2 = 1.9$ cm (Fig. 4.13). Figs. 4.14(a) - 4.14(b) show the evolution of the normalized perimeter of the bag $\Delta L/L_0$ and the tensile stress in the wrapping bag σ_{bag}, respectively. It can be observed that $\Delta L/L_0$ as well as σ_{bag} nonlinearly increases with u_2. The evolution of the mean value of the volume strain is shown in Fig. 4.15(a). After an overall compaction small dilatancy can be observed at $u_2 = 1.0$ cm. However, for $u_2 = 1.9$ cm the soilbag generally experiences compression where $\Delta V < 0.01 \times V_0$. The local volume change, however, significantly varies as discussed in more details later on. A similar small volume change was also reported by Matsuako & Liu (2006) [82] for the unconfined compression test

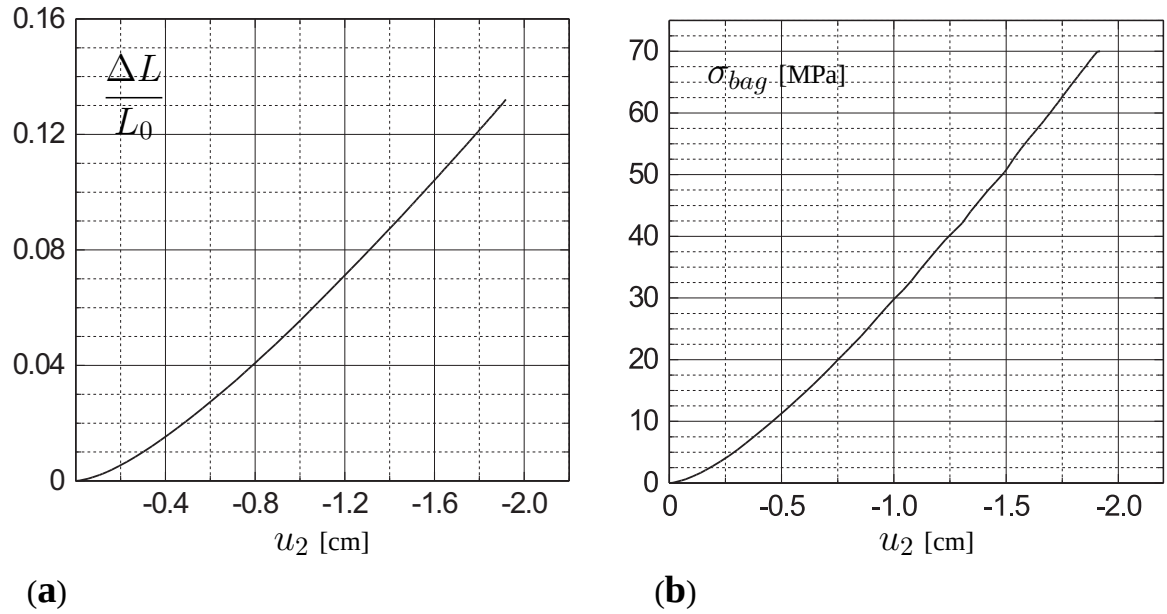

Figure 4.14: Frictionless interface: evolution of the (**a**) normalized change of perimeter $\Delta L/L_0$, (**b**) tensile stress σ_{bag} in the wrapping material.

of soilbags with different granular materials. Fig. 4.15(b) shows the nonlinear increase of the vertical pressure p_v with an increase of the prescribed vertical displacement u_2.

In the following the distribution of the state variables of the granular soil across sections 0-0, 1-1 and 4-4 are shown in Figs. 4.16 - 4.19 for the vertical displacements of $u_2 = 0.2$, 0.5 and 1.9 cm. In particular, Fig. 4.16(a) shows the distribution of the void ratio e at section 0-0 (in the middle of the soilbag), section 1-1 and section 4-4 (at the side of the soilbag). For the small prescribed vertical displacements of $u_2 = 0.2$ cm and $u_2 = 0.5$ cm the distribution of the void ratio e are almost the same across sections 0-0 and 1-1 while a stronger variation can be observed for section 4-4. The maximum void ratio is observed in the middle of section 4-4. When the bag material reaches the limit stress at $u_2 = 1.9$ cm a higher value of the void ratio is also observed in the middle of section 0-0 and at the top of section 1-1. The strong local variation of e indicates strain localization in the zones with a higher e. With an increase of the prescribed vertical displacement the location of the highest value of e shifts from the middle to the bottom in the middle of section 4-4. Thus, the location of shear strain localization changes with continuous compression (Fig. 4.16(c)).

Fig. 4.16(b) shows the distribution of the Cosserat rotation ω_3^c. At the beginning of compression, i.e. for $u_2 = 0.2$ cm and $u_2 = 0.5$ cm, ω_3^c is very small in all sections. For the vertical displacement $u_2 = 1.9$ cm, ω_3^c is pronounced at the middle of section 0-0, at the top part of section 1-1 and at the bottom in the middle of section 4-4. The location of the extremal values of ω_3^c is similar as that for the extremal values of the void ratio (Fig. 4.16(a)) and the deviatoric strain rate (Fig. 4.16(c)).

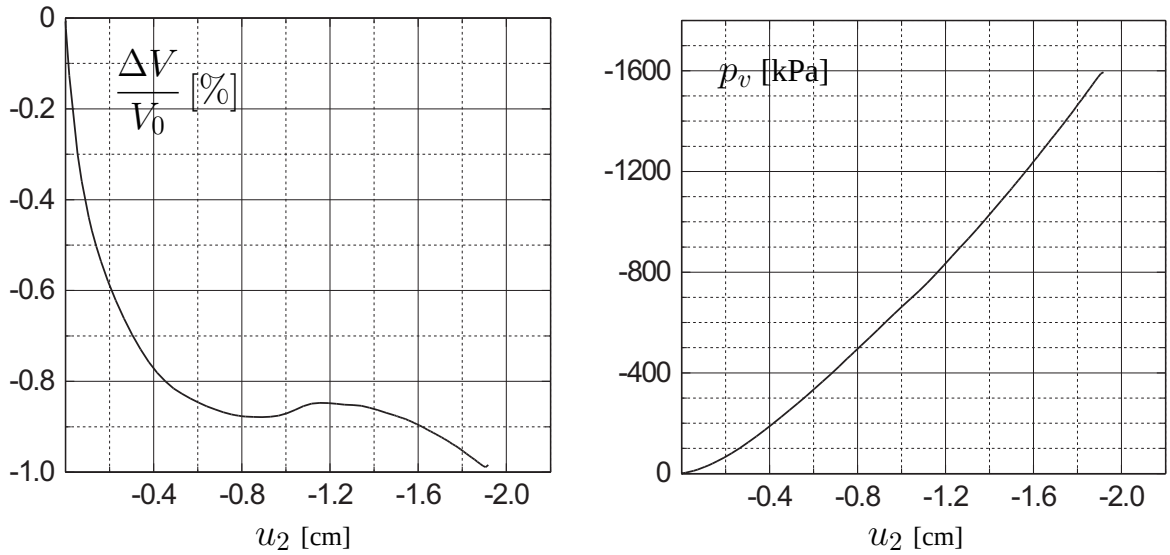

Figure 4.15: Frictionless interface: evolution of (**a**) the average value of the normalized volume change $\Delta V/V_0$, (**b**) the average value of the vertical stress p_v.

Fig. 4.17 shows the distribution of $\dot{\kappa}_{31}$ and $\dot{\kappa}_{32}$ in different sections. For $u_2 = 1.9$ cm the micro-curvature rates, $\dot{\kappa}_{31}$ and $\dot{\kappa}_{32}$, are pronounced at the middle part of section 0-0, at the top part of section 1-1 and at the bottom of the middle part of section 4-4.

The distribution of the normal stress components and the shear stress and couple stress components are shown in Fig. 4.18 and Fig. 4.19, respectively. For small prescribed vertical displacements, the normal stress, the shear stress and the couple stress components are almost constant across the sections of the soilbag. For $u_2 = 1.9$ cm the values of σ_{22}, σ_{12} and σ_{21} varies little stronger. A nonlinear distributions of μ_{31} and μ_{32} can be detected in Figs. 4.19(c) - 4.19(d).

For different states, the deformed mesh is shown in Fig. 4.20. Although there is no friction resistance in the contact zones between the soilbag and the platens the deformation is not homogeneous. In particular, the lateral sides of the soilbag become more curved with an advanced vertical displacement. Furthermore, for $u_2 = 1.9$ cm a zig-zag pattern of zones with intense localization of the deformation is clearly seen. Figs. 4.21 - 4.23 show the contour plots of the void ratio e, the volumetric strain rate $\dot{\varepsilon}_{kk}$ and the norm of the deviatoric strain rate $\|\dot{\boldsymbol{\varepsilon}}^d\|$ for different vertical compression. It can be seen that the shear band becomes more pronounced with an increase of u_2. In particular, at the beginning of the compression, i.e. for $u_2 = 0.2$ cm, the granular material in the middle part of the soilbag experiences compression, i.e. the volumetric strain rate $\dot{\varepsilon}_{kk}$ is negative (Fig. 4.22), and it is almost uniformly distributed within the soilbag (Fig. 4.21). At the left and right sides of the soilbag dilatancy, i.e. the volumetric strain rate is positive, already develops for small vertical displacements. In the filling material

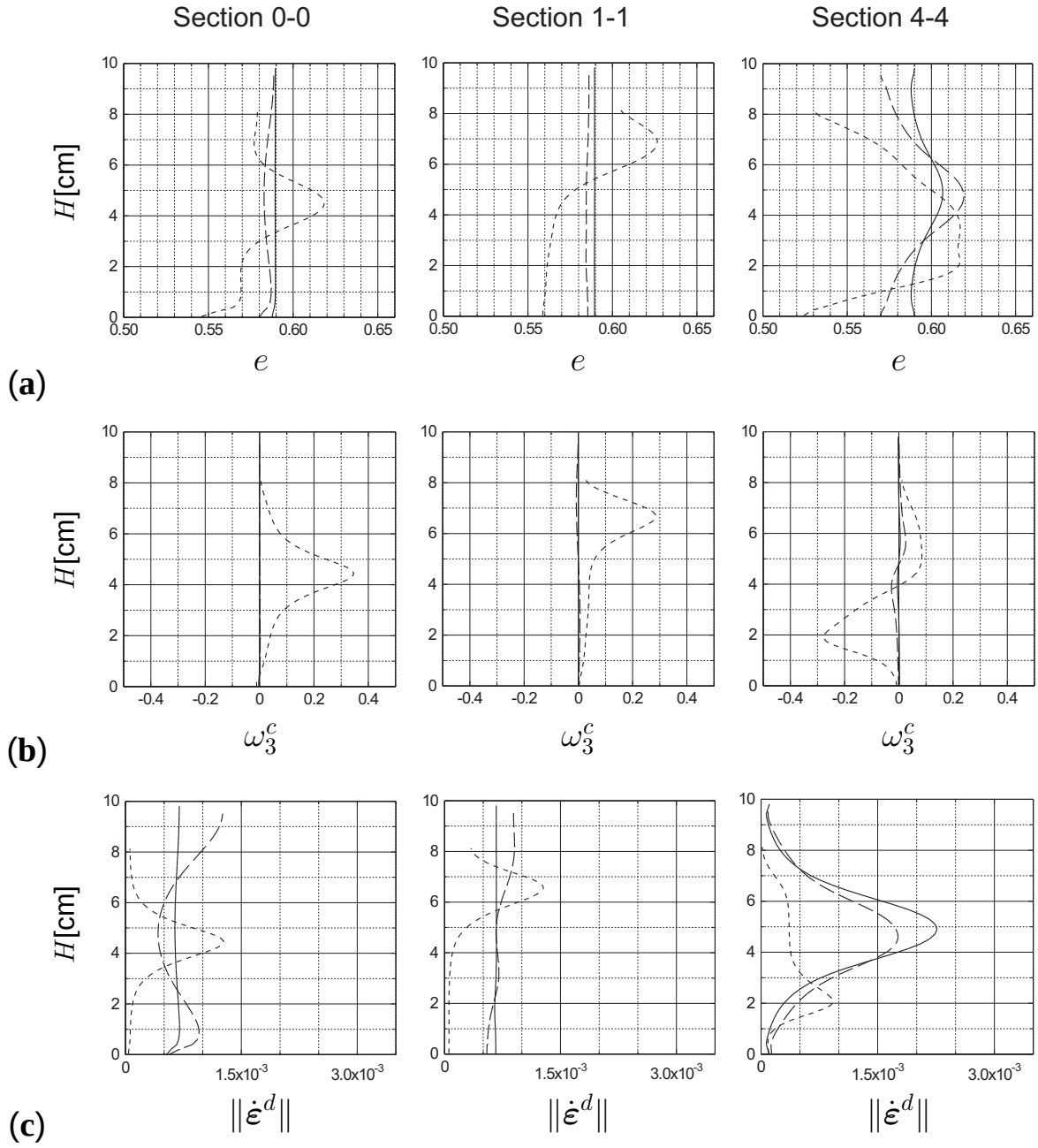

Figure 4.16: Frictionless interface: distribution of the (**a**) void ratio e, (**b**) Cosserat rotation ω_3^c (**c**) norm of the deviatoric strain rate $\|\dot{\varepsilon}^d\|$ of the granular soil at $u_2 = 0.2$ cm (solid curve), $u_2 = 0.5$ cm (long dashed curve) and $u_2 = 1.9$ cm (short dashed curve) across sections 0-0, 1-1 and 4-4.

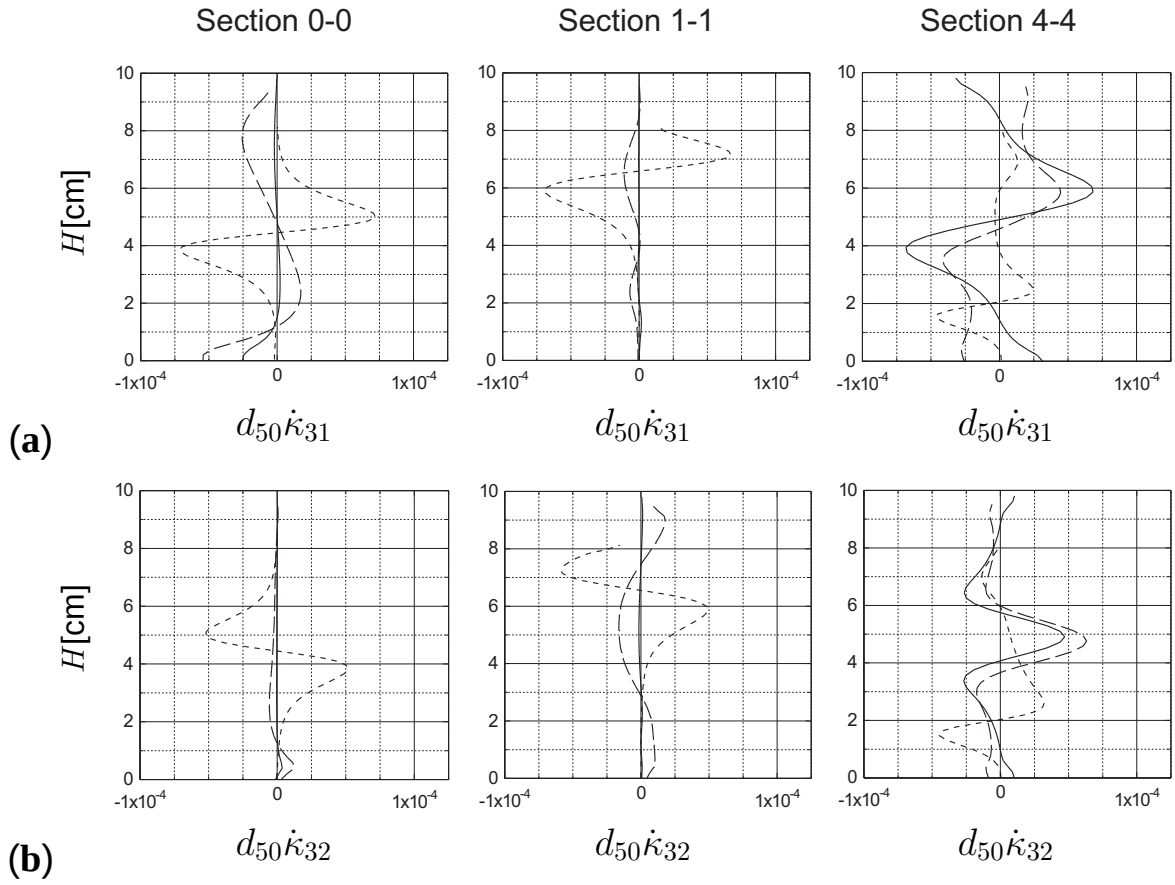

Figure 4.17: Frictionless interface: distribution of the normalized micro-curvature rates (**a**) $d_{50}\dot{\kappa}_{31}$, (**b**) $d_{50}\dot{\kappa}_{32}$ of the granular soil at $u_2 = 0.2$ cm (solid curve), $u_2 = 0.5$ cm (long dashed curve) and $u_2 = 1.9$ cm (short dashed curve) across sections 0-0, 1-1 and 4-4.

the localizations of the volumetric strain rate $\dot{\varepsilon}_{kk}$ (Fig. 4.22) and the deviatoric strain rate $\|\dot{\boldsymbol{\varepsilon}}^d\|$ (Fig. 4.23) are clearly seen from the beginning of loading. However, the shear band is not clearly observed in the contour plot of the void ratio e (Fig. 4.21). For $u_2 = 0.5$ cm two zig-zag patterns of shear bands develop (Figs. 4.22 - 4.23). With further compression, only one zig-zag pattern becomes dominant (Fig. 4.20).

From the distributions of $\dot{\varepsilon}_{kk}$ (Fig. 4.22) and $\|\dot{\boldsymbol{\varepsilon}}^d\|$ (Fig. 4.23), the inclination angles of the shear bands can be estimated. In particular, the line which passes through the middle points of the shear band at the top and the bottom surfaces is taken as a reference. It shows that for $u_2 = 0.2$ cm the inclination angle to the horizontal surface is about 51^0 - 52^0. It increases for $u_2 = 0.5$ cm up to 57^0 - 59^0. Then, with further increase of the vertical displacement the inclination angle decreases and it becomes 52^0 - 53^0 for $u_2 = 1.9$ cm.

Due to the zigzag patterns it is not reliable to measure the thickness of the shear band from

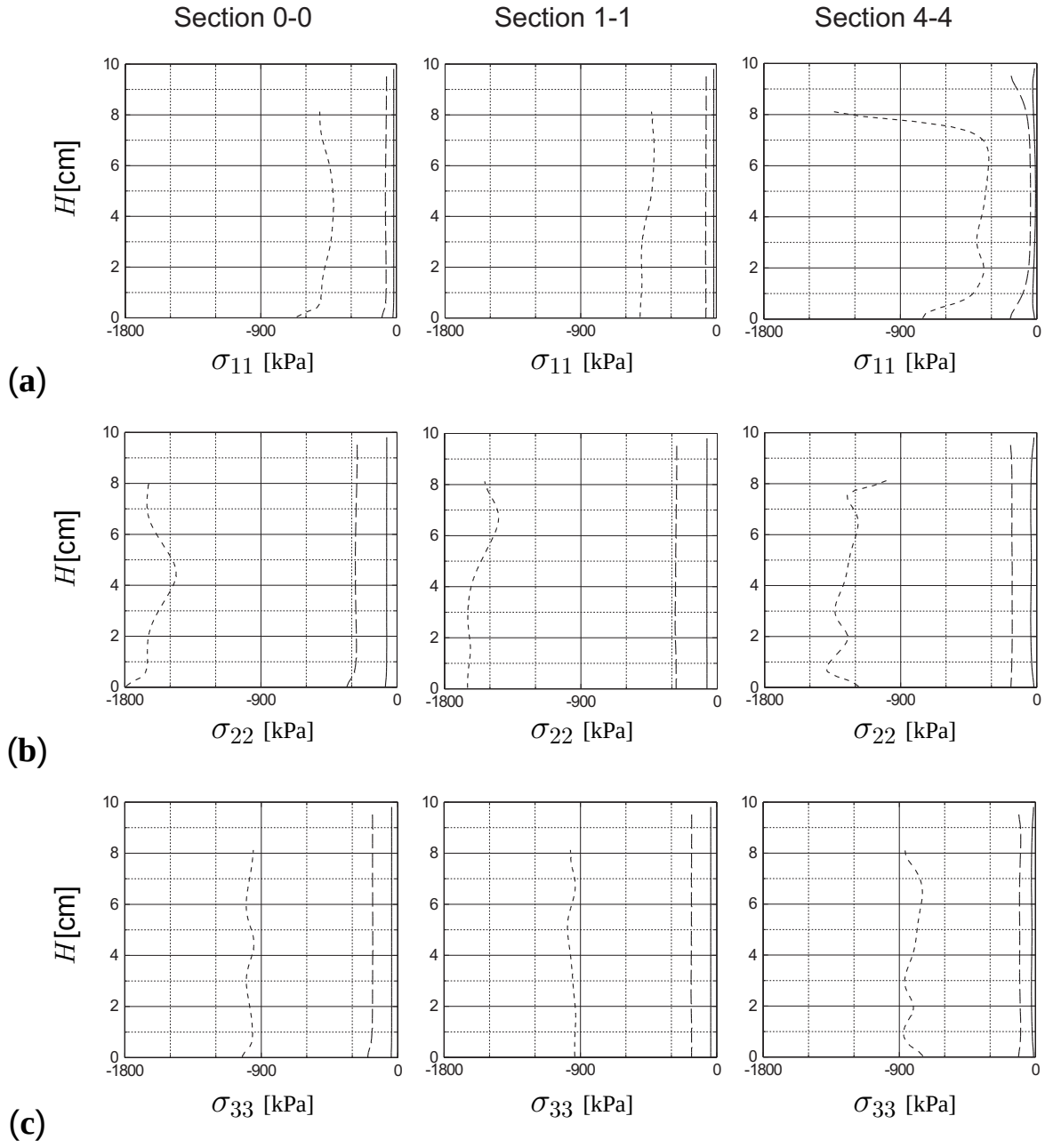

Figure 4.18: Frictionless interface: distribution of the normal stress (**a**) σ_{11}, (**b**) σ_{22} and (**c**) σ_{33} of the granular soil at $u_2 = 0.2$ cm (solid curve), $u_2 = 0.5$ cm (long dashed curve) and $u_2 = 1.9$ cm (short dashed curve) across sections 0-0, 1-1 and 4-4.

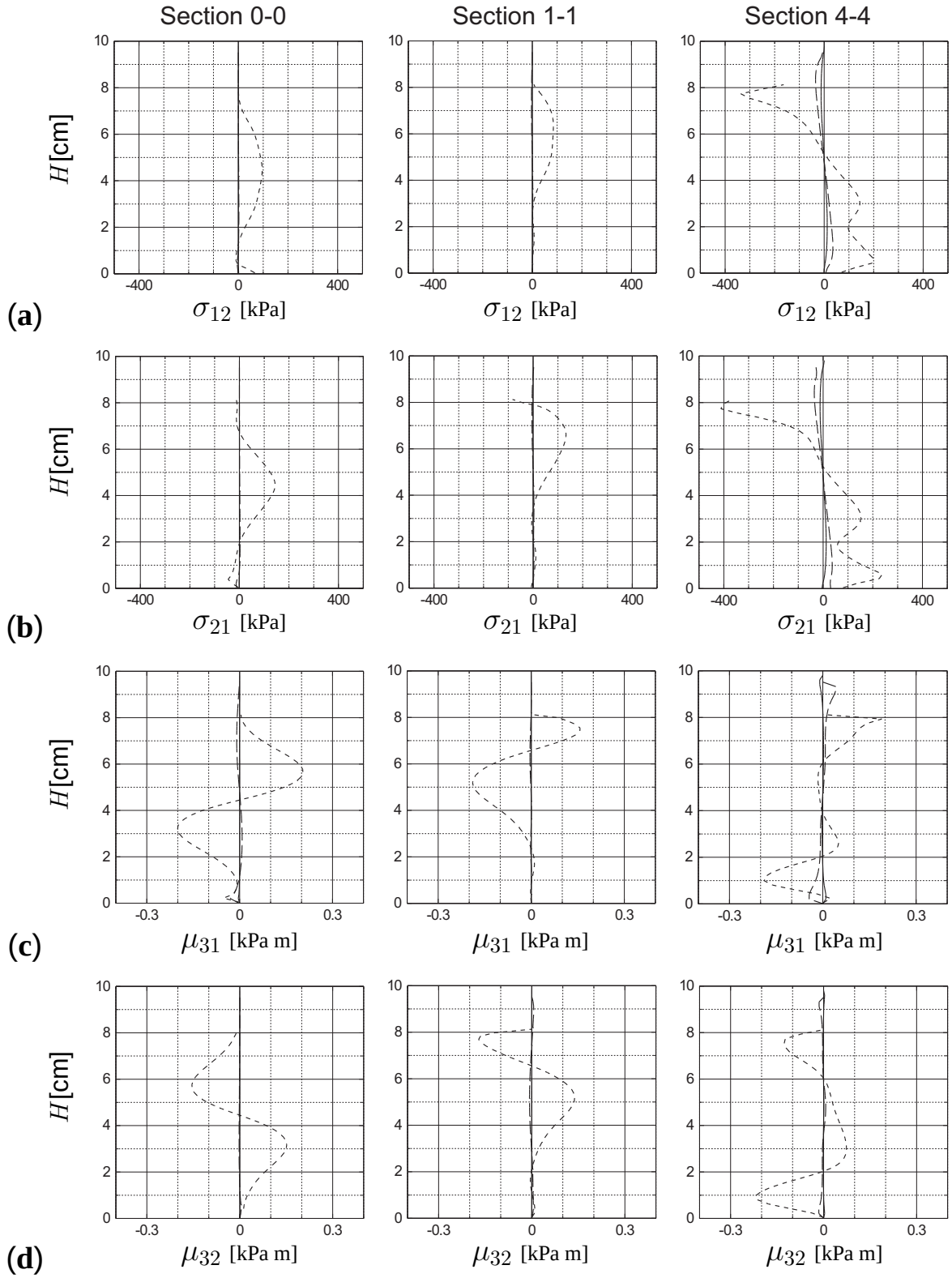

Figure 4.19: Frictionless interface: distribution of the shear stresses (**a**) σ_{12}, (**b**) σ_{21} and the couple stresses (**c**) μ_{31}, (**d**) μ_{32} of the granular soil for $u_2 = 0.2$ cm (solid curve), $u_2 = 0.5$ cm (long dashed curve) and $u_2 = 1.9$ cm (short dashed curve) across sections 0-0, 1-1 and 4-4.

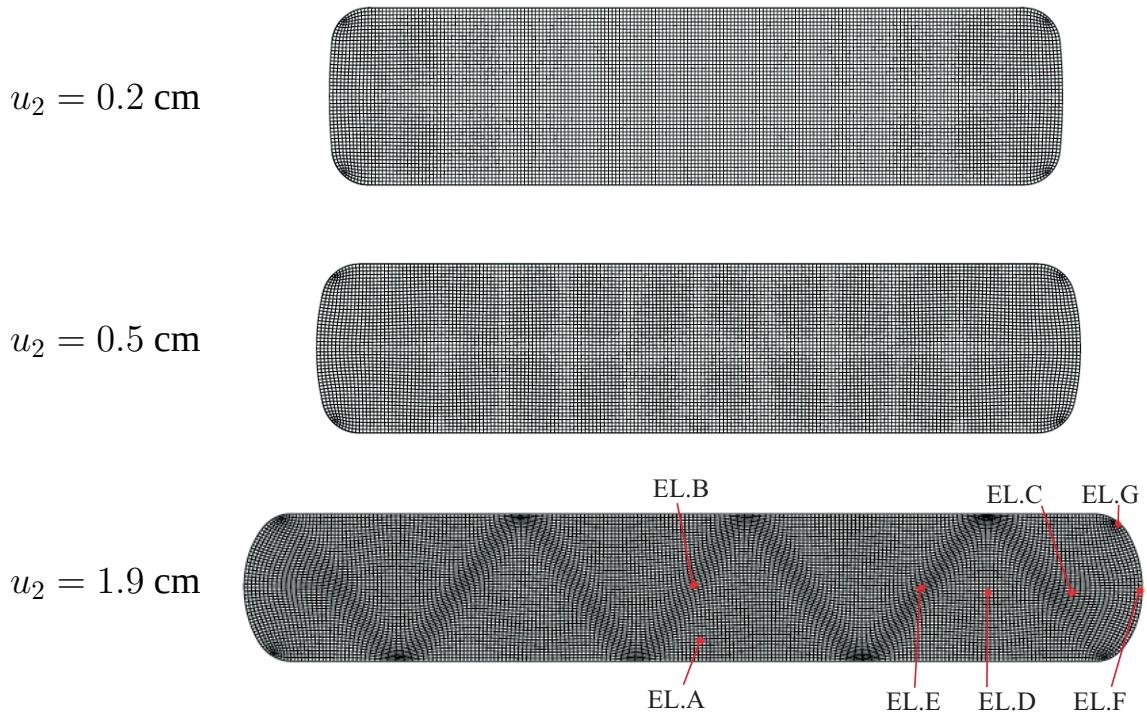

Figure 4.20: Frictionless interface: deformed shape of the soilbag for different vertical displacements u_2.

the section profile of the distributions of the void ratio, the Cosserat rotation, the strain rates or the micro-curvature rates. Therefore, it is convenient to measure the shear band thickness for instance from the contour plots of the void ratio or the strain rates. From Fig. 4.21 one can obtained at thickness of about $12.5 \times d_{50}$ to $16 \times d_{50}$. It should be mentioned that the thickness of localized zones is also influenced by the initial density and the mean pressure (e.g. Tatsuoka et al., 1986 [104]). The experimental results by Mokni (1992) and Hammad (1991) showed that the thickness of the localized zone under shearing decreases as the confining pressure and the initial density increase (Desrues & Viggiani 2004 [36]). The mean pressure increases in the filling material with an increase of the vertical displacement u_2. At the beginning of the compression the mean pressure at the left and the right sides of the soilbag, e.g. in EL.C, is lower than those at the middle part, e.g. in EL.A and EL.B (Fig. 4.24(a)). At the left and right sides of the soilbag, e.g. in EL.C in Fig. 4.24(b), dilatancy appears almost from the beginning of loading. It can be observed that strain localization starts from the area at the sides of the soilbag (Fig. 4.21, Fig. 4.22 and Fig. 4.23).

Fig. 4.24(b) shows the evolution of the void ratio at EL.A, EL.B, EL.C, EL.D and EL.E with the vertical displacement u_2. It can be seen that at the beginning of loading only compression occurs. It is followed by dilatancy shown at EL.B, EL.C and EL.E while at EL.A and EL.D only compression occurs. However, for larger vertical displacements dilatancy also occurs at

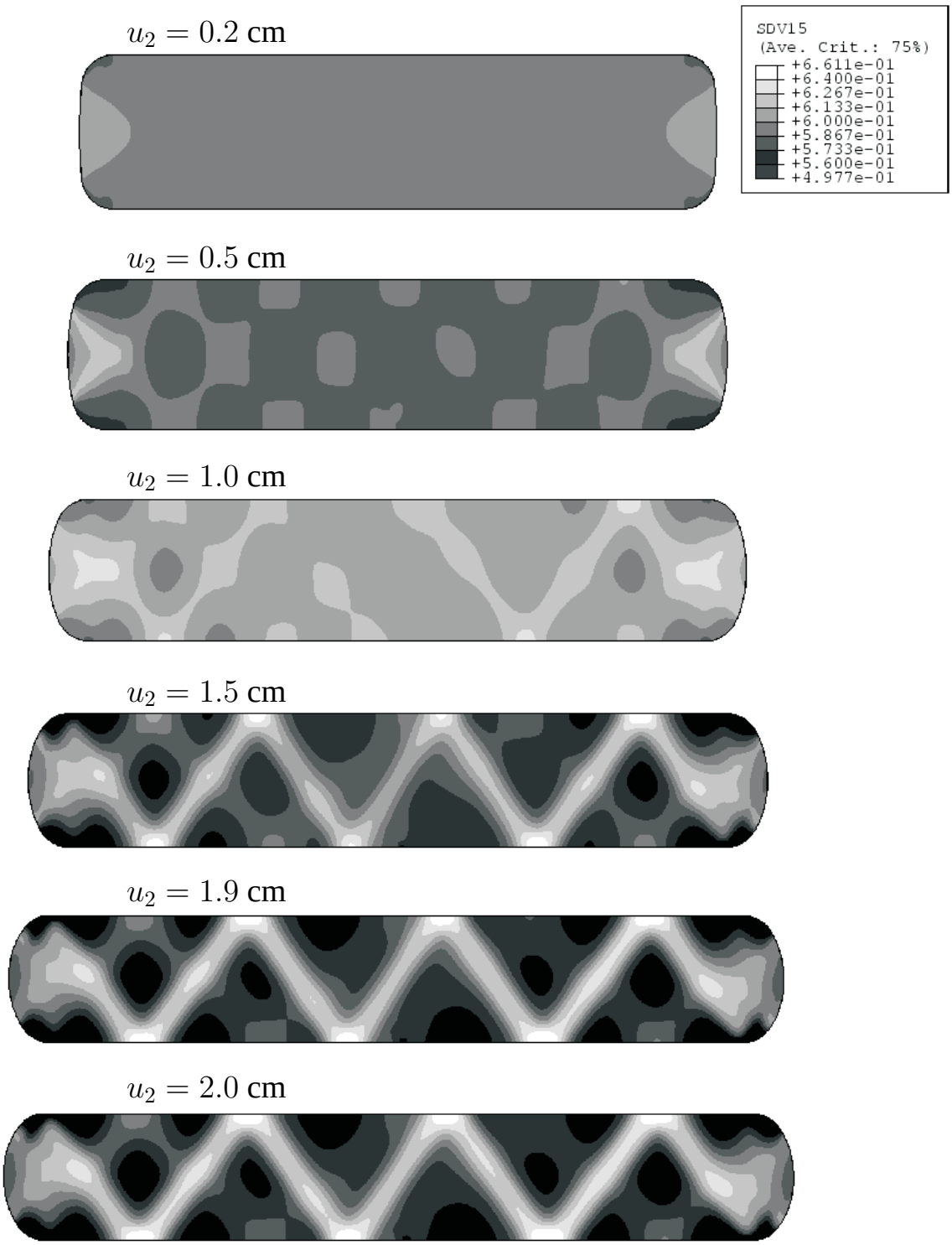

Figure 4.21: Frictionless interface: contour plot of the void ratio e for different vertical displacements u_2.

Figure 4.22: Frictionless interface: contour plot of the volumetric strain rate $\dot{\varepsilon}_{kk}$ for different vertical displacements u_2.

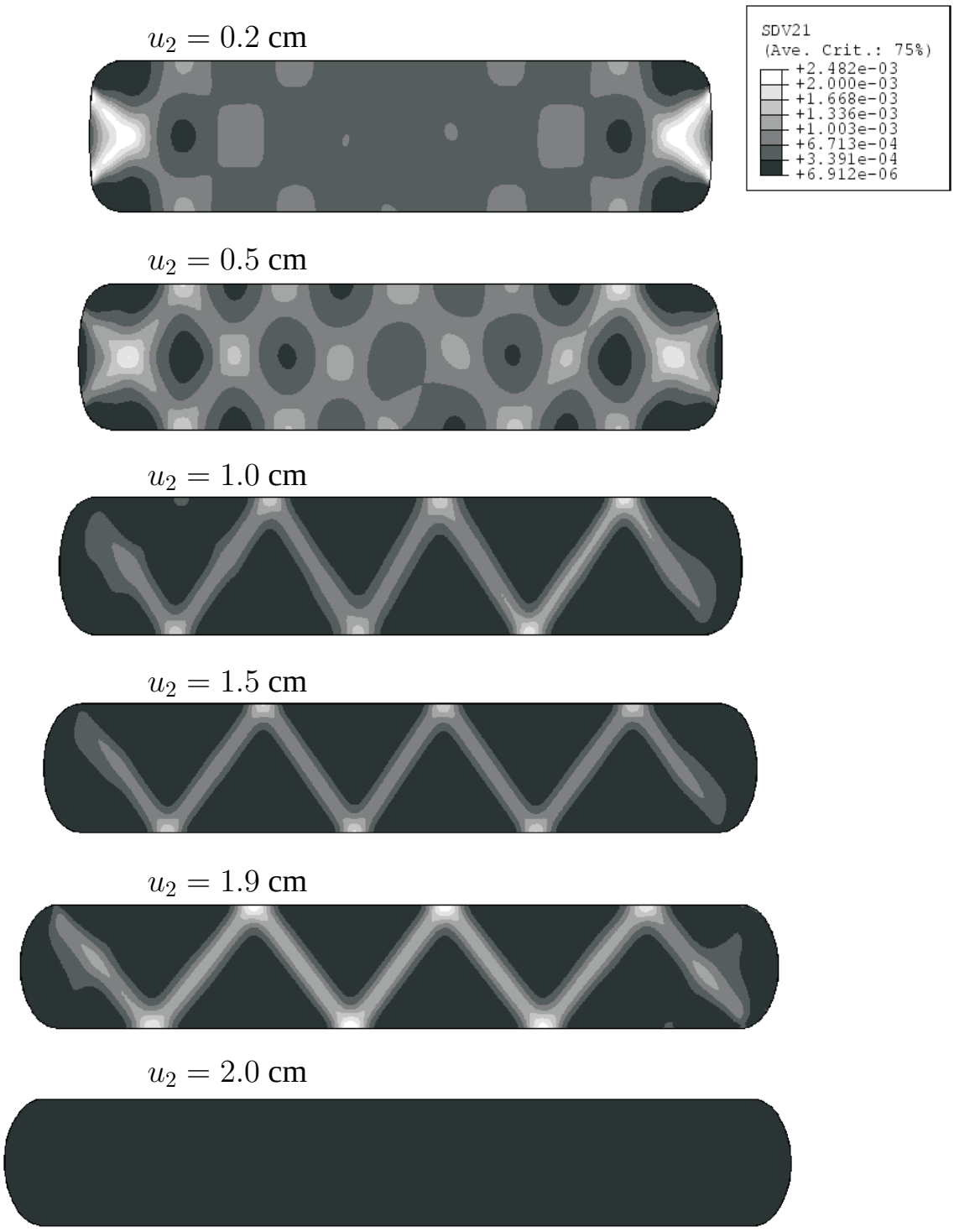

Figure 4.23: Frictionless interface: contour plot of the norm of the deviatoric strain rate $\|\dot{\boldsymbol{\varepsilon}}^d\|$ for different vertical displacements u_2.

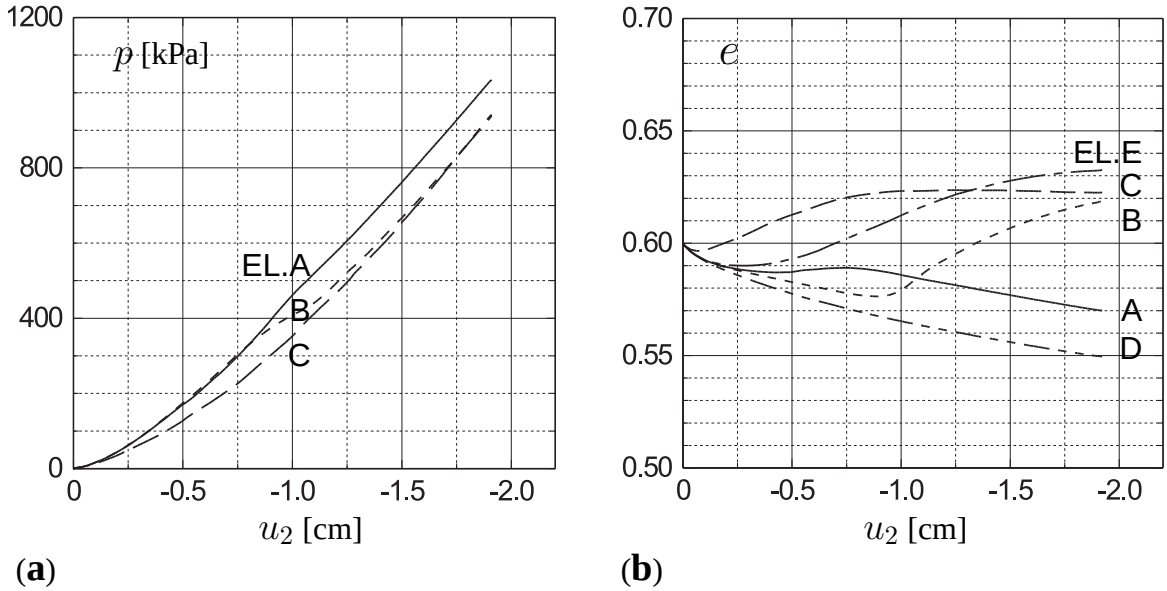

Figure 4.24: Frictionless interface: evolution of the (**a**) mean pressure $p = -\sigma_{kk}/3$ at EL.A, EL.B and EL.C. (**b**) void ratio e at EL.A, EL.B, EL.C, EL.D and EL.E.

EL.B. The elements EL.B, EL.C and EL.E are inside a localized zone while the elements EL.A and EL.D are located outside the localized zone (Fig. 4.20).

4.2.2 Comparison with the analytical results

Figs. 4.25(a) - 4.25(b) and Figs. 4.26(a) - 4.26(b) show the comparison between the results from the finite element calculation and from the analytical method for the evolutions of the quantities $\Delta L/L_0$, T/T_{limit}, p_v and K, respectively.

In particular, the nonlinear increase of $\Delta L/L_0$ and T/T_{limit} with an increase of the normalized prescribed vertical displacement, u_2/H_0, are shown in Figs. 4.25(a) - 4.25(b), where the increase of $\Delta L/L_0$ and T/T_{limit} obtained from the analytical model is higher than that for the finite element calculation. These can be explained by the initial compaction of the granular soil predicted with the hypoplastic material model, while a constant volume is assumed in the analytical model. The tensile stress of the bag increases up to the limit value of $T/T_{limit} = 1$ which is reached for a smaller vertical compression with the analytical method than with the finite element method (Fig. 4.25(b)). The corresponding vertical pressure predicted with the numerical model shows a good agreement with the analytical model (Fig. 4.26(a)). When the limit tensile stress in the wrapping material is reached the mean value of the vertical pressure p_v can further increase with an increase of u_2.

From Fig. 4.26(b) it can be seen that in contrast to the analytical model, the predicted stress ratio

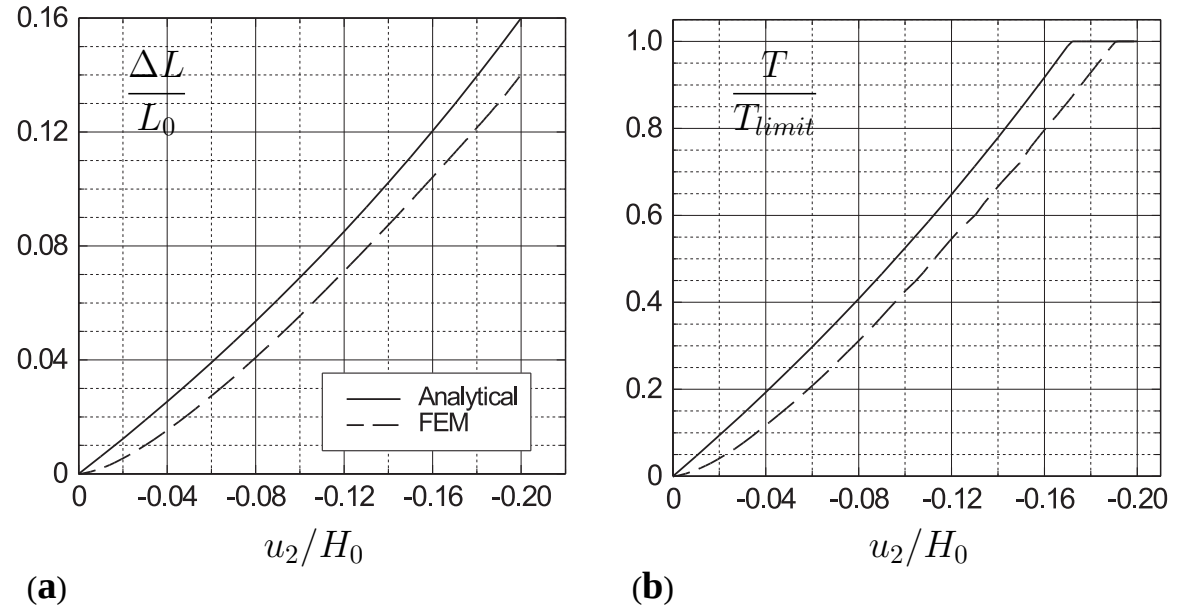

Figure 4.25: Comparison between the analytical and the finite element model for the evolution of (**a**) the normalized change of perimeter $\Delta L/L_0$ and (**b**) the normalized tensile force T/T_{limit} in the wrapping material.

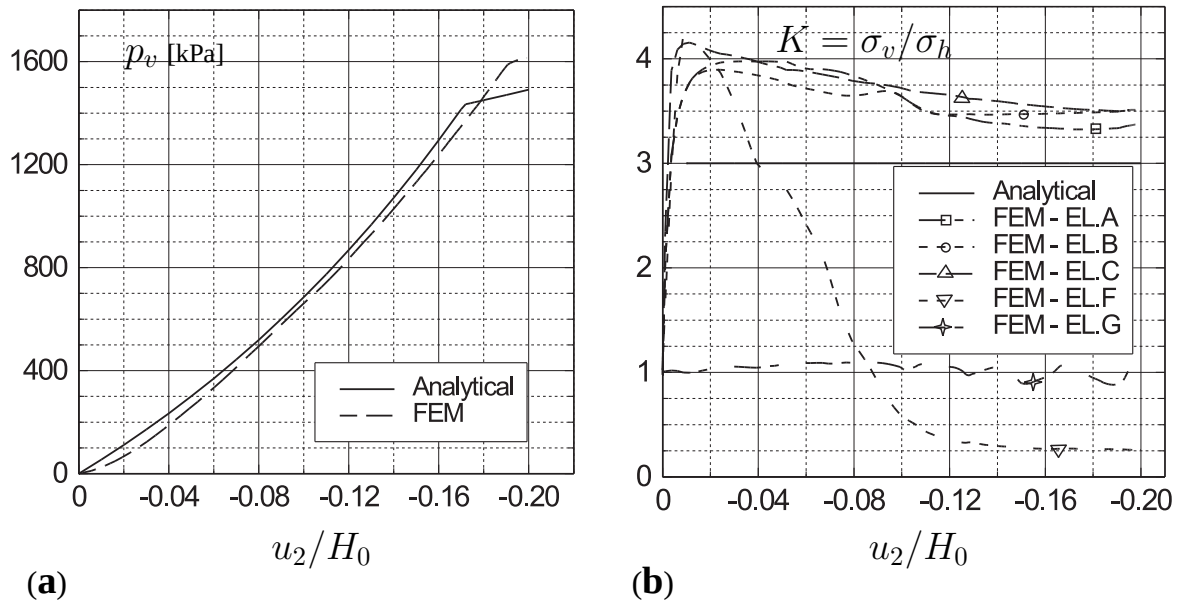

Figure 4.26: Comparison between the analytical and the finite element model for the evolution of (**a**) the applied vertical pressure p_v and (**b**) the stress ratio $K = \sigma_v/\sigma_h$.

K obtained from the hypoplastic material model is not constant during the compression and it is not homogeneously distributed. For example the stress ratio K in the middle of the soilbag, e.g. in elements EL.A, EL.B, EL.C, is higher than that close to the lateral boundaries, e.g. EL.G. In EL.A, EL.B and EL.C the stress ratio increases from the initially isotropic condition up to the peak value which is higher in EL.C than in EL.A and EL.B. After the peak, the stress ratio decreases and it tends towards a stationary value of $K = 3$. The asymptotic value, however, is not clearly detected. Close to the lateral part of the boundary with an initially circular shape, the stress ratio is close to one, e.g.at EL.G (Fig. 4.12). This indicates that for the analytical model proposed in Section 4.1.2 the assumption of $K = 1$ is rather realistic for the part of the soilbag close to a boundary with the circular shape. For EL.F which is located in the middle of the soilbag close to the lateral boundary with a small curvature, the stress ratio decreases to a value of less than one.

Furthermore, the numerical simulation shows that the volume change during compression is rather small, e.g. it is about 1% for the vertical compression of 2 cm (Fig. 4.15(a)). Thus, the assumption of a constant volume for the analytical model seems to be reasonable.

From the above comparisons it can be concluded that for the same vertical compression the predicted $\Delta L/L_0$ and T via the analytical model is slightly higher than that for the numerical model. The differences are due to the simplifications assumed for the analytical model.

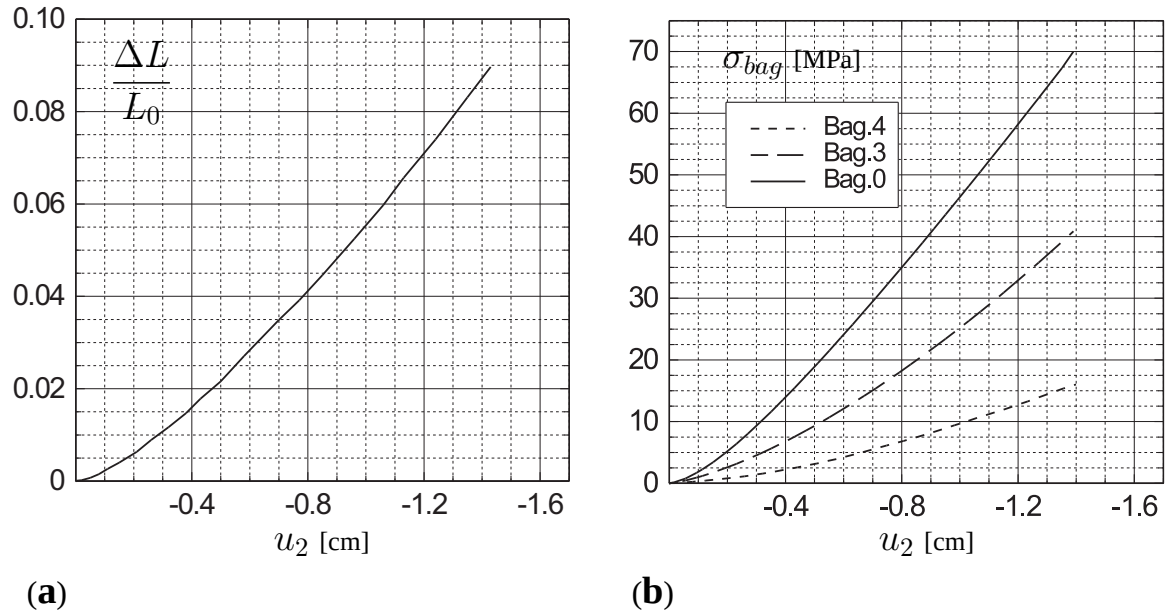

Figure 4.27: Interlocked interface: evolution of (**a**) the normalized change of perimeter $\Delta L/L_0$ and (**b**) the tensile stress σ_{bag} at Bag.0, Bag.3 and Bag.4.

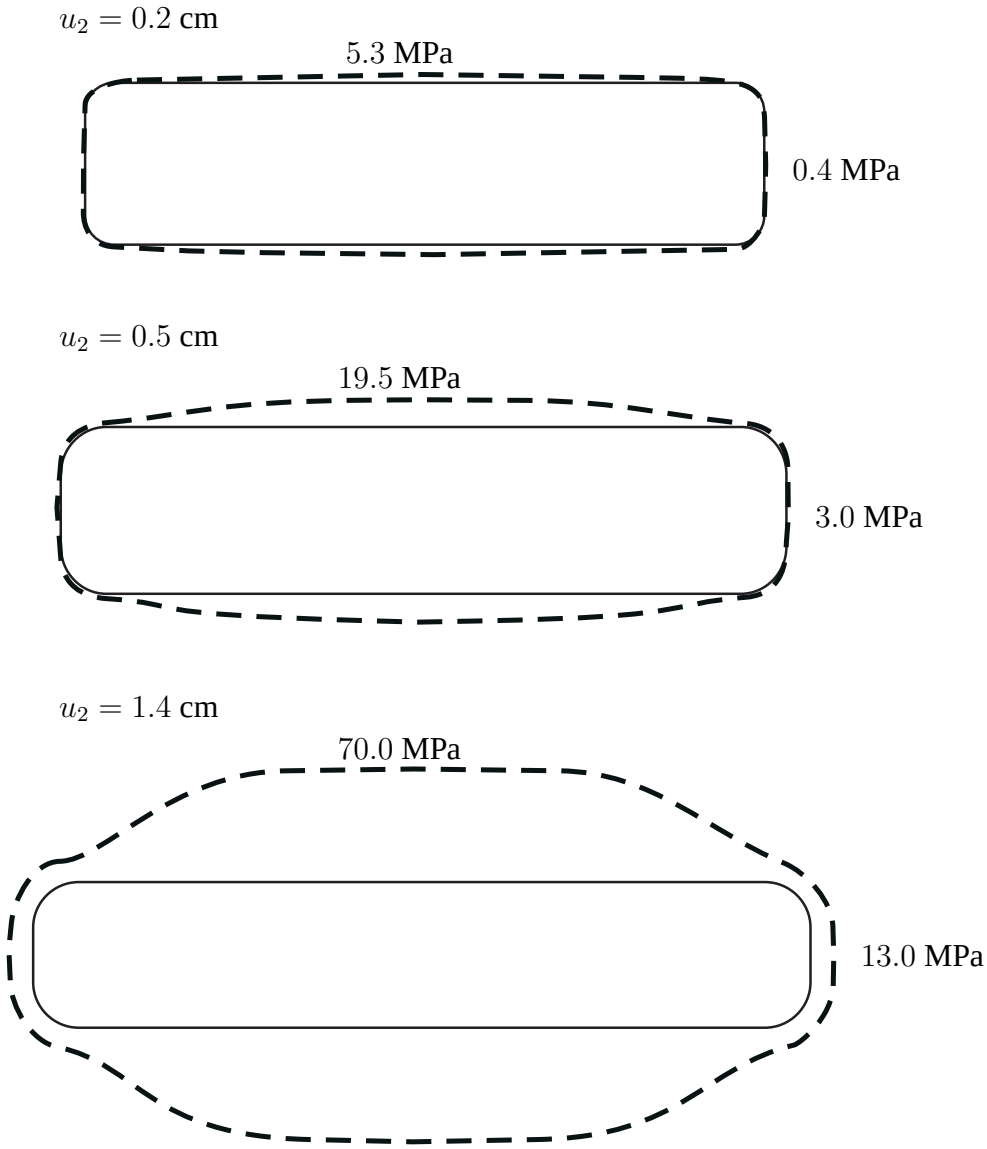

Figure 4.28: Interlocked interface: distribution of tensile stress in the wrapping material for different vertical displacements u_2.

4.2.3 Interlocked interface behavior

In the following the evolution of the stress and strain is investigated for the case that no relative displacements and Cosserat rotations along the interface between the soil and the wrapping bag take place. Fig. 4.27(a) shows that for an increase of the vertical displacement u_2 the normalized perimeter of the soilbag, $\Delta L/L_0$, as well as the tensile stress σ_{bag} in the wrapping material nonlinearly increases. The distribution of the tensile stress in the wrapping material is not uniform, as shown in Fig. 4.28. In particular for the same prescribed vertical displacement

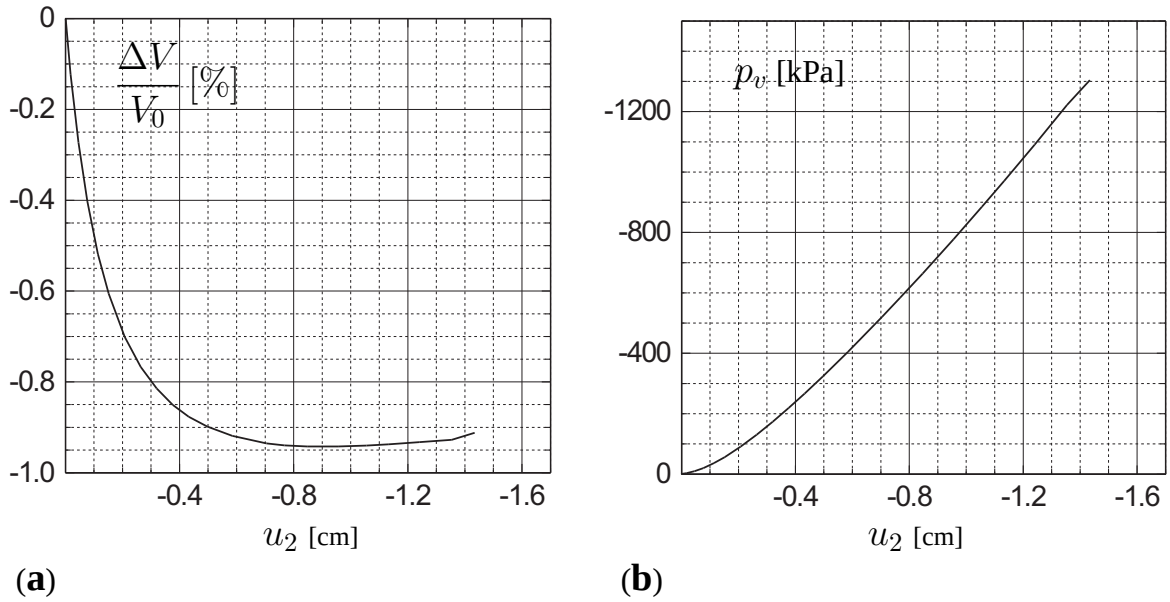

Figure 4.29: Interlocked interface: evolution of the (**a**) average value of the normalized volume change $\Delta V/V_0$, (**b**) average value of the vertical pressure p_v.

u_2 the tensile stress in the middle of the soilbag is higher than on the sides. For $u_2 = 1.4$ cm the limit tensile stress is reached in the middle of the soilbag (Bag.0 in Fig. 4.27(b)). Fig. 4.29(a) and Fig. 4.29(b) show the evolutions of $\Delta V/V_0$ and of p_v, respectively. The soilbag experiences only compression up to about $u_2 = 1.0$ cm (Fig. 4.29(a)), with a maximum volume change of less than 1% of V_0. The mean vertical pressure p_v nonlinearly increases with the increase of u_2, as shown in Fig. 4.29(b).

Fig. 4.30, Fig. 4.31, Fig. 4.32 and Fig. 4.33 show the distributions of the void ratio e, the Cosserat rotation ω_3^c, the norm of the deviatoric strain rate, $\|\dot{\boldsymbol{\varepsilon}}^d\|$, the normalized micro-curvature rates ($d_{50}\dot{\kappa}_{31}$, $d_{50}\dot{\kappa}_{32}$), the normal stresses (σ_{11}, σ_{22}, σ_{33}), the shear stresses (σ_{12}, σ_{21}) and couple stresses (μ_{31}, μ_{32}) in different sections and for the prescribed vertical displacements of $u_2 = 0.2$, 0.5 and 1.4 cm. The state variables across sections 0-0 and 1-1 for the vertical displacements of $u_2 = 0.2$, 0.5 cm are rather homogeneously distributed while state variables across section 4-4 are nonlinearly distributed for a higher vertical displacements. While in section 0-0 and section 1-1 the void ratio decreases, it increases in section 4-4 and shows the maximum value in the middle. Fig. 4.30(b) shows that Cosserat rotations, ω_3^c, are only significant in section 4-4, where the particles rotate clockwise, i.e. $\omega_3^c > 0$, in the upper part and anti-clockwise, i.e. $\omega_3^c < 0$, in the lower part of the soilbag. In Fig. 4.30(c), the distribution of the norm of the deviatoric strain rate, $\|\dot{\boldsymbol{\varepsilon}}^d\|$, across section 4-4 is heterogeneous while its distributions across the sections 0-0 and 1-1 are rather homogeneous. The micro-curvature rates, $\dot{\kappa}_{32}$, are only pronounced in section 4-4 (Fig. 4.31). From Fig. 4.30 and Fig. 4.31 it can be concluded that strain localization accompanied with dilatancy, micro-curvature rates and Cosserat rotation is only significant in the lateral parts of the soilbag. In contrast to the frictionless inter-

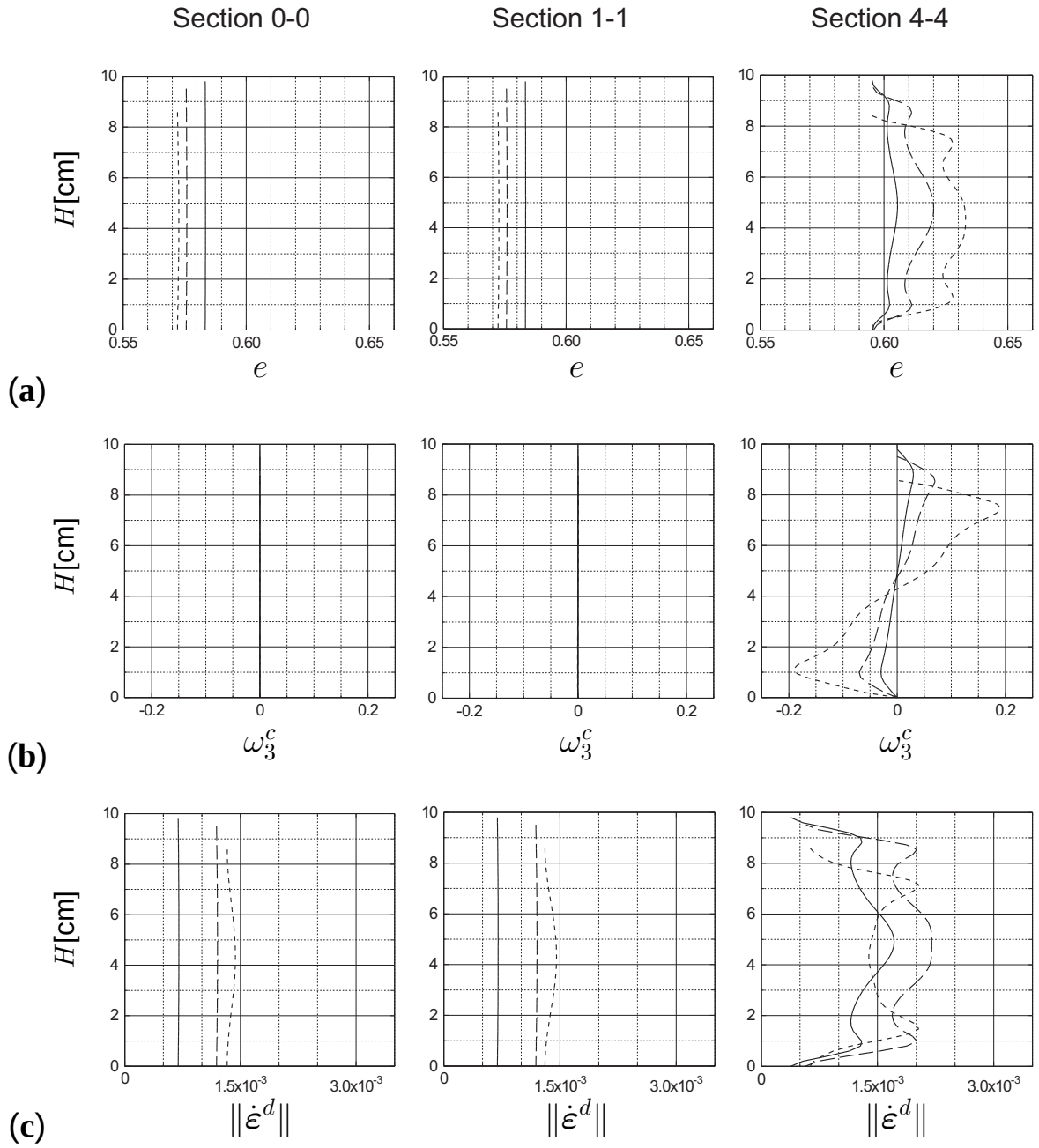

Figure 4.30: Interlocked interface: distribution of (**a**) the void ratio e, (**b**) the Cosserat rotation ω_3^c and (**c**) the norm of the deviatoric strain rate $\|\dot{\varepsilon}^d\|$ for $u_2 = 0.2$ cm (solid curve), $u_2 = 0.5$ cm (long dashed curve) and $u_2 = 1.4$ cm (short dashed curve) across sections 0-0, 1-1 and 4-4.

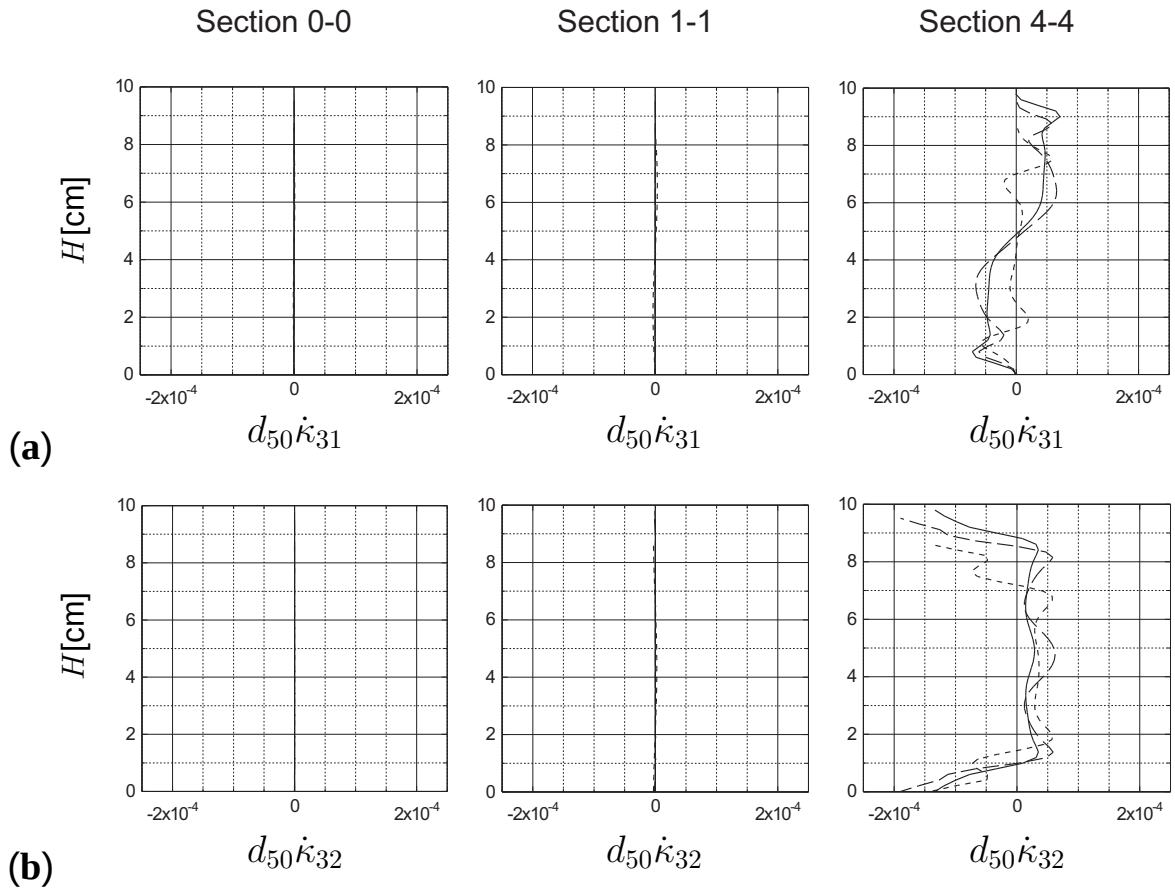

Figure 4.31: Interlocked interface: distribution of the normalized micro-curvature rates (**a**) $d_{50}\dot{\kappa}_{31}$, (**b**) $d_{50}\dot{\kappa}_{32}$ for $u_2 = 0.2$ cm (solid curve), $u_2 = 0.5$ cm (long dashed curve) and $u_2 = 1.4$ cm (short dashed curve) across sections 0-0, 1-1 and 4-4.

face, the deformation in the middle part of the soilbag is rather homogeneous, also for higher vertical compressions.

Fig. 4.32 shows a homogeneous distributions of σ_{11}, σ_{22} and σ_{33} across sections 0-0, 1-1 and 4-4 for $u_2 = 0.2$ cm and also for $u_2 = 0.5$ cm. For $u_2 = 1.4$ cm the distributions becomes heterogeneous across section 4-4. Across section 0-0 and section 1-1 the distributions of σ_{12}, σ_{21} and μ_{31}, μ_{32} are very close to zero (Figs. 4.33). Across section 4-4, a heterogeneous distribution of the state quantities becomes more pronounced for higher vertical compression.

For the vertical displacements of $u_2 = 0.2$, 0.5 and 1.4 cm the deformed mesh, the contour plot of the void ratio and the contour plot of the deviatoric strain rate are shown in Figs. 4.34, 4.35 and 4.36, respectively. With an increase of u_2 the area of intense shear strain rate expands to the middle part of the soilbag. It is obvious that also for higher vertical compressions no discrete

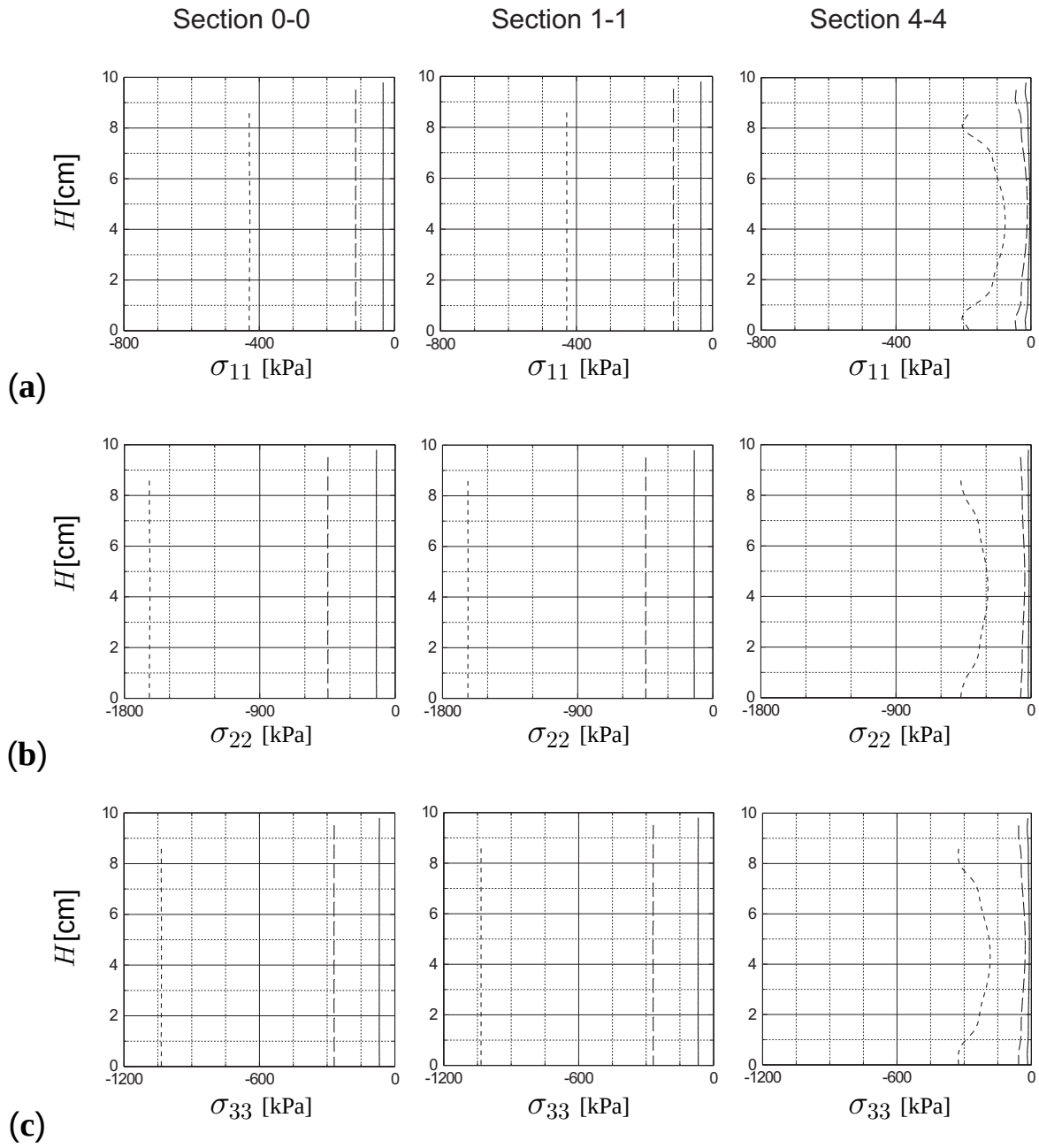

Figure 4.32: Interlocked interface: distribution of the normal stress (**a**) σ_{11}, (**b**) σ_{22} and (**c**) σ_{33} for $u_2 = 0.2$ cm (solid curve), $u_2 = 0.5$ cm (long dashed curve) and $u_2 = 1.4$ cm (short dashed curve) across sections 0-0, 1-1 and 4-4.

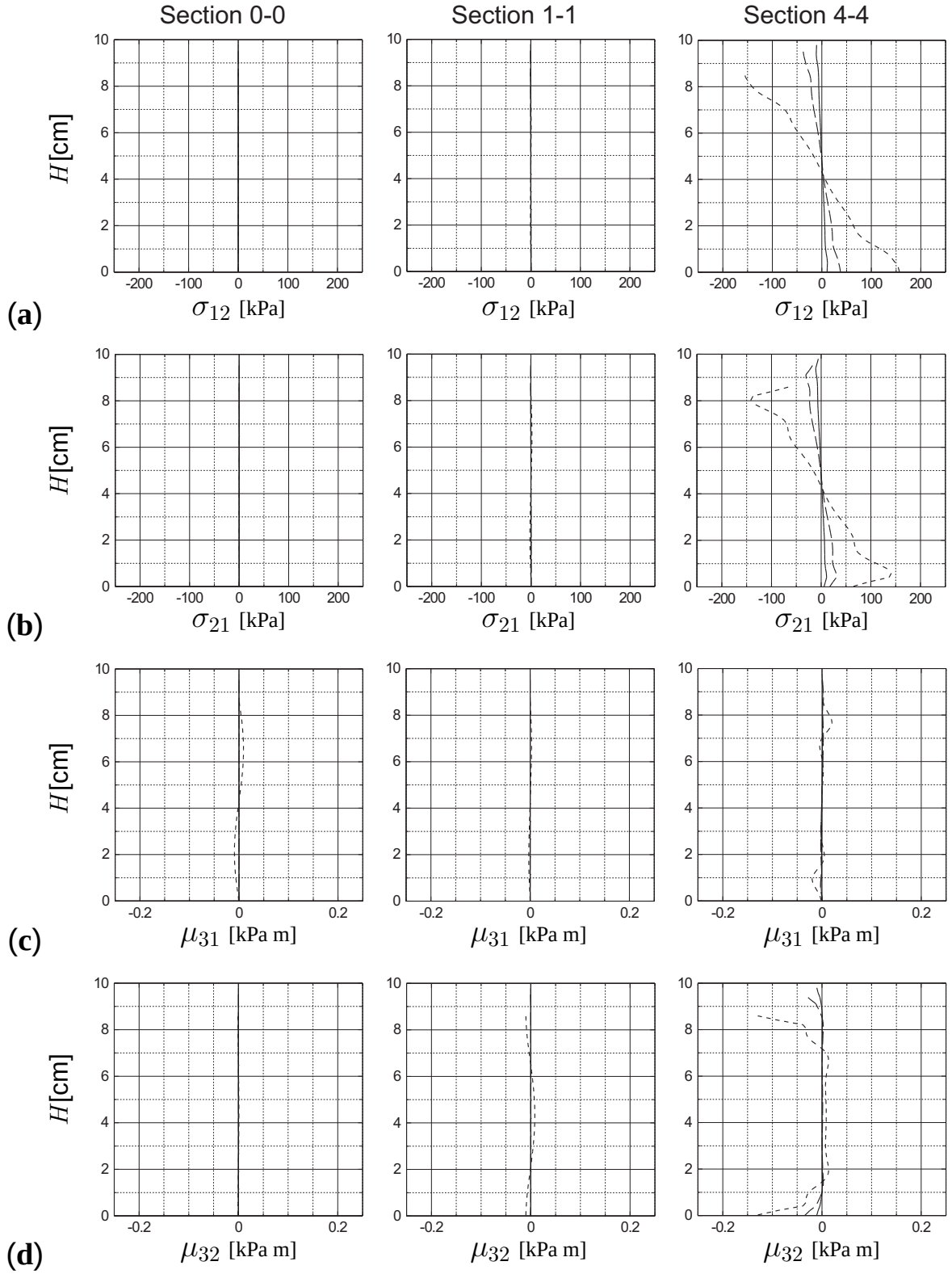

Figure 4.33: Interlocked interface: distribution of the shear stress (**a**) σ_{12}, (**b**) σ_{21} and the couple stress (**c**) μ_{31}, (**d**) μ_{32} for $u_2 = 0.2$ cm (solid curve), $u_2 = 0.5$ cm (long dashed curve) and $u_2 = 1.4$ cm (short dashed curve) across sections 0-0, 1-1 and 4-4.

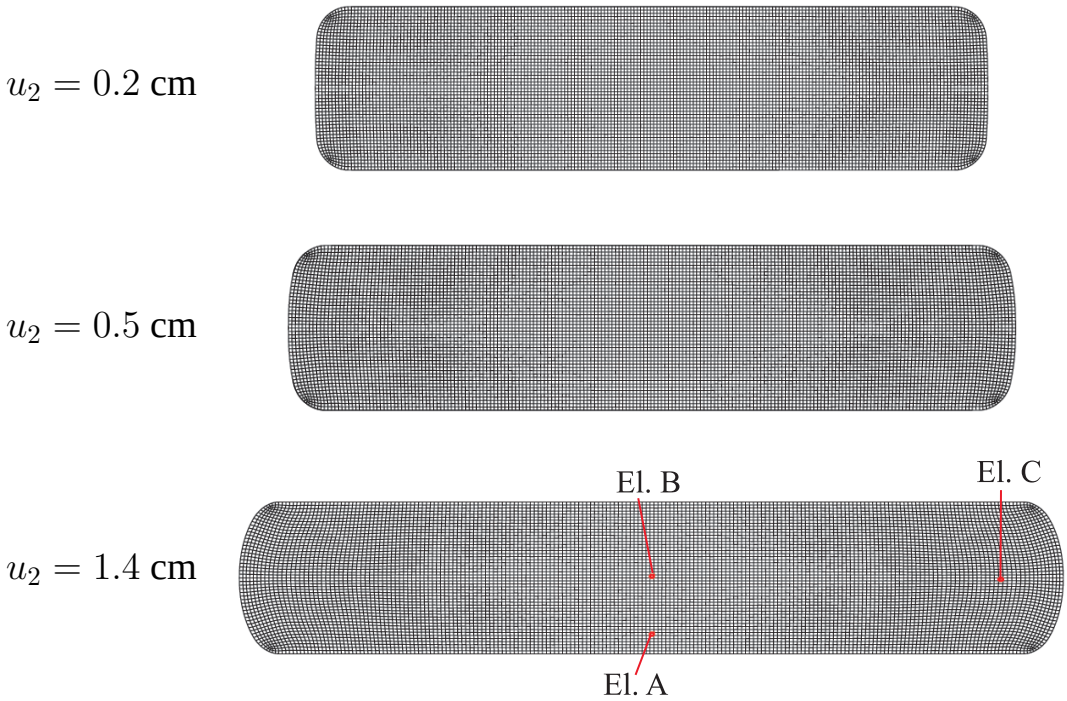

Figure 4.34: Interlocked interface: deformed shape of the soilbag for different vertical displacements u_2.

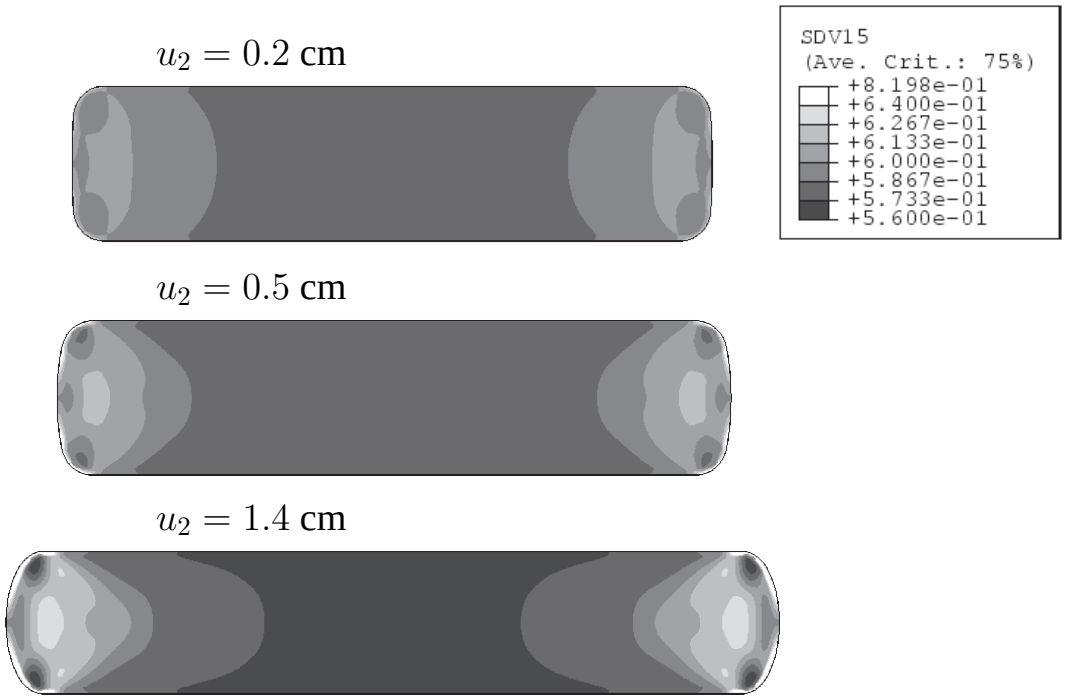

Figure 4.35: Interlocked interface: contour plot of the void ratio e for different vertical displacements u_2.

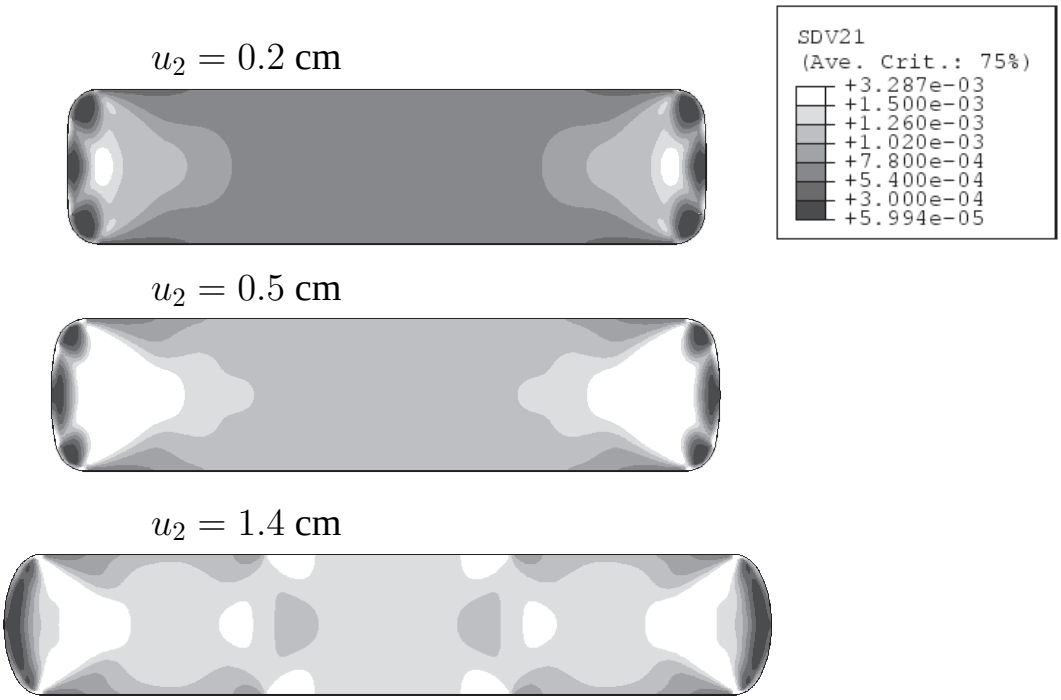

Figure 4.36: Interlocked interface: contour plot of the norm of the deviatoric strain rate $\|\dot{\boldsymbol{\varepsilon}}^d\|$ for different vertical displacements u_2.

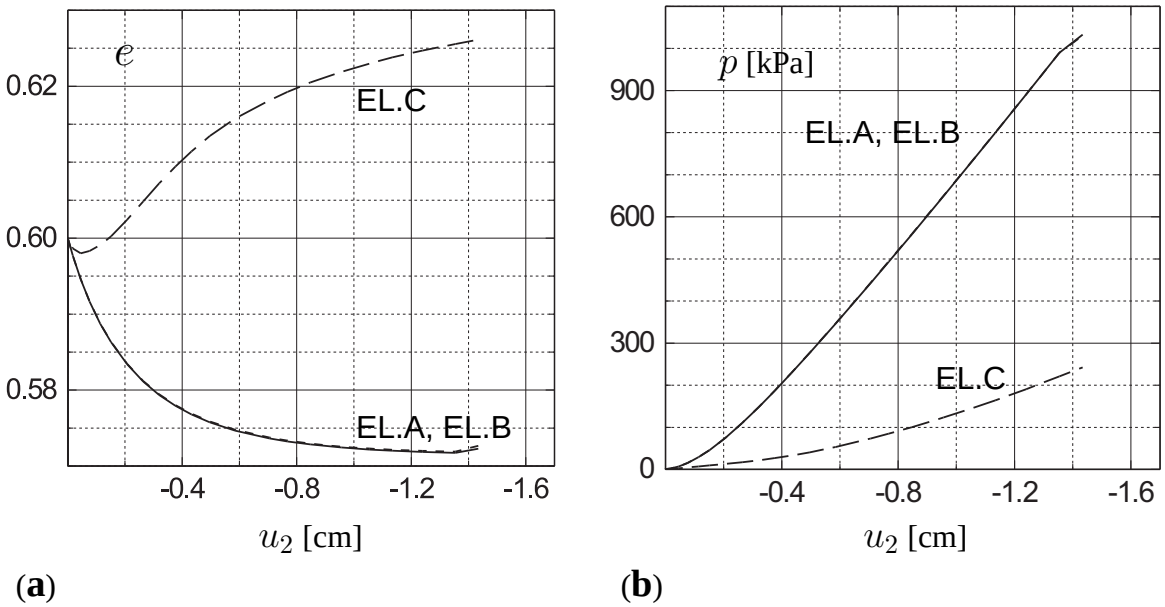

Figure 4.37: Interlocked interface: evolution of the (**a**) void ratio e, (**b**) mean pressure $p = -\sigma_{kk}/3$ at EL.A, EL.B and EL.C.

shear band occurs. While in the middle part densification is dominant dilatancy can only be detected at the sides part of the soilbag (Fig. 4.35 and Fig. 4.37(a)). For the same vertical displacement u_2 the mean pressure p in the filling material at EL.C is lower than at EL.A and EL.B (Fig. 4.37(b)).

4.2.4 Influence of random distribution of the initial void ratio

In this section the influence of a random distribution of the initial void ratio on the soil deformation inside the soilbag is investigated. For generating a random distribution of the initial void ratio a density function $f(e)$ with the so-called β-distribution is used (e.g. Grimmett & Stirzaker, 1992 [49]). From basics of statistics a probability density function $f(e)$ of the void ratio e must fulfil the following requirements:

$$f(e) \geq 0, \tag{4.40}$$

and

$$\int_{-\infty}^{\infty} f(e)\, de = 1. \tag{4.41}$$

The density function with β-distribution for the void ratio e reads:

$$\begin{aligned} f(e) &= \frac{1}{B\,(p,q)\;(b-a)^{p+q-1}}\;(e-a)^{p-1}\,(b-e)^{q-1} \quad \text{for} \quad a \leq e \leq b, \\ f(e) &= 0 \qquad\qquad\qquad\qquad\qquad\qquad\qquad\qquad\quad \text{for} \quad e < a \text{ or } e > b. \end{aligned} \tag{4.42}$$

Herein, a is the lower bound of e which can be related to the minimum void ratio and b is the upper bound of e which can be related to the maximum void ratio. In contrast to the pressure dependent relation 2.41 for the limit void ratios, the corresponding values are assumed here to be constant, i.e. $a = e_{d0}$, $b = e_{i0}$. The parameters p and q are defined as:

$$p = \frac{e_m - a}{b-a}\left[\frac{(e_m-a)\,(b-e_m)}{s} - 1\right], \quad q = \frac{b-e_m}{b-a}\left[\frac{(e_m-a)\,(b-e_m)}{s} - 1\right]. \tag{4.43}$$

In Eq. 4.43 e_m is a given mean value of the void ratio and s is a given variance, which is the square of the standard deviation d, i.e. $s = d^2$. With the magnitude of s the range of random void ratios can be chosen. In order to fulfil the requirements $p > 0$ and $q > 0$ the value of s is restricted by $s < (e_m - a)(b - e_m)$. The constant $B(p,q)$ in Eq. 4.42 is obtained from the so-called β-function: (e.g. Grimmett & Stirzaker, 1992 [49])

$$B(p,q) = \int_0^1 e^{p-1}\,(1-e)^{q-1}\; de. \tag{4.44}$$

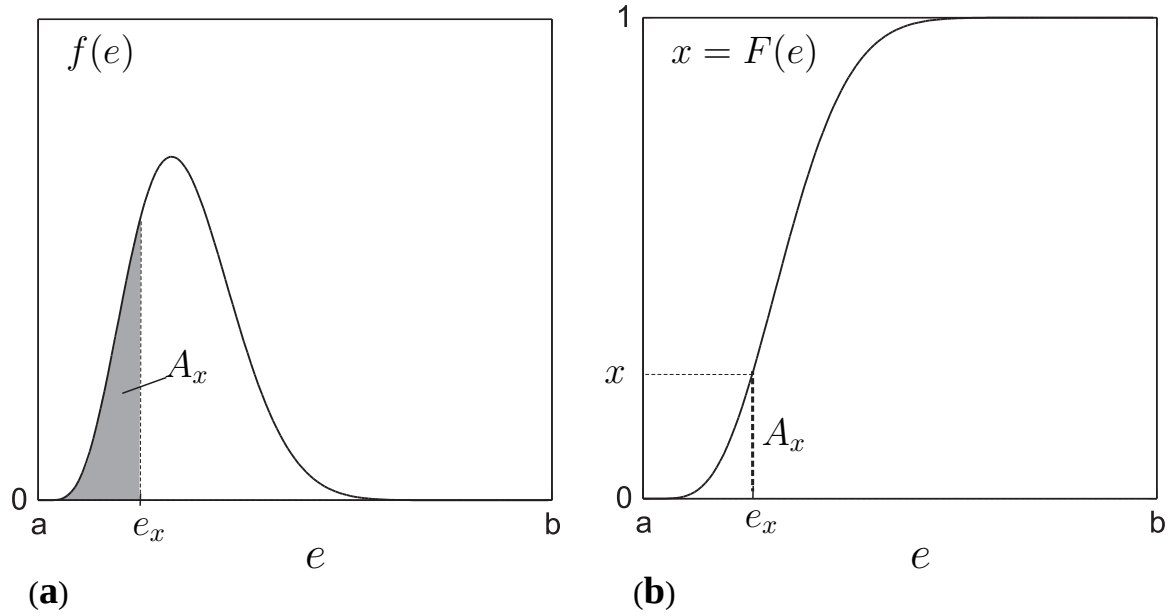

Figure 4.38: (**a**) Frequency distribution $f(e)$ of the void ratio e, (**b**) cumulative frequency distribution $F(e)$ of the void ratio e

It is worth mentioning that the requirement in Eq. 4.41 will be fulfilled with $B(p,q)$ defined in Eq. 4.44 as shown in detail in Appendix C.

The cumulative probability distribution $F(e)$ can be obtained by integration of the density function $f(e)$, i.e.

$$F(e) = \int_a^e f(e)de. \tag{4.45}$$

The cumulative probability distribution lies in the range between $F(e = a) = 0$ and $F(e = b) = 1$, as shown in Fig. 4.38(b).

A uniform random number generator, i.e. a random number generator which generates random numbers of uniform deviation (e.g. Press et al., 1992 [98]), is used to generate random values between $[0, 1]$. In order to relate the random value x to the desired void ratio e the cumulative frequency density $F(e)$ is used, i.e.

$$x(e) = F(e). \tag{4.46}$$

This means that the random variable x has probability density $f(e)$. Eq. 4.46 allows an immediate geometric interpretation as sketched in Fig. 4.38. A chosen random value x is related to the corresponding void ratio e via the shaded area A_x in Fig. 4.38(a). The value of A_x is

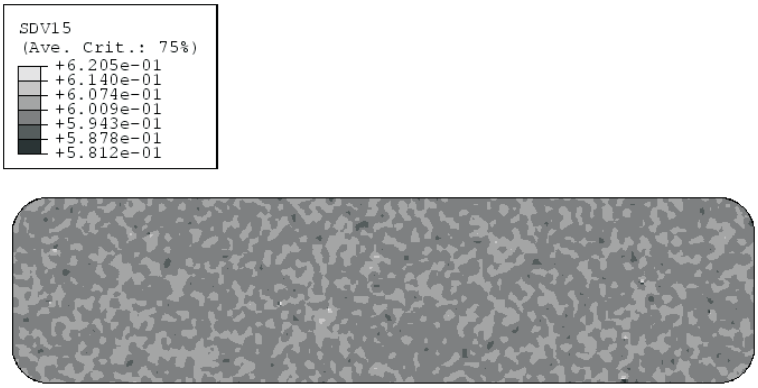

Figure 4.39: Contour plot of the initial random distribution of the void ratio.

equal to $F(e)$ as shown by the dashed line in Fig. 4.38(b). In Eq. 4.46 the parameter e is unknown. It can be computed with the so-called transformation method (e.g. Press et al., 1992 [98]) according to

$$e = F^{-1}(x), \tag{4.47}$$

where, $F^{-1}(x)$ denotes the inverse of $F(e)$.

For the following numerical simulation a stochastic description of the initial void ratio with respect to a initial mean void ratio of $e_{m0} = 0.6$ and a standard deviation of 1.3% is assumed. The distribution of the initial void ratio varies between $e_0 = 0.5812 - 0.6205$ as shown in Fig. 4.39. In the following the results obtained for the initially homogeneous void ratio are compared with that of the initially heterogeneous for both the frictionless interface and the interlocked interface.

For the frictionless interface Fig. 4.40 and Fig. 4.41 show the contour plots of the void ratio e and the norm of the deviatoric strain rate $\|\dot{\boldsymbol{\varepsilon}}^d\|$ of granular soil after the vertical displacements of $u_2 = 0.2$, 0.5 and 1.9 cm, respectively. From Fig. 4.40 zig-zag patterns of the shear band can be observed after the vertical displacement of $u_2 = 0.5$ cm for the initially heterogeneous void ratio. For the initially homogeneous void ratio, shear bands are observed for longer compression. Furthermore, for $u_2 = 1.9$ cm only one pattern of the shear band is pronounced for the initially heterogeneous void ratio while additional 'smeared' shear band patterns are observed for the initially homogeneous void ratio (Fig. 4.40). However, the contour plot for $\|\dot{\boldsymbol{\varepsilon}}^d\|$ shows that the pattern of the shear band for the case of initially heterogeneous void ratio is similar to that obtained for the initially homogeneous void ratio (Fig. 4.41).

For the case of interlocked interface, it can clearly be seen that neither initially homogeneous void ratio nor initially heterogeneous void ratio shows a localization in the granular soil. Moreover, both, the initially homogeneous void ratio and the initially heterogeneous void ratio show

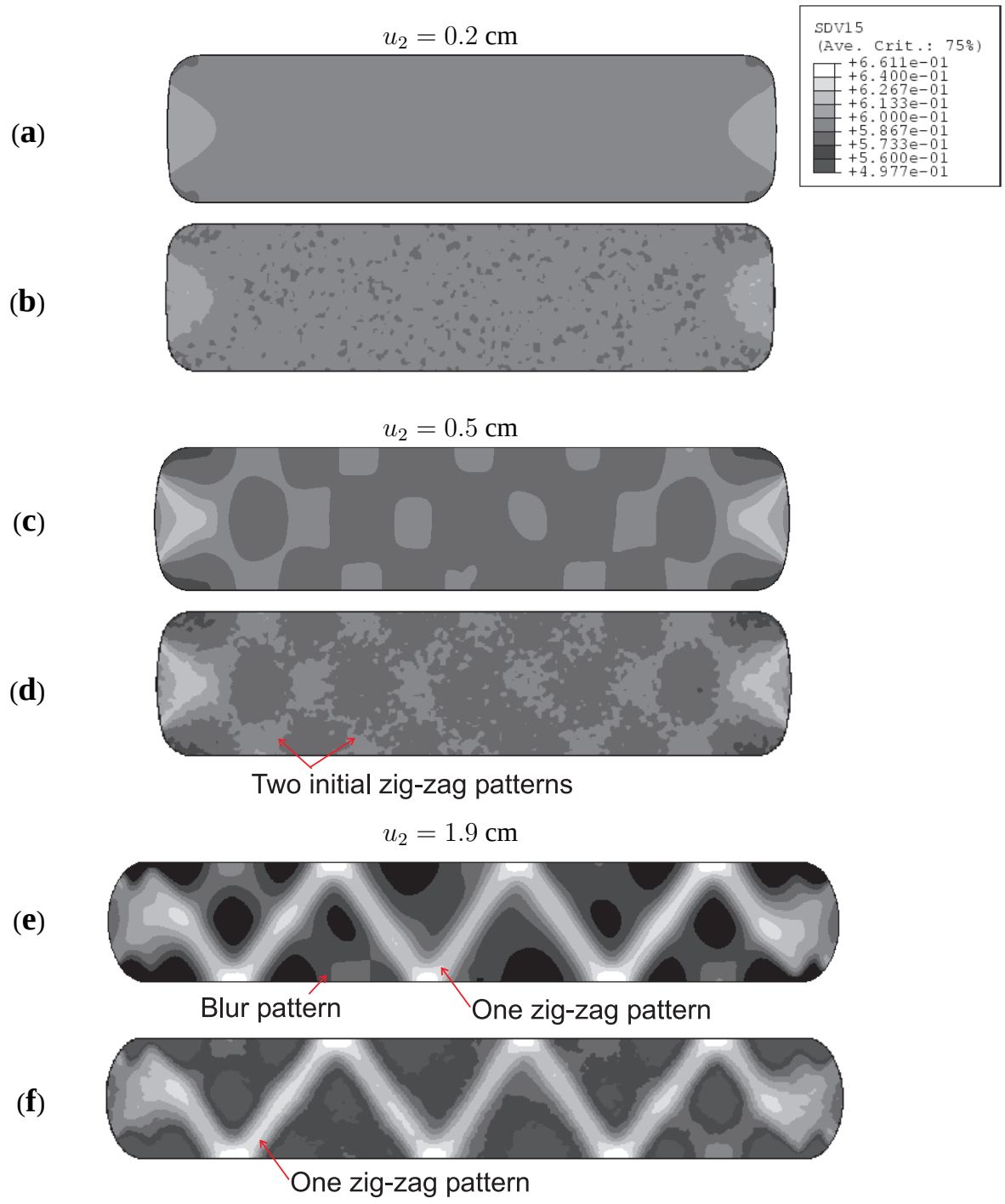

Figure 4.40: Frictionless interface: contour plot of the void ratio e resulting from (**a**, **c**, **e**) the initially homogeneous void ratio, (**b**, **d**, **f**) the initially heterogeneous void ratio for different vertical displacements u_2.

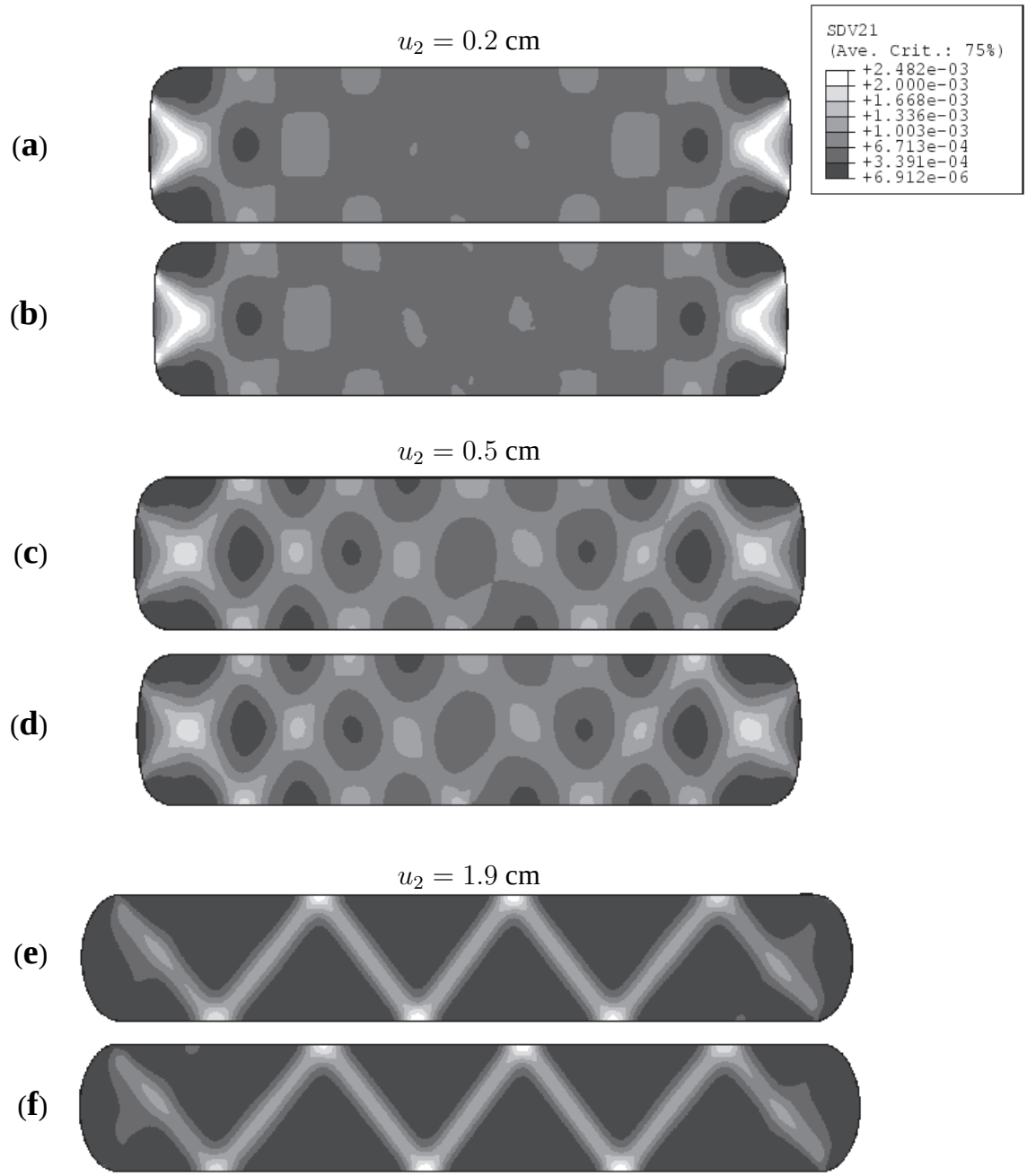

Figure 4.41: Frictionless interface: contour plot of the norm of the deviatoric strain rate $\|\dot{\varepsilon}^d\|$ resulting from (**a**, **c**, **e**) the initially homogeneous void ratio, (**b**, **d**, **f**) the initially heterogeneous void ratio for different vertical displacements u_2.

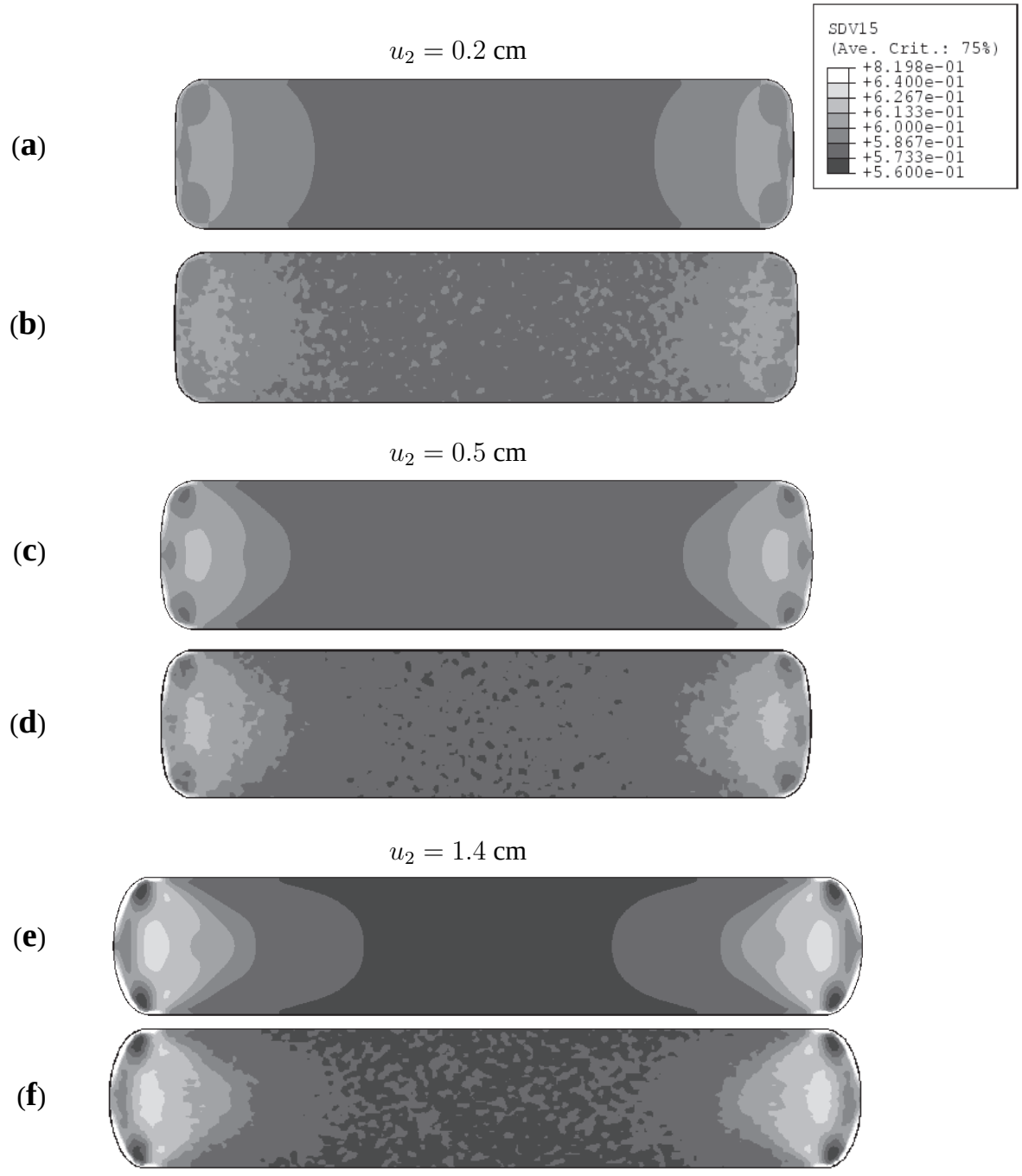

Figure 4.42: Interlocked interface: contour plot of the void ratio e resulting from (**a**, **c**, **e**) the initially homogeneous void ratio, (**b**, **d**, **f**) the initially heterogeneous void ratio for different vertical displacements u_2.

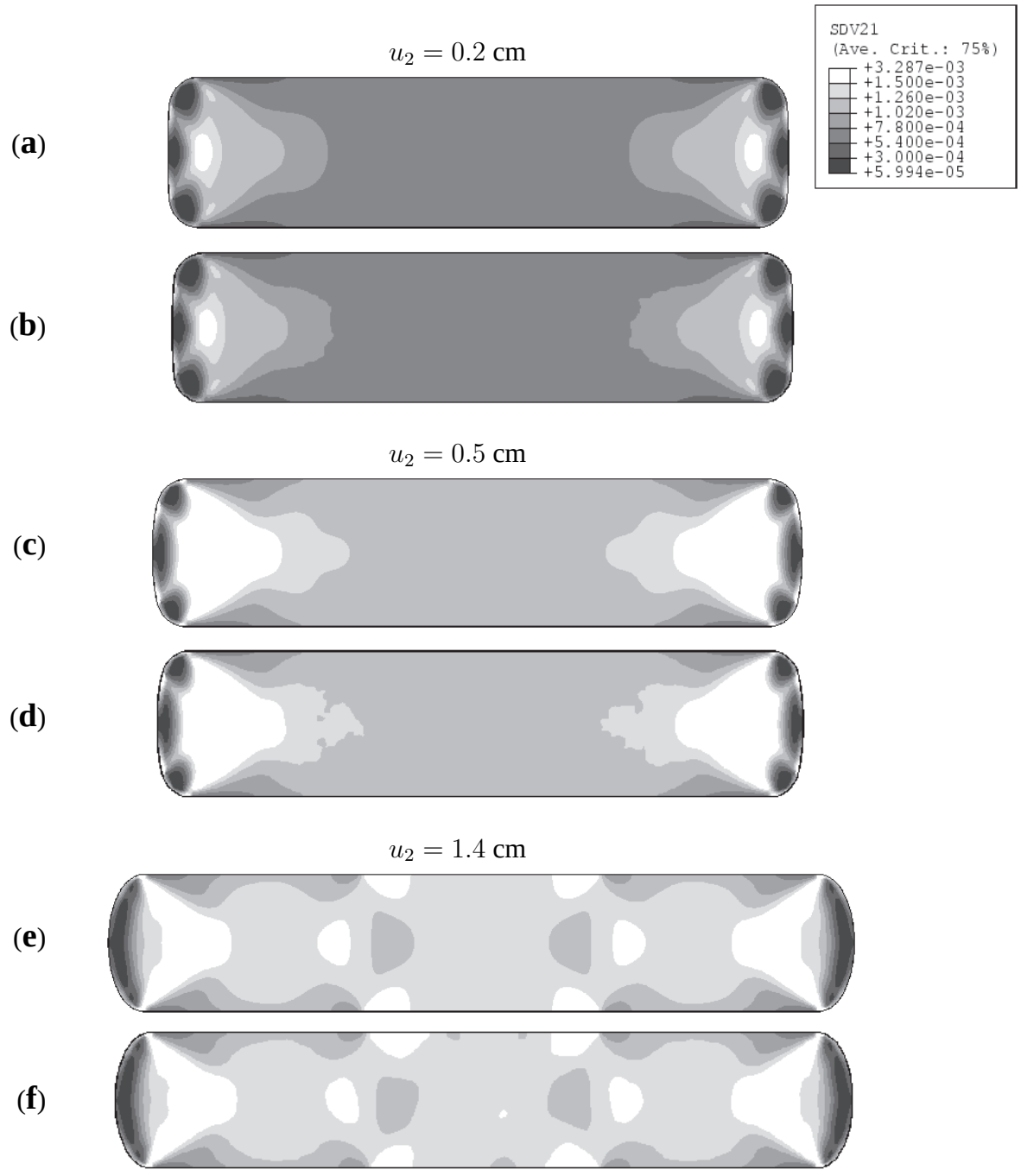

Figure 4.43: Interlocked interface: contour plot of the norm of the deviatoric strain rate $\|\dot{\varepsilon}^d\|$ resulting from (**a**, **c**, **e**) the initially homogeneous void ratio, (**b**, **d**, **f**) the initially heterogeneous void ratio for different vertical displacements u_2.

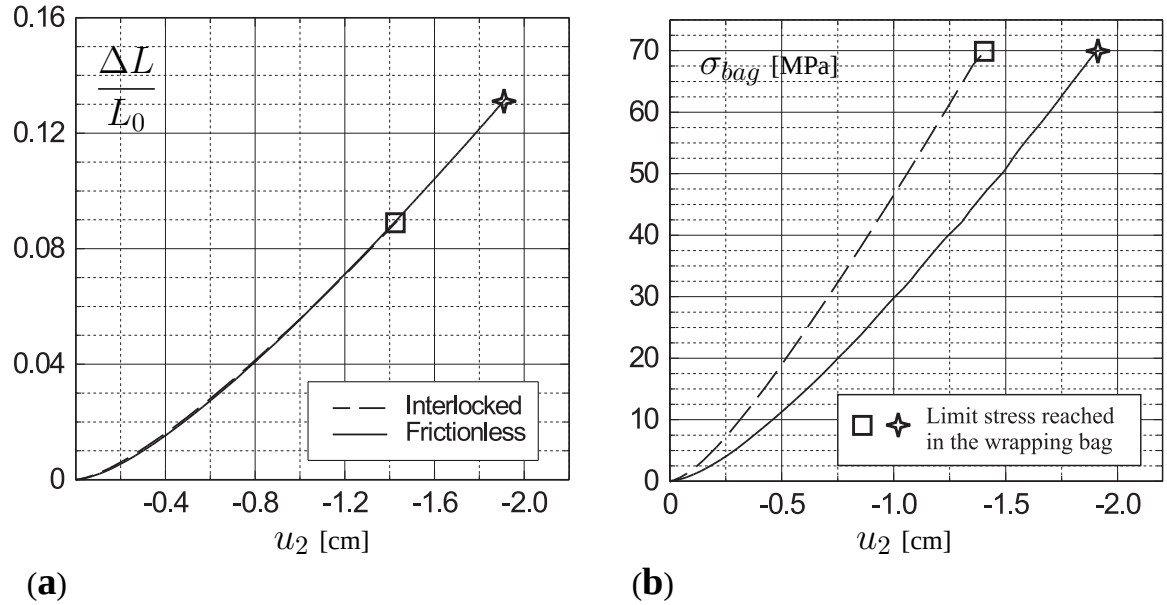

Figure 4.44: Comparison between the frictionless interface and the interlocked interface for the evolution of (**a**) $\Delta L/L_0$, (**b**) σ_{bag} at Bag.0.

similar distribution for the void ratio e (Fig. 4.42) and for the deviatoric strain rate $\|\dot{\varepsilon}^d\|$ (Fig. 4.43).

4.2.5 Interpretation of the numerical results

In the following the numerical results obtained for the frictionless interface is compared with the interlocked interface for the vertical displacement of $u_2 = 0.2$ cm and 0.5 cm and for the state when the bag reaches the limit stress $\sigma_{bag} = \sigma_{limit}$, i.e. $u_2 = 1.9$ cm for the frictionless interface and $u_2 = 1.4$ cm for the interlocked interface.

While the change of the perimeter ΔL with u_2 is almost independent of the assumed interface behavior (Fig. 4.44(a)), the evolution of the tensile stress is not (Fig. 4.44(b)). In particular, for the interlocked interface, the limit stress σ_{limit} in the wrapping material is already reached for a lower vertical displacement than that for the frictionless interface. Moreover, Fig. 4.45 shows that in contrast to the frictionless interface, the distribution of the tensile stress in the wrapping material along the circumference of the soilbag is not uniform for the case of the interlocked interface. The limit stress is first reached at the middle part of the soilbag. Fig. 4.46(a) shows that for both, the frictionless interface and the interlocked interface, $\Delta V/V_0$ is less than 1%. The mean vertical stress p_v for the interlocked interface is higher than that for the frictionless interface(Figs. 4.46(b)).

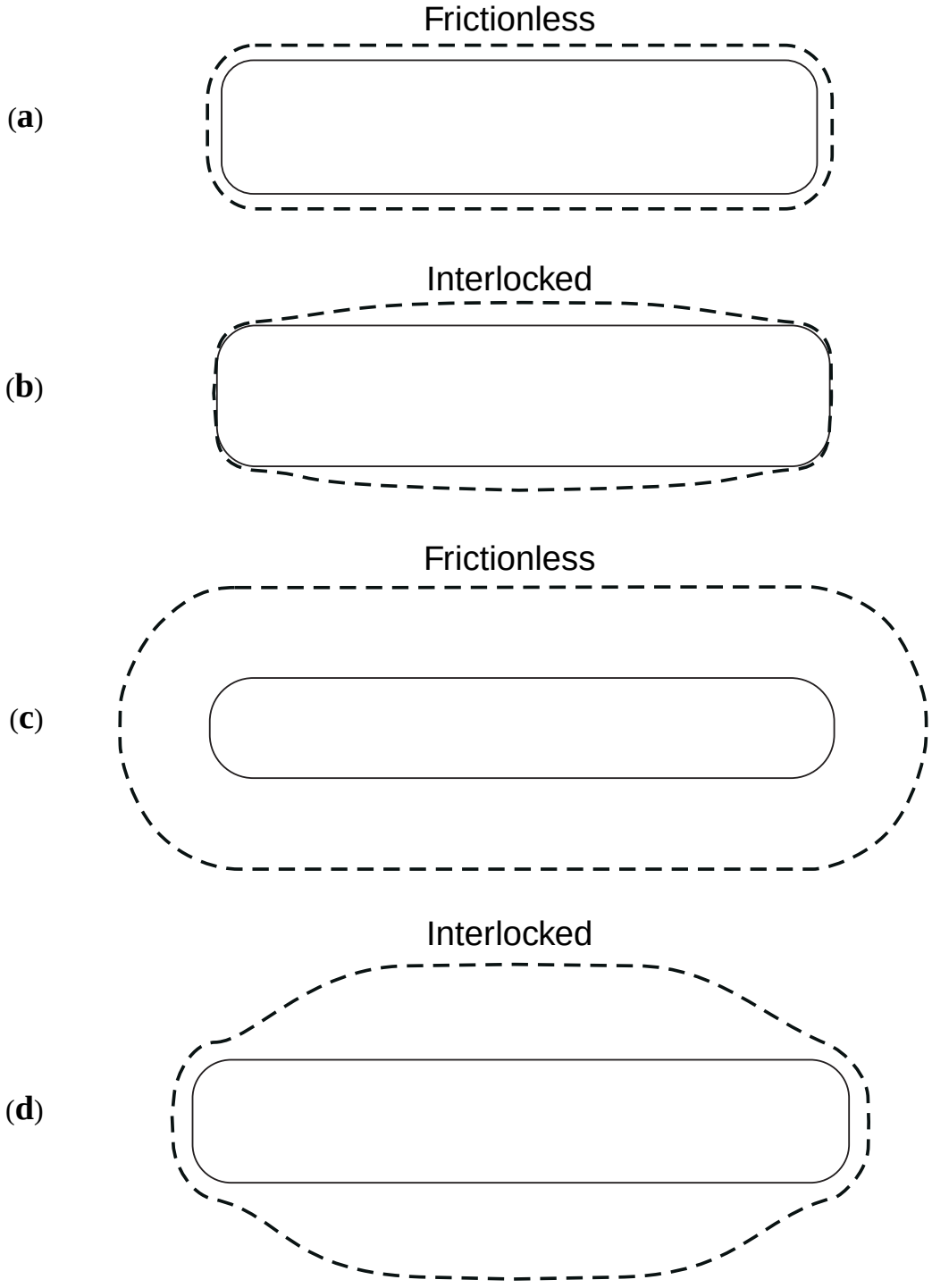

Figure 4.45: Comparison between the frictionless interface and the interlocked interface for the contour plot of the tensile stress in the wrapping material at (**a**, **b**) the vertical displacement of $u_2 = 0.5$ cm, (**c**, **d**) the state when $\sigma_{bag} = \sigma_{limit}$.

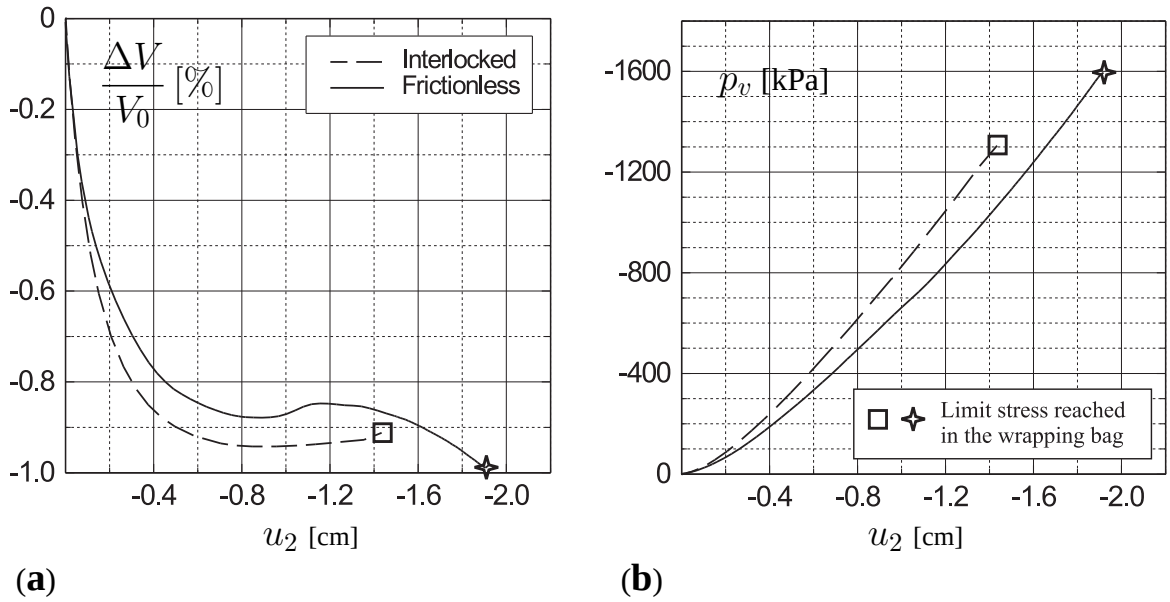

Figure 4.46: Comparison between the frictionless interface and the interlocked interface for the evolution of (**a**) $\Delta V/V_0$, (**b**) p_v.

For the small vertical displacement the distribution of the void ratio for the interlocked interface is more homogeneous than that for frictionless interface (Fig. 4.47(a)). Furthermore, when the wrapping material reaches the limit stress, higher values of the void ratio are concentrated in a zig-zag pattern for the case of frictionless interface (Fig. 4.47(b)). For the interlocked interface, mainly the granular soil at the left and right sides of the soilbag experience dilatancy. With an inhomogeneous distribution of the void ratio the onset of the shear band is more pronounced for the case of frictionless interface, as outlined in Section 4.2.4.

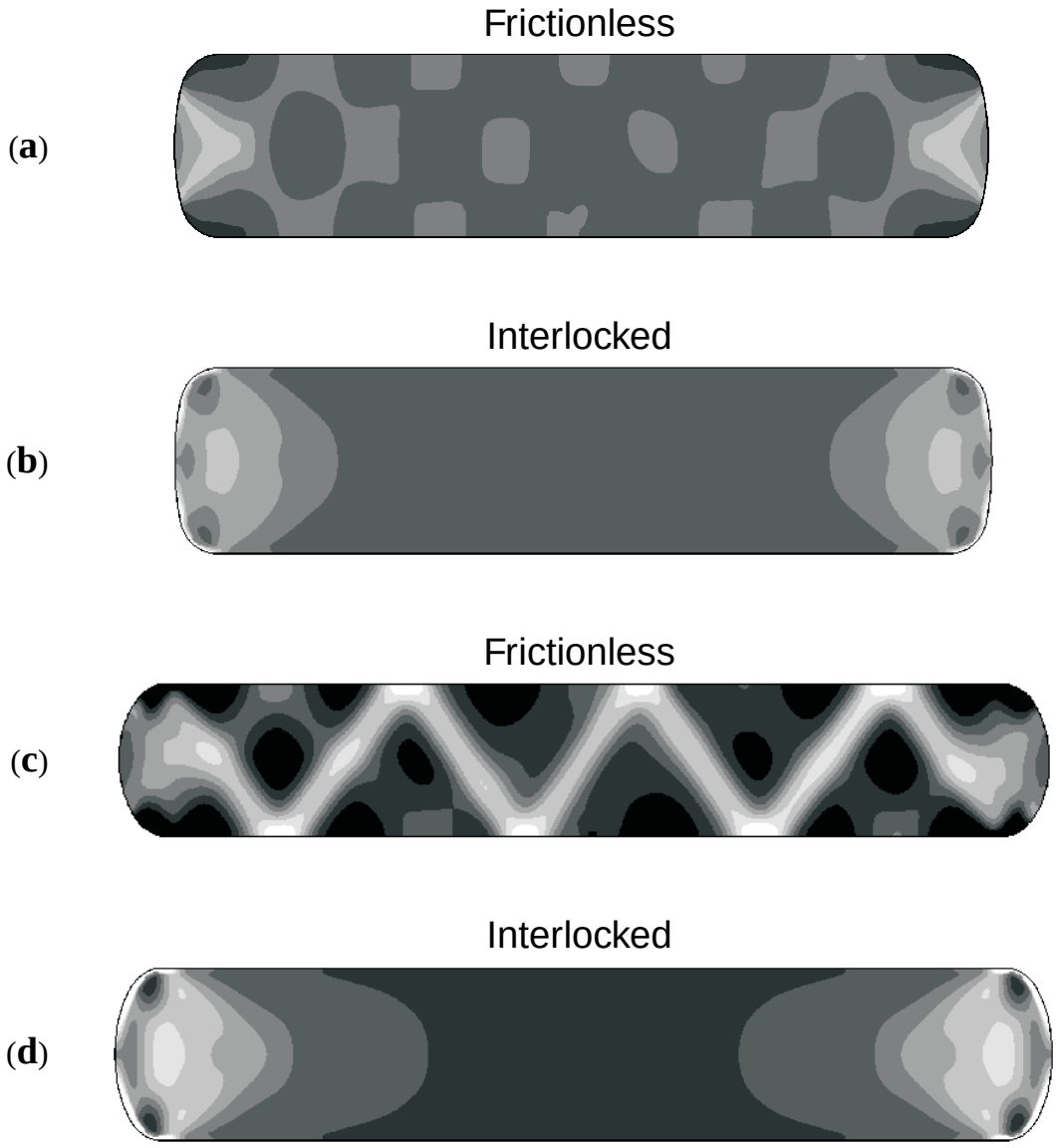

Figure 4.47: Comparison between the frictionless interface and the interlocked interface for the contour plot of the void ratio e at (**a**, **b**) the vertical displacement of $u_2 = 0.5$ cm, (**c**, **d**) the state when $\sigma_{bag} = \sigma_{limit}$.

5 CONCLUSIONS

Analytical and numerical investigations on the mechanical behavior of a soilbag under vertical compression and plane strain condition have been conducted. Particular attention is paid to the influence of the interface behavior between the granular soil and the wrapping bag on the stress-strain behavior of the soilbag structure. Two different interface behaviors are investigated: a frictionless interface (no slide and rotation resistance along the interface) and an interlocked interface (motion of the soil particles at the interface coincides with the motion of the bag). For the analytical study several simplifications are made, e.g. the granular material inside the soilbag is assumed to be in the limit state and the contact between the soil and the bag is frictionless. In order to evaluate the simplified analytical model numerical simulations with a more sophisticated description for the soil behavior and the interface are carried out. Furthermore, the soil behavior close to the interface is separately studied for the case of shearing of an infinite granular soil strip under constant vertical pressure. In this study, the attention is paid to the influences of the initial density of the granular soil, the mean grains size and the rotation resistance of the particles at the interface on the evolution of the mobilized friction angle and the occurrence of strain localization in form of shear bands.

In particular, for the soil behavior closed to the interface under shearing the following results are obtained:

- Shear strain localization takes place from the beginning of shearing where the location and the thickness of shear band strongly depends on the prescribed boundary conditions, the mean grain size, the initial void ratio and the vertical pressure. The results are in agreement with the numerical simulations of other authors.

- For a lower rotation resistance at the interface the shear band is located closer to the surface of the bounding structure.

- The predicted thickness of the shear band is higher for an initially looser material, a higher vertical pressure, a larger mean grain size and for a higher rotation resistance of the soil grains along the interface area. The results are in agreement with the numerical simulation other authors.

- In accordance with experimental observations the peak value of the mobilized friction angle is higher for initially dense granular soil. With advanced shearing the mobilized friction angle decreases and it tends towards a stationary value which is close to the critical friction angle of the granular soil. The deviation from the critical friction angle de-

pends on the specific formulation of the constitutive model, i.e. on the described coupling between the stress and the couple stress at stationary state.

- For the case of a fluctuation of the Cosserat rotation at the interface the mobilized friction angle also varies. However, the mean value is almost equal to the critical friction angle of the granular soil.

For the vertically compressed soilbag under plane strain condition, the following results are obtained:

(a) for the simplified analytical models

  – The tensile stress in the wrapping material and the vertical pressure on the top of the soilbag are a function of the prescribed vertical displacement, the initial width-to-height ratio, the elasto-plastic properties of the wrapping material and the limit stress ratio of the filling material.
  – With the increase of the prescribed vertical displacement the perimeter of the soilbag, the tensile stress in the wrapping material, and the mean vertical pressure on the top of the soilbag nonlinearly increase.
  – The tensile stress in the wrapping material reaches the limit tensile stress earlier for a higher initial width-to-height ratio of the soilbag. The vertical pressure on the top of the soilbag is also higher for higher initial width-to-height ratio.
  – While for the model by Matsuoka & Liu only the global equilibrium in the section of the soilbag is fulfilled, also the local equilibrium is fulfilled in the proposed extended model.

(b) for the numerical model with frictionless interface between the granular soil and the wrapping bag

  – The tensile stress in the wrapping material uniformly increases while the stress ratio of the granular soil inside the bag inhomogeneously develops.
  – Dilatancy of the granular soil firstly appears at the side parts of the soilbag.
  – The pattern of zones with intense shear strain which is reflected by the soilbag boundaries can be detected with the advance of the compression.
  – With an inhomogeneous distribution of the initial void ratio, the onset of the strain localization in the granular body appears for a lower vertical compression.

(c) for the numerical model with interlocked interface between the granular soil and the wrapping bag

  – The distribution of the tensile stress in the wrapping membrane is not uniform as it is for the frictionless interface. The tensile stress in the wrapping material is higher in the middle of the soilbag than at the sides of the soilbag.

- The filling material in the middle of the soilbag mainly experiences compression. Dilatancy occurs at the sides of the soilbag.
- No significant strain localization is observed up to the limit stress reached in the wrapping material.
- The mean vertical pressure on the top of the soilbag is higher than that obtained with the frictionless interface.

(d) for the comparison between the analytical and numerical model with the frictionless interface

- The tensile stress in the wrapping material obtained from the analytical model is slightly higher than that from the numerical one.
- The mean vertical pressure on the top of the soilbag shows a rather good agreement.

In general it can be concluded that the soilbag can resist high compression provided that the volume change of the granular body is small. The vertical load capacity depends on the type of wrapping material, the critical friction angle of granular material and the interface properties between the filling material and the wrapping bag. With the simplified analytical model the vertical pressure on the top of the soilbag can be well predicted as far as the assumed critical friction angle of the filling material is closed to the real value and the interface is frictionless. With an increase of the interface friction between the granular soil and the wrapping bag, the vertical pressure increases for the same vertical compression. However, the vertical load capacity is smaller if friction between the soil and the wrapping material appears. This is because the limit stress in the wrapping material is reached for a lower vertical compression. Finally, it should be noted that the present conclusions are only related to the case of a vertical compression of the soilbag. Thus, more general load conditions including shear loads applied on the top of the soilbags need additional investigations.

A SYMBOLS

Throughout this thesis, symbolic notations are used for vectors and tensors with bold lower and bold upper case letters, respectively. For vector and tensor components, indical notation with respect to a rectangular Cartesian basis e_i ($i = 1, 2, 3$). Herein, the summation convention over repeated indices is used. Operations are defined as:

$$
\begin{aligned}
\mathbf{a} \cdot \mathbf{b} &= a_i\, b_i, \\
\mathbf{a} \otimes \mathbf{b} &= a_i\, b_j\, \mathbf{e}_i \otimes \mathbf{e}_j, \\
\mathbf{A}\, \mathbf{b} &= A_{ij}\, b_j\, \mathbf{e}_i, \\
\mathbf{A}\, \mathbf{B} &= A_{ik}\, B_{kj}\, \mathbf{e}_i \otimes \mathbf{e}_j, \\
\mathbf{A} : \mathbf{B} &= A_{ij}\, B_{ij}, \\
\mathcal{C} : \mathbf{B} &= C_{ijkl}\, B_{kl}\, \mathbf{e}_i \otimes \mathbf{e}_j, \\
\mathrm{grad}(\mathbf{a}) &= \frac{\partial \mathbf{a}}{\partial \mathbf{x}}, \\
\mathrm{div}(\mathbf{a}) &= \mathrm{grad}(\mathbf{a}) \cdot \mathbf{I}, \\
\|\mathbf{a}\| &= \sqrt{\mathbf{a} \,.\, \mathbf{a}} = \sqrt{a_i\, a_i}, \\
\|\mathbf{A}\| &= \sqrt{\mathbf{A} \,:\, \mathbf{A}} = \sqrt{A_{ij}\, A_{ij}}
\end{aligned}
$$

All notations and symbols are defined where they first appear in the text. For easy reference, the most frequently used symbols and their meaning are presented here.

$\mathbf{e}_i$: base vector

$\boldsymbol{\epsilon}$: permutation tensor

$\mathbf{I}$: second order unit tensor

δ_{ij} : Kronecker delta

$\mathbf{x}$: position vector in the current configuration

$\mathbf{X}$: position vector in the reference configuration

$\mathbf{u}$: displacement vector

$\dot{\mathbf{u}}$: velocity vector

$\mathbf{F}$: deformation gradient

$\mathbf{L}$: velocity gradient

$\dot{\boldsymbol{\varepsilon}}$: symmetric part of velocity gradient

$\mathbf{W}$: macro-spin tensor, the skew symmetric part of velocity gradient

$\boldsymbol{\omega}$: macro rotation vector

$\dot{\boldsymbol{\omega}}$: rate of the macro rotation vector

$\bar{\boldsymbol{\Omega}}$: micro-polar gyration tensor

$\boldsymbol{\omega}^c$: Cosserat rotation vector

$\dot{\boldsymbol{\omega}}^c$: rate of the Cosserat rotation vector

$\dot{\boldsymbol{\varepsilon}}^c$: Cosserat strain rate tensor

$\dot{\varepsilon}^c_{kk}$: volumetric strain rate

$\dot{\boldsymbol{\varepsilon}}^d$: deviatoric part of strain rate tensor,

$\dot{\boldsymbol{\kappa}}$: rate of curvature

$\boldsymbol{\sigma}$: Cauchy stress tensor

$\mathbf{t}$: surface traction vector

$\dot{\boldsymbol{\sigma}}$: time derivative of the stress tensor

$\mathring{\boldsymbol{\sigma}}$: objective stress rate tensor

$\boldsymbol{\mu}$: couple stress tensor

$\mathbf{m}$: surface couple vector

$\dot{\boldsymbol{\mu}}$: time derivative of the couple stress tensor

$\mathring{\boldsymbol{\mu}}$: objective couple stress rate tensor

e : current void ratio

$\dot{e}$: rate of void ratio

e_i : maximum void ratio, at which the grains are still in contact

e_{i0} : maximum void ratio at nearly stress free state

e_c : critical void ratio

e_{c0} : critical void ratio at nearly stress free state

e_d : minimum void ratio

e_{d0} : minimum void ratio at nearly stress free state

α : positive hypoplastic constitutive constant

β : hypoplastic constitutive constant, $\beta > 1$

n : hypoplastic constitutive constant

h_s : hypoplastic constitutive constant

d_{50} : mean grain diameter

φ_c : critical friction angle

φ_m : mobilized friction angle

K : stress ratio in the granular material inside the soilbag

p_v : mean value of resulting vertical pressure on top of a soilbag

T : tensile force in the wrapping material

σ_{bag} : tensile stress in the wrapping material

σ_{bag}^{limit} : limit tensile stress in the wrapping material

E : elastic modulus of the wrapping material

B_0, H_0 : initial width and initial height of the soilbag

B, H : current width and current height of the soilbag

L_0, L : initial and current perimeter of the soilbag

V_0, V_0 : initial and current volume of the soilbag

B MICRO-POLAR HYPOPLASTIC MODELING OF STATIONARY STATES

Concerning stationary states the following four different versions of polar hypoplastic constitutive models are discussed:

- Version A (Tejchman & Gudehus, 2001 [114]; Tejchman, 2004 [110]; Tejchman & Bauer, 2005 [113]):

$$\mathring{\sigma}_{ij} = f_s \left[\hat{a}^2 \, \dot{\varepsilon}^c_{ij} + (\hat{\sigma}_{kl} \dot{\varepsilon}^c_{kl} + \hat{\mu}_{kl} \dot{\kappa}^*_{kl}) \, \hat{\sigma}_{ij} + f_d \, \hat{a} \, \left(\hat{\sigma}_{ij} + \hat{\sigma}^d_{ij} \right) \sqrt{\|\dot{\varepsilon}^c_{kl}\|^2 + \|\dot{\kappa}^*_{kl}\|^2} \right], \tag{B.1}$$

$$\mathring{\mu}_{ij} = d_{50} f_s \left[\hat{a}^2 \, \dot{\kappa}^*_{ij} + (\hat{\sigma}_{kl} \dot{\varepsilon}^c_{kl} + \hat{\mu}_{kl} \dot{\kappa}^*_{kl}) \, \hat{a}^2 \, \hat{\mu}_{ij} + f_d \, \hat{a}^2 \, a_m \, \hat{\mu}_{ij} \sqrt{\|\dot{\varepsilon}^c_{kl}\|^2 + \|\dot{\kappa}^*_{kl}\|^2} \right], \tag{B.2}$$

with

$$\hat{a}^{-1} = c_1 + c_2 \sqrt{\hat{\sigma}^d_{kl} \, \hat{\sigma}^d_{kl}} \, [1 + \cos(3\theta)] \quad , \quad \cos(3\theta) = -\sqrt{6} \frac{\hat{\sigma}^d_{kl} \hat{\sigma}^d_{lm} \hat{\sigma}^d_{mk}}{(\hat{\sigma}^d_{pq} \, \hat{\sigma}^d_{pq})^{3/2}},$$

$$c_1 = \sqrt{\frac{3}{8}} \frac{(3 - \sin\varphi_c)}{\sin\varphi_c} \quad , \quad c_2 = \frac{3}{8} \frac{(3 + \sin\varphi_c)}{\sin\varphi_c}.$$

- Version B (Huang et al., 2002 [63]):

$$\mathring{\sigma}_{ij} = f_s \left[\hat{a}^2 \, \dot{\varepsilon}^c_{ij} + (\hat{\sigma}_{kl} \dot{\varepsilon}^c_{kl} + \hat{\mu}_{3l} \dot{\kappa}^*_{kl}) \, \hat{\sigma}_{ij} + f_d \left(\hat{\sigma}_{ij} + \hat{\sigma}^d_{ij} \right) \sqrt{\hat{a}^2 \|\dot{\varepsilon}^c_{kl}\|^2 + a_m^2 \|\dot{\kappa}^*_{kl}\|^2} \right], \tag{B.3}$$

$$\mathring{\mu}_{ij} = d_{50} \, f_s \left[a_m^2 \, \dot{\kappa}^*_{ij} + (\hat{\sigma}_{kl} \dot{\varepsilon}^c_{kl} + \hat{\mu}_{kl} \dot{\kappa}^*_{kl}) \, \hat{\mu}_{ij} + f_d \, 2 \, \hat{\mu}_{ij} \sqrt{\hat{a}^2 \|\dot{\varepsilon}^c_{kl}\|^2 + a_m^2 \|\dot{\kappa}^*_{kl}\|^2} \right], \tag{B.4}$$

with

$$\hat{a} = \frac{\sin\varphi_c}{3 - \sin\varphi_c} \left[\sqrt{\frac{8/3 - 3c + \sqrt{3/2} \, c^{3/2} \cos(3\theta)}{1 + \sqrt{3/2} \, c^{1/2} \cos(3\theta)}} - \sqrt{c} \right] \quad , \quad c = \hat{\sigma}^{sd}_{pq} \, \hat{\sigma}^{sd}_{pq},$$

$$\cos(3\theta) = -\sqrt{6} \frac{\hat{\sigma}^{sd}_{kl} \hat{\sigma}^{sd}_{lm} \hat{\sigma}^{sd}_{mk}}{c^{3/2}} \quad , \quad \hat{\sigma}^{sd}_{kl} = \frac{(\hat{\sigma}^d_{kl} + \hat{\sigma}^d_{kl})}{2}.$$

- Version C (Bauer & Huang, 1999 [11]; Huang & Bauer, 2003 [61]):

$$\mathring{\sigma}_{ij} = f_s \left[\hat{a}^2 \, \dot{\varepsilon}^c_{ij} + (\hat{\sigma}_{kl}\dot{\varepsilon}^c_{kl} + \hat{\mu}_{kl}\dot{\kappa}^*_{kl}) \, \hat{\sigma}_{ij} + f_d \, \hat{a} \, \left(\hat{\sigma}_{ij} + \hat{\sigma}^d_{ij}\right) \sqrt{\|\dot{\varepsilon}^c_{kl}\|^2 + \|\dot{\kappa}^*_{kl}\|^2} \right], \tag{B.5}$$

$$\mathring{\mu}_{ij} = d_{50} f_s \left[a_m^2 \, \dot{\kappa}^*_{ij} + (\hat{\sigma}_{kl}\dot{\varepsilon}^c_{kl} + \hat{\mu}_{kl}\dot{\kappa}^*_{kl}) \; \hat{\mu}_{ij} + f_d \, 2 \, a_m \hat{\mu}_{ij} \sqrt{\|\dot{\varepsilon}^c_{kl}\|^2 + \|\dot{\kappa}^*_{kl}\|^2} \right], \tag{B.6}$$

with

$$\hat{a} = \frac{\sin\varphi_c}{3 - \sin\varphi_c} \left[\sqrt{\frac{8/3 - 3c + \sqrt{3/2}\, c^{3/2}\cos(3\theta)}{1 + \sqrt{3/2}\, c^{1/2}\cos(3\theta)}} - \sqrt{c} \right] \quad , \quad c = \hat{\sigma}^{sd}_{pq}\, \hat{\sigma}^{sd}_{pq},$$

$$\cos(3\theta) = -\sqrt{6}\frac{\hat{\sigma}^{sd}_{kl}\hat{\sigma}^{sd}_{lm}\hat{\sigma}^{sd}_{mk}}{c^{3/2}} \qquad , \quad \hat{\sigma}^{sd}_{kl} = \frac{(\hat{\sigma}^d_{kl} + \hat{\sigma}^d_{kl})}{2}.$$

- Version D (Bauer, 2005 [8]):

$$\mathring{\sigma}_{ij} = f_s \left[\hat{a}^2 \, \dot{\varepsilon}^c_{ij} \; + \; (\hat{\sigma}_{kl}\dot{\varepsilon}^c_{kl}) \, \hat{\sigma}_{ij} \; + \; f_d \, \hat{a} \; \left(\hat{\sigma}_{ij} + \hat{\sigma}^d_{ij}\right) \|\dot{\varepsilon}^c_{kl}\| \right], \tag{B.7}$$

$$\mathring{\mu}_{ij} = d_{50} \, f_s \left[a_m^2 \, \dot{\kappa}^*_{ij} \; + \; (\hat{\mu}_{kl}\dot{\kappa}^*_{kl}) \; \hat{\mu}_{ij} \; + \; f_d \, 2 \, a_m \hat{\mu}_{ij} \, \|\dot{\kappa}^*_{kl}\| \right], \tag{B.8}$$

with

$$\hat{a} = \sqrt{\frac{8\sin^2\varphi_c}{9(3 + \sin^2\varphi_c)}}.$$

A stationary states is defined as a state in which there is no changes of σ_{ij}, μ_{ij} and e for a constant rate of deformation $\dot{\varepsilon}^c_{ij}$ and or a constant rate of curvature $\dot{\kappa}^*_{ij}$, i.e.

$$\mathring{\sigma}_{ij} = 0 \quad \wedge \quad \mathring{\mu}_{ij} = 0 \quad \wedge \quad \dot{e} = 0. \tag{B.9}$$

With the assumption of incompressible grains, the requirement $\dot{e} = 0$ is equivalent to the vanishing of the volumetric strain, i.e. $\dot{\varepsilon}^c_{kk} = 0$. Thereby, the following relations at the stationary state can be drawn

$$\dot{\varepsilon}^c_{kk} = 0, \qquad \dot{\varepsilon}^{cd}_{ij} = \dot{\varepsilon}^c_{ij}.$$

Applying the criterion for stationary states, i.e. Eq. B.9, to the evolution equations of the stress and the couple stress leads to the following relations for the normalized deviatoric stress $\hat{\sigma}^d_{ij}$ and the normalized couple stress $\hat{\mu}_{ij}$:

- Version A

$$\hat{\sigma}^d_{ij} \;=\; \frac{-\hat{a}\,\dot{\varepsilon}^c_{ij}}{f_d\,\sqrt{\|\dot{\varepsilon}^c_{kl}\|^2+\|\dot{\kappa}^*_{kl}\|^2}}\,, \qquad \hat{\mu}_{ij} \;=\; \frac{-\dot{\kappa}^*_{ij}}{(a_m-\hat{a})\;f_d\,\sqrt{\|\dot{\varepsilon}^c_{kl}\|^2+\|\dot{\kappa}^*_{kl}\|^2}}\,, \tag{B.10}$$

and

$$\left(\frac{\|\hat{\sigma}^d_{ij}\|}{\hat{a}}\right)^2+\left(\frac{\|\hat{\mu}_{ij}\|}{\lambda a_c}\right)^2 \;=\; 1\,, \qquad \lambda=\frac{1}{a_m\,(a_m-\hat{a})}\,, \tag{B.11}$$

with:

$$f_d \;=\; \sqrt{\frac{\|\dot{\varepsilon}^c_{kl}\|^2+\lambda\,\|\dot{\kappa}^*_{kl}\|^2}{\|\dot{\varepsilon}^c_{kl}\|^2+\|\dot{\kappa}^*_{kl}\|^2}}\,, \qquad \lambda \;=\; \frac{1}{\hat{a}\,(a_m-\hat{a})}. \tag{B.12}$$

- Version B

$$\hat{\sigma}^d_{ij} \;=\; \frac{-\hat{a}^2\,\dot{\varepsilon}^c_{ij}}{f_d\,\sqrt{\hat{a}^2\|\dot{\varepsilon}^c_{kl}\|^2+a_m^2\|\dot{\kappa}^*_{kl}\|^2}}\,, \qquad \hat{\mu}_{ij} \;=\; \frac{-a_m^2\,\dot{\kappa}^*_{ij}}{f_d\,\sqrt{\hat{a}^2\|\dot{\varepsilon}^c_{kl}\|^2+a_m^2\|\dot{\kappa}^*_{kl}\|^2}}\,, \tag{B.13}$$

and

$$\left(\frac{\|\hat{\sigma}^d_{ij}\|}{\hat{a}}\right)^2+\left(\frac{\|\hat{\mu}_{ij}\|}{a_m}\right)^2 \;=\; 1\,, \tag{B.14}$$

with:

$$f_d \;=\; \sqrt{\frac{\hat{a}^2\|\dot{\varepsilon}^c_{kl}\|^2+a_m^2\,\|\dot{\kappa}^*_{kl}\|^2}{\hat{a}^2\|\dot{\varepsilon}^c_{kl}\|^2+a_m^2\|\dot{\kappa}^*_{kl}\|^2}} \;=\; 1. \tag{B.15}$$

- Version C

$$\hat{\sigma}^d_{ij} \;=\; \frac{-\hat{a}\,\dot{\varepsilon}^c_{ij}}{f_d\,\sqrt{\|\dot{\varepsilon}^c_{kl}\|^2+\|\dot{\kappa}^*_{kl}\|^2}}\,, \qquad \hat{\mu}_{ij} \;=\; \frac{-a_m^2\,\dot{\kappa}^*_{ij}}{(2a_m-\hat{a})\;f_d\,\sqrt{\|\dot{\varepsilon}^c_{kl}\|^2+\|\dot{\kappa}^*_{kl}\|^2}}\,, \tag{B.16}$$

and

$$\left(\frac{\|\hat{\sigma}^d_{ij}\|}{\hat{a}}\right)^2+\left(\frac{\|\hat{\mu}_{ij}\|}{\lambda a_m}\right)^2 \;=\; 1\,, \qquad \lambda=\frac{a_m}{2a_m-\hat{a}}\,, \tag{B.17}$$

with:

$$f_d \;=\; \sqrt{\frac{\|\dot{\varepsilon}^c_{kl}\|^2+\lambda\,\|\dot{\kappa}^*_{kl}\|^2}{\|\dot{\varepsilon}^c_{kl}\|^2+\|\dot{\kappa}^*_{kl}\|^2}}\,, \qquad \lambda \;=\; \frac{a_m}{\hat{a}}\,\frac{a_m}{(2a_m-\hat{a})}. \tag{B.18}$$

- Version D

$$\hat{\sigma}^d_{ij} \;=\; \frac{-\hat{a}\,\dot{\varepsilon}^c_{ij}}{f_d\,\|\dot{\varepsilon}^c_{kl}\|}\,, \qquad \hat{\mu}_{ij} \;=\; \frac{-a_m^2\,\dot{\kappa}^*_{ij}}{\hat{\mu}_{kl}\dot{\kappa}^*_{kl} \;+\; f_d\,2\,a_m\,\|\dot{\kappa}^*_{kl}\|}\,, \tag{B.19}$$

and

$$\|\hat{\sigma}^d_{ij}\| = \hat{a}, \qquad \|\hat{\mu}_{ij}\| = \frac{a_m^2\,\|\dot{\kappa}^*_{kl}\|}{\hat{\mu}_{kl}\dot{\kappa}^*_{kl} \;+\; 2\,a_m\,\|\dot{\kappa}^*_{kl}\|}, \tag{B.20}$$

with:

$$f_d \;=\; \sqrt{\frac{\hat{a}\,\|\dot{\varepsilon}^c_{kl}\|^2}{\hat{a}\,\|\dot{\varepsilon}^c_{kl}\|^2}} \;=\; 1. \tag{B.21}$$

Herein the relations for $\hat{\sigma}^d_{ij}$, $\hat{\mu}_{ij}$ and f_d are derived in a similar way as first shown by Huang et al. (2002) [63]. From Eq. B.11, Eq. B.14 and Eq. B.17, it follows that for stationary states $\|\hat{\sigma}^d_{ij}\|$ and $\|\hat{\mu}_{ij}\|$ are coupled while it is not in Eq. B.20. Furthermore, unlike Version A and Version C, for Version B and Version D factor a_m can be unique related to $\|\hat{\mu}_{ij}\|$ for $\|\hat{\sigma}^d_{ij}\| = 0$. From Eq. B.15 and Eq. B.21, it can be concluded that the density factor f_d generally fulfils the requirement for the void ratio in critical state only for the Version B and the Version D, i.e. for $f_d = 1$ the void ratio e is equal to the critical void ratio e_c according to Eq. 2.40. For these versions, the critical void ratio e_c is reached at stationary state independent of the initial state and the value of a_m. On the other hand, from Eq. B.12 and Eq. B.18 it follows that f_d can be higher than one, thus, the void ratio can also be higher than the critical void ratio. For Version A and Version C, the relation 2.41 between the void ratio in the stationary state and the mean pressure can only be fulfilled for special cases. In particular, one of the following conditions should be fulfilled to obtain $f_d = 1$ at the stationary state:

(i) $\|\dot{\kappa}^*_{ij}\| = 0$,

(ii) $\|\dot{\kappa}^*_{ij}\| \neq 0$ and $\lambda = 1$.

With the condition (i), the parameter a_m has no influence on f_d. Moreover, from Eq. B.10 and Eq. B.16 the couple stress becomes zero and the norm of the normalized deviatoric stress $\|\hat{\sigma}^d_{ij}\| = \hat{a}$. The latter is also obtained for the non-polar version of the hypoplastic model (Bauer, 2000a [6]).

For the condition (ii), one can conclude that for

Version A : $a_m = \hat{a} + 1/\hat{a}$,

Version C : $a_m = \hat{a}$.

It should also be noted that for the condition (ii), coupling between $\hat{\sigma}^d_{ij}$ and $\hat{\mu}_{ij}$ still exist in Version A, Version B and Version C. Therefore, at stationary state, the influence of couple stress may exist, and, consequently, the mobilized friction angle φ_m may deviate from the critical friction angle defined from the limit condition by Matsuoka-Nakai.

C REQUIREMENT FOR THE PROBABILITY DENSITY FUNCTION

In order to proof the requirement 4.41, i.e.

$$\int_{-\infty}^{\infty} f(e)\,de = 1 \tag{C.1}$$

for the chosen density function $f(e)$ in 4.42, i.e.

$$f(e) = \frac{1}{B\,(p,q)\;(b-a)^{p+q-1}}\;(e-a)^{p-1}\,(b-e)^{q-1}\,, \tag{C.2}$$

the integral in Eq.C.1 can be represented as

$$\begin{aligned}
\int_{-\infty}^{\infty} f(e)\,de &= \int_{-\infty}^{a} f(e)\,de + \int_{a}^{b} f(e)\,de + \int_{b}^{\infty} f(e)\,de \\
&= 0 + \int_{a}^{b} f(e)\,de + 0 \\
&= \int_{a}^{b} \frac{1}{B\,(p,q)\;(b-a)^{p+q-1}}\;(e-a)^{p-1}\,(b-e)^{q-1}\;de.
\end{aligned}$$

With the substitution: $u = e - a \rightarrow de = du$, $e = u + a$,

$$\int_{a}^{b} f(e)\,de = \frac{1}{B\,(p,q)} \int_{0}^{b-a} \frac{u^{p-1}(b-u-a)^{q-1}}{(b-a)^{p+q-1}}\,du.$$

With the substitution: $\frac{u}{b-a} = v \rightarrow du = (b-a)dv$,

$$(b-u-a)^{q-1} = \left(1 - \frac{u}{b-a}\right)^{q-1} (b-a)^{q-1},$$

$$\begin{aligned}
\int_a^b f(e)\,de &= \frac{1}{B(p,q)} \int_0^1 \frac{(v(b-a))^{p-1}(1-v)^{q-1}(b-a)^{q-1}(b-a)}{(b-a)^{p+q-1}}\,dv \\
&= \frac{1}{B(p,q)} \int_0^1 v^{p-1}(1-v)^{q-1} \frac{(b-a)^{p-1}(b-a)^{q-1}(b-a)}{(b-a)^{p}\,(b-a)^{q-1}}\,dv \\
&= \frac{1}{B(p,q)} \int_0^1 v^{p-1}(1-v)^{q-1}\,dv.
\end{aligned}$$

According to Eq. 4.44 the integral $\int_0^1 v^{p-1}(1-v)^{q-1}\,dv = B(p,q)$, thus

$$\int_a^b f(e)\,de = \frac{1}{B(p,q)}\,B(p,q) = 1.$$

REFERENCES

[1] K.A. Alshibli and S. Sture. Shear band formation in plane strain experiments of sand. *Journal of Geotechnical and Geoenvironmental Engineering ASCE*, 126(6):495–503, 2000.

[2] U. Aqil, K. Matsushima, Y. Mohri, S. Tamazaki, and F. Tatsuoka. Lateral shearing tests on geosynthetic soilbags. In *Proc. of the 8th International Conference in Geosynthetics*, 1703–1706. Millpress Science Publishers, Rotterdam, Netherlands, 2006.

[3] E. Bauer. Constitutive modeling of critical states in hypoplasticity. In G.N. Pande and S. Pietruszczak, editors, *Proc. of the 5th International Symposium on Numerical Models in Geomechanics*, 15–20. Balkema, Rotterdam, 1995.

[4] E. Bauer. Calibration of a comprehensive hypoplastic model for granular materials. *Soils and Foundations*, 36:13–26, 1996.

[5] E. Bauer. Analysis of shear band bifurcation with a hypoplastic model for a pressure and density sensitive granular material. *Mechanics of Materials*, 31:597–609, 1999.

[6] E. Bauer. Conditions for embedding casagrande's critical states into hypoplasticity. *Mechanics of Cohesive-Frictional Materials*, 5:125–148, 2000.

[7] E. Bauer. Continuum mechanics and theory of materials. Private lecture notes, Graz University of Technology, 2004.

[8] E. Bauer. Initial response of a micro-polar hypoplastic material under plane shearing. *Journal of Engineering Mathematics*, 52:35–51, 2005.

[9] E. Bauer and I. Herle. Stationary states in hypoplasticity. In D. Kolymbas, editor, *Constitutive modeling of granular materials*, 167–192. Springer, 1999.

[10] E. Bauer and W. Huang. The dependence of shear banding on pressure and density in hypoplasticity. In T. Adachi, F. Oka, and A. Yashima, editors, *Proc. of the 4th International Workshop on Localization and Bifurcation Theory for Soils and Rocks*, 81–90. Balkema, Rotterdam, 1997.

[11] E. Bauer and W. Huang. Numerical study of polar effets in shear zones. In G.N. Pande, S. Pietruszczak, and H.F. Schweiger, editors, *Proc. of the 7th International Symposium on Numerical Models in Geomechanics*, 133–138. Balkema, 1999.

[12] E. Bauer and W. Huang. Effect of particle rotations on the interface behavior between a granular layer and parallel rough plates. *Science and Engineering of Composite Materials*, 11:239–246, 2004.

[13] E. Bauer, J. Tejchman, S.F. Tantono, and W. Huang. Micro-polar effects under monotonic and cyclic shearing. In W. Wu and H.S. Yu, editors, *Modern Trends in Geomechanics*, 193–207. Springer, 2006.

[14] E. Bauer and W. Wu. A hypoplastic model for granular soils under cyclic loading. In D. Kolymbas, editor, *Modern Approaches to Plasticity*, 247–258. Elsevier, 1993.

[15] G.E. Bauer and Y.M. Mowafy. The interaction mechanism of granular soils with geogrids. In G. Swoboda, editor, *Proc. of 6th International Conference Numerical Methods in Geomechanics, Innsbruck*, 1263–1272. Balkema, 1988.

[16] Z.P. Bazant and F.-B. Lin. Nonlocal yield limit degradation. *International Journal of Numerical Methods in Engineering*, 26:1805–1823, 1989.

[17] Z.P. Bazant, F.-B. Lin, and G. Pijaudier-Cabot. Yield limit degradation: non-local continuum model with local strain. In E. Onate, D.R.J. Owen, and E. Hinton, editors, *Proc. of International Conference in Computational Plasticity, Barcelona*, 1757–1780, 1987.

[18] Z.P. Bazant and G. Pijaudier-Cabot. Measurement of characteristic length of non-local continuum. *ASCE Journal of Engineering Mechanics*, 115:755–767, 1989.

[19] D.T. Bergado, L.R. Anderson, N. Miura, and A.S. Balasubramaniam. *Soft Ground Improvement*. ASCE, 1996.

[20] D.T. Bergado, S. Youwai, C. Teerawattanasuk, and P. Visudmedanukul. The interaction mechanism and behavior of hexagonal wire mesh reinforced embankment with silty sand backfill on softclay. *Computers and Geotechnics*, 30:517–534, 2003.

[21] D. Besdo. Inelastic behvaior of plane frictionless block-system described as cosserat media. *Archieve Mechanics*, 37:603–619, 1985.

[22] S.K. Bhatia and A.F. Soliman. Frequency distribution of void ratio of granular materials determined by an image analyzer. *Soils and Foundations*, 30(1):1–16, 1990.

[23] M. Boulon. Basic features of soil structure interface behavior. *Computers and Geotechnics*, 7:115–131, 1989.

[24] M. Boulon and R. Nova. Modeling of soil-structure interface behavior: A comparison between elastoplastic and rate type laws. *Computers and Geotechnics*, 9:21–46, 1990.

[25] R.B.J. Brinkgreve. *Geomaterial models and numerical analysis of softening*. PhD thesis, Delft Institute of Technology, The Netherlands, 1994.

[26] R. Chambon. *Bases théoriques d'une loi de comportement incrémentale consistante pour les sols*. Rapport de Recherche, Groupe C.O.S.M., 1989.

[27] E. Cosserat and F. Cosserat. *Theorie des corps deformable*. A. Hermann et Fils, Paris, 1909.

[28] F. Darve. *Contribution á la détermination de la loi rhéologues incrémentale des sols*. PhD thesis, Université Scientifique et Médicale de Grenoble, France, 1974.

[29] F. Darve. Incrementally non-linear constitutive relationships. In F. Darve, editor, *Geomaterials: Consitutive Equations and Modelling*, 213–237. Elsevier Press, 1991.

[30] R.A. Day and D.M. Potts. Zero thickness interface elements - numerical stability and application. *International Journal for Numerical and Analytical Methods in Geomechanics*, 18:689–708, 1994.

[31] R. de Borst and H.B. Mühlhaus. Gradient dependent plasticity: formulation and algorithmic aspects. *International Journal for Numerical Methods in Engineering*, 35:521–539, 1992.

[32] R. de Borst, L.J. Sluys, H.B. Mühlhaus, and J. Pamin. Fundamental issues in finite element analyses of localization of deformation. *Engineering Computations*, 10:99–121, 1993.

[33] J.T. DeJong and J.D. Frost. Physical evidence of shear banding at granular-continuum interfaces. In A. Smyth, editor, *Proc. 15th ASCE Engineering Mechanics Conference*. http://www.civil.columbia.edu/em2002/, 2002.

[34] C.S. Desai, M.M. Zaman, J.G. Lightner, and H.J. Siriwardane. Thin layer element for interface and joints. *International Journal for Numerical and Analytical Methods in Geomechanics*, 8:19–43, 1984.

[35] J. Desrues, R. Chambon, M. Mokni, and F. Mazerolle. Void ratio evolution inside shear bands in triaxial sand specimens studied by computed tomography. *Géotechnique*, 46:529–546, 1996.

[36] J. Desrues and G. Viggiani. Strain localization in sand: an overview of the experimental results obtained in grenoble using stereophotogrammetry. *International Journal for Numerical and Analytical Methods in Geomechanics*, 28:279–321, 2004.

[37] S. Diebels. A macroscopic description of the quasi-static behavior of granular materials based on the theory of porous media. *Granular Matter*, 2:143–152, 2000.

[38] A. Drescher and I. Vardoulakis. Geometric softening in triaxial test on granular material. *Géotechnique*, 32:291–303, 1982.

[39] W. Ehlers. Foundations of multiphasic and porous materials. In W. Ehlers and J. Bluhm, editors, *Porous media: Theory, Experiments and Numerical Simulations*, 3–86. Springer Verlag Berlin Heidelberg New York, 2002.

[40] A.C. Eringen. Theory of micropolar continua. In *Proceedings of the Ninth Midwestern Mechanics Conference*, 23–40, Univ. of Wisconsin, Madison, 1965.

[41] A.C. Eringen and C.B. Kafadar. Polar field theories. In A.C. Eringen, editor, *Continuum Physics Vol. IV*, 1–73. Academic Press, New York, 1976.

[42] A.C. Eringen and E.S. Suhubi. Nonlinear theory of simple microelastic solids - 1. *International Journal of Engineering Science*, 2:189–203, 1964.

[43] J.D. Frost, J.T. DeJong, and M. Recalde. Shear failure behavior of granular-continuum interfaces. *Engineering Fracture Mechanics*, 69:2029–2048, 2002.

[44] J.D. Frost and D-J. Jang. Evolution of sand microstructure during shear. *Journal of Geotechnical and Geoenvironmental Engineering*, 126:116–130, 2000.

[45] Y.C. Fung. *First course in continuum mechanics, 3rd edition*. Prentice-Hall International, Inc., 1994.

[46] V.K. Garga and J.A. Infante Sedano. Steady state strength of sands in a constant volume ring shear apparatus. *Geotechnical Testing Journal*, 25(4):414–421, 2002.

[47] A. Gens, I. Carol, and E.E. Alonso. An interface element formulation for the analysis of soil-reinforcement interaction. *Computers and Geotechnics*, 7:133–151, 1988.

[48] R.E. Goodman, R.L. Taylor, and T.L. Brekke. A model for the mechanics of jointed rock. *Journal of the Soil Mechanics and Foundations Division*, 94(3):637–659, 1968.

[49] G.R. Grimmett and D.R. Stirzaker. *Probability and random processes*. Claderon Press, Oxford, 1992.

[50] G. Gudehus. Localization in granular bodies - position and objectives. In R. Chambon, J. Desrues, and I. Vardoulakis, editors, *Proc. 3rd International Workshop on Localization and Bifurcation Theory for Soils and Rocks*, 3–11. Balkema, Rotterdam, 1994.

[51] G. Gudehus. A comprehensive constitutive equation for granular materials. *Soils and Foundations*, 36(1):1–12, 1996.

[52] G. Gudehus. Shear localization in simple grain skeleton with polar effect. In T. Adachi, F. Oka, and A. Yashima, editors, *Proc. 4th International Workshop on Localization and Bifurcation Theory for Soils and Rocks*, 3–10. Balkema press, 1997.

[53] G. Gudehus. On the physical background of soil strength. In D. Kolymbas, editor, *Constitutive modeling of granular materials*, 291–301. Springer, 1999.

[54] G. Gudehus. Forced and spontaneous polarisation in shear zones. In H.B. Mühlhaus, A.V. Dyskin, and E. Pasternak, editors, *Proc. 5th International Workshop on Bifurcation and Localization Theory in Geomechanics*, 45–51. Rotterdam: Balkema, 2001.

[55] G. Gudehus. Physical background of hypoplasticity. In W. Wu and H.S. Yu, editors, *Modern Trends in Geomechanics*, 17–37. Springer, 2006.

[56] G. Gudehus and K. Nübel. Evolution of shear bands in sand. *Géotechnique*, 54(3):187–201, 2004.

[57] C. Han and A. Drescher. Shear band in biaxial test on dry coarse sand. *Soils and Foundations*, 33(1):118–132, 1993.

[58] I. Herle and G. Gudehus. Determination of parameters of a hypoplastic constitutive model from properties of grain assemblies. *Mechanics of Cohesive-Frictional Materials*, 4:461–486, 1999.

[59] A. Hettler and I. Vardoulakis. Behavior of dry sand tested in a larger triaxial apparatus. *Géotechnique*, 34(2):183–198, 1984.

[60] W. Huang. *Hypoplastic modelling of shear localization in granular materials*. PhD thesis, Graz University of Technology, Austria, 2000.

[61] W. Huang and E. Bauer. Numerical investigations of shear localization in a micro-polar hypoplastic material. *International Journal for Numerical and Analytical Methods in Geomechanics*, 27:325–352, 2003.

[62] W. Huang, E. Bauer, and S.W. Scott. Behavior of interfacial layer along granular soil-structure interfaces. *Structural Engineering and Mechanics*, 15(3):315–329, 2003.

[63] W. Huang, K. Nübel, and E. Bauer. Polar extension of a hypoplastic model for granular materials with shear localization. *Mechanics of Materials*, 34:563–576, 2002.

[64] W. Huang, D. Sun, and S.W. Scott. Analysis of the failure mode and softening behavior of sands in true triaxial tests. *International Journal of Solids and Structures*, 44:1423–1437, 2007.

[65] T.J.R. Hughes. Generalization of selective integration procedure to anisotropic and nonlinear media. *International Journal for Numerical Methods in Engineering*, 15:1413–1418, 1980.

[66] T.S. Ingold. Laboratory pullout testing of grid reinforcements in sand. *Geotechnical Testing Journal*, 6(3):101–111, 1983.

[67] R.A. Jewell and C.P. Wroth. Direct shear tests on reinforced sand. *Géotechnique*, 37(1):53–68, 1987.

[68] E. Khalili. *Earthquake resistant building structure employing sandbags*. United State Patent 5934027, 1999.

[69] M. Kimura and Y. Fukubayashi. Establishment of design for all-weather rural access road in east africa using labor-based-technology for empowerment of agricultural community. In *Proc. 6th Association of Third World Studies Inc. (ATWS) International Conference Kenya Chapter*, 2005.

[70] D. Kolymbas. *Ein nichtlineares viskoplastisches Stoffgesetz für Böden*. PhD thesis, University of Karlsruhe, 1978.

[71] D. Kolymbas. A generalized hypoelastic constitutive law. In *Proc. XI International Conference on Soil Mechanics and Foundation Engineering (XI ICSMFE)*, page 2626, 1985.

[72] D. Kolymbas. A novel constitutive law for soils. In C.S. Desai, E. Krempl, P.D. Kiousis, and T. Kundu, editors, *Second International Conference on Constitutive Laws For Engineering Materials: Theory and Applications, Tucson, Arizona*. Elsevier, 1987.

[73] D. Kolymbas. Barotropy and pyknotropy of granular materials. In *2nd European Symposium on the Stress and Strain Behaviour of Particulate Solids (CHISA '90)*, 1990.

[74] D. Kolymbas. An outline of hypoplasticity. *Archieve of Applied Mechanics*, 61:143–151, 1991.

[75] D. Kolymbas. *Introduction to Hypoplasticity*. Balkema/Rotterdam/Brookfield, 2000.

[76] D. Kolymbas and I. Herle. Hypoplasticity: A framework to model granular materials. In B. Cambou, editor, *Behaviour of granular materials. CISM courses and lectures No. 385*, 239–268. Springer, 1998.

[77] D. Kolymbas and W. Wu. Introduction to hypoplasticity. In D. Kolymbas, editor, *Modern Approaches to Plasticity*, 213–223. Elsevier, 1993.

[78] H. Konietzky, L. te Kamp, and T. Groeger. Use of DEM to model the interlocking effect of geogrid under static and cyclic loading. In Y. Shimizu, R.D. Hart, and P. Cundall, editors, *Numerical Modeling in Micromechanics via Particle Methods*, 3–11. Taylor & Francis Group, London, 2004.

[79] S. Liu. Introduction to the soilbag as soil reinforcement method. Private communication during one month visit to Graz in November 2006.

[80] T.N. Lohani, K. Matsushima, U. Aqil, Y. Mohri, and F. Tatsuoka. Evaluating the strength and deformation characteristics of a soilbag pile from full-scale laboratory tests. *Geosynthetics International*, 13(6):246–264, 2006.

[81] H. Matsuoka and S. Liu. New earth reinforcement method by soilbags (DONOW). *Soils and Foundations*, 43(6):173–188, 2003.

[82] H. Matsuoka and S. Liu. *A new earth reinforcement method using soilbags*. Taylor & Francis Groups, London, UK, 2006.

[83] T. Mogami. A statistical approach to the mechanics of granular materials. *Soils and Foundations*, 5(2):26–36, 1965.

[84] H.B. Mühlhaus. Application of cosserat theory in numerical solutions of limit load problems. *Ingenieur Archieve*, 59:127–137, 1989.

[85] H.B. Mühlhaus. Continuum models for layered and blocky rock. In J. Hudson, editor, *Comprehensive Rock Engineering: Analysis and Design Methods*, volume 2, 209–230. Pergamon Press, 1993.

[86] H.B. Mühlhaus and I. Vardoulakis. The thickness of shear bands in granular materials. *Géotechnique*, 37:271–283, 1987.

[87] J.C. Nagtegaal, D.M. Parks, and J.R. Rice. On numerically accurate finite element solutions in fully plastic range. *Computer Method in Applied Mechanics and Engineering*, 4:153–177, 1974.

[88] A. Neddleman. A material rate dependence and mesh sensitivity in localization problems. *Computer Method in Applied Mechanics and Engineering*, 67:69–85, 1988.

[89] K. Nübel. *Experimental and numerical investigation of shear localization in granular material*. PhD thesis, University of Karlsruhe, 2002.

[90] K. Nübel and W. Huang. A study of localized deformation pattern in granular media. *Computer Method in Applied Mechanics and Engineering*, 193:2719–2743, 2004.

[91] M. Oda and H. Kazama. Microstructure of shear bands and its relation to the mechanics of dilatancy and failure of dense granular soils. *Géotechnique*, 48:465–481, 1998.

[92] M. Oda, J. Konish, and S. Nemat-Nasser. Experimental micromechanical evaluation of strength of granular materials: effect of particle rolling. *Mechanics of Materials*, 1:269–283, 1982.

[93] M. Oda, T. Takemura, and M. Takahashi. Microstructure in shear band observed by microfocus x-ray computed tomography. *Géotechnique*, 54(8):539–542, 2004.

[94] S. Paikowsky, C.M. Player, and P.J. Connors. A dual interface apparatus for testing unrestricted friction of soil along solid surfaces. *Geotechnical Testing Journal*, 18(2):168–193, 1995.

[95] E.M. Palmiera and G.W.E. Milligan. Scale and other factors affecting the results of pullout tests of grids buried in sand. *Géotechnique*, 39(3):511–524, 1989.

[96] J. Pamin. *Gradient dependent plasticity in numerical simulation of localization phenomena*. PhD thesis, Delft Institute of Technology, The Netherlands, 1994.

[97] J.G. Potyondy. Skin friction between various soils and construction materials. *Géotechnique*, 2(4):339–353, 1961.

[98] W.H. Press, S.A. Teukolsky, W.T. Vetterling, and B.P. Flannery. *Numerical recipes in Fortran 77 - The art of scientific computing*. Cambridge University Press, 2nd edition, 1992.

[99] R.W. Schilder. *Das Kunststoffbewehrte Schotterbett*. PhD thesis, Graz University of Technology, Austria, 1983.

[100] M. Shahinpoor. Statistical mechanical considerations on storing bulk solids. *Bulk Solids Handling*, 1:31–36, 1981.

[101] K.G. Sharma and C.S. Desai. Analysis and implementation of thin layer element for interfaces and joints. *Journal of Engineering Mechanics*, 118(12):2442–2462, 1992.

[102] E.S. Suhubi and A.C. Eringen. Nonlinear theory of simple microelastic solids - 2. *International Journal of Engineering Science*, 2:389–404, 1964.

[103] F. Tatsuoka. An approximate isotropic perfectly plastic solution for compressive strength of geosynthetic-reinforced soil. *Geosynthetic International*, 11(5):390–405, 2004.

[104] F. Tatsuoka, M. Sakamoto, T. Kawamura, and S. Fukushima. Strength and deformation characteristics of sand in plane strain compression at extremely low pressures. *Soils and Foundations*, 26(1):65–84, 1986.

[105] F. Tatsuoka, M. Tateyama, T. Uchimura, and J. Koseki. Geosynthetic-reinforced soil retaining walls as important permanent structures. *Geosynthetic International*, 4(2):81–136, 1997.

[106] J. Tejchman. Numerical study on localized deformation in a cosserat continuum. In *Proc. of 8th International Conference on Computer Methods and Advances in Geomechanics, Morgantown, USA*, 695–701, 1994.

[107] J. Tejchman. *Modeling of shear localization and autogeneous dynamic effect in granular bodies*. Publication series of the Institute for Rock and Soil Mechanics, No. 140, University of Karlsruhe, 1997.

[108] J. Tejchman. Numerical modeling of shear localization with a polar hypoplastic approach. In T. Adachi, F. Oka, and A. Yashima, editors, *Proc. of the 4th International Workshop on Localization and Bifurcation Theory for Soils and Rocks*, 323–332. Balkema, Rotterdam, 1997.

[109] J. Tejchman. Behavior of granular bodies in induced shear zones. *Granular Matter*, 2(2):77–96, 2000.

[110] J. Tejchman. Fe-simulations of a direct wall shear box test. *Soils and Foundations*, 44(4):67–81, 2004.

[111] J. Tejchman and E. Bauer. Numerical simulation of shear band formation with a polar hypoplastic model. *Computers and Geotechnics*, 19(3):221–244, 1996.

[112] J. Tejchman and E. Bauer. Effect of cyclic shearing on shear localization in granular bodies. *Granular Matter*, 5(4):204–212, 2004.

[113] J. Tejchman and E. Bauer. Fe-simulations of a direct and a true simple shear test within a polar hypoplasticity. *Computers and Geotechnics*, 32:1–16, 2005.

[114] J. Tejchman and G. Gudehus. Shearing of a narrow granular layer with polar quantities. *International Journal for Numerical and Analytical Methods in Geomechanics*, 25:1–28, 2001.

[115] J. Tejchman, I. Herle, and J. Wehr. Fe-studies on the influence of initial void ratio, pressure level and mean grain diameter on shear localization. *International Journal for Numerical and Analytical Methods in Geomechanics*, 23:2045–2074, 1999.

[116] J. Tejchman and W. Wu. Numerical study on shear band patterning in a cosserat continuum. *Acta Mechanica*, 99:61–74, 1993.

[117] J. Tejchman and W. Wu. Experimental and numerical study of sand-steel interfaces. *International Journal for Numerical and Analytical Methods in Geomechanics*, 19:513–536, 1995.

[118] M. Uesugi and H. Kishida. Frictional resistance at yield between dry sand and mild steel. *Soils and Foundations*, 26(4):139–149, 1986.

[119] M. Uesugi and H. Kishida. Influential fators of friction between steel and dry sands. *Soils and Foundations*, 26(2):33–46, 1986.

[120] M. Uesugi, H. Kishida, and Y. Tsubakihara. Behavior of sand particles in sand-steel friction. *Soils and Foundations*, 28(1):107–118, 1988.

[121] P. Unterreiner, J. Sulem, I. Vardoulakis, and M. Boulon. Essential feutures of a cosserat continuum in interfacial localization. In R. Chambon, J. Desrues, and I. Vardoulakis, editors, *Proc. 3rd International Workshop on Localization and Bifurcation Theory for Soils and Rocks*, 141–152. Balkema, Rotterdam, 1994.

[122] I. Vardoulakis. 2nd gradient constitutive models. In D. Kolymbas, editor, *Constitutive modeling of granular materials*, 225–248. Springer, 1999.

[123] I. Vardoulakis and E.C. Aifantis. Gradient dependent dilatancy and its implications in shear bending. *Ingineur Archieve*, 59:197–208, 1989.

[124] W. Wu and E. Bauer. A hypoplastic model for barotrophy and pyknotropy of granular soils. In D. Kolymbas, editor, *Modern Approaches to Plasticity*, 225–246. Elsevier, 1993.

[125] W. Wu, E. Bauer, and D. Kolymbas. Hypoplastic constitutive model with critical state for granular materials. *Mechanics of Materials*, 23:45–69, 1996.

[126] W. Wu and D. Kolymbas. Hypoplasticity then and now. In D. Kolymbas, editor, *Constitutive modeling of granular materials*, 57–105. Springer, 1999.

[127] Y. Yoshimi and T. Kishida. A ring torsion apparatus for evaluating friction between soil and metal surfaces. *Geotechnical Testing Journal*, 4(4):148–152, 1981.

Monographic Series TU Graz

Computation in Engineering and Science

Volume 1
Steffen Alvermann
Effective Viscoelastic Behaviour of Cellular Auxetic Materials
2008, *ISBN 978-3-902465-92-4*

Volume 2
Sendy Fransiscus Tantono
The Mechanical Behavior of a Soilbag under Vertical Compression
2008, *ISBN 978-3-902465-97-9*

Volume 3
Thomas Rüberg
Non-conforming FEM/BEM Coupling in Time Domain
2008, *ISBN 978-3-902465-98-6*